Regulation of Breast Cancer Cell Morphological and Invasive Characteristics by the Extracellular Environment

Michelle Ziperstein

Submitted in partial fulfillment of the
Requirements for the degree of
Doctor of Philosophy
in the Graduate School of Arts and Sciences

COLUMBIA UNIVERSITY

2016

ABSTRACT

Regulation of Breast Cancer Cell Morphological and Invasive Characteristics by the Extracellular Environment

Michelle Ziperstein

The aim of this thesis is to evaluate the role of the extracellular environment in regulating breast cancer cell morphological and invasive characteristics. *In vitro* experiments of breast cancer cell lines in three dimensional matrices, which afford control over variables of interest while maintaining physiological relevance, were utilized for this purpose. We evaluated the sensitivity of cell morphology to the dimensionality, biochemistry, and mechanical properties of the extracellular environment as well as the reciprocal effects cells display when remodeling the extracellular environment during invasion.

Chapter 1 introduces background material on breast cancer development, classification systems, and *in vitro* methods of research. Chapter 2 describes protocols for cell care and experiments used in these studies. In chapter 3, we explore the role of fibrillar collagen I environments in breast cancer cell invasion. This was motivated by previous research that has associated high breast tissue density with breast cancer risk and poor prognosis as well as tissue stiffness with cancer cell aggressiveness. Breast cancer cells were found to regain an invasive phenotype in sterically constrained environments when the extracellular matrix included a fibrillar component. In chapter 4, the relationship between cell morphology and invasive behavior in various dimensional contexts was assessed. Anecdotal evidence has shown stellate morphology may be associated with epithelial to mesenchymal transition and invasive capacity in cancer cells. Differences in the dimensionality and biochemistry of the environment resulted in changes to cell

aggregate morphology. Although morphology did not predict invasive capacity as measured by spheroid invasion in collagen I, invasion was found to correlate with cancer-related gene expression profiling, suggesting the ability of cancer cells to utilize more than one mode of invasion. Chapter 5 explores to what degree the presence of invasive cells can give rise to invasive behavior from noninvasive cells. Segregation of cell subtypes during co-culture spheroid formation was found to be altered in the presence of BME. When implanted into collagen gels, invasive cell lines that generate structural changes to the extracellular matrix on their own were able to confer invasive behavior to otherwise noninvasive cell lines in some cases. Chapter 6 summarizes these findings and suggests further studies. Appendix 1 lists useful abbreviations. In Appendices 2 and 3, codes for ImageJ and Matlab-based analyses are recorded.

Through this work, we see how cell morphology and invasive capacity are influenced by the extracellular environment. Cells that can interact with components of the extracellular matrix through matrix-specific integrins show a range of capacities for remodeling the extracellular environment, which in turn plays a role in invasive capacity. We anticipate that enhanced understanding of the role of the extracellular environment in regulating cell morphology and invasive behavior will lead to advances in the study of cell locomotion as well as in cancer research, diagnosis, and treatment.

Table of Contents

List of Figures

List of Tables

Acknowledgements

I would like to express my sincere gratitude to my thesis advisor, Dr. Laura Kaufman. Her knowledge, creativity, and guidance has been pivotal to the success of this work and her affinity for pursuing a range of academic interests has granted me a remarkable learning environment for the past five years. I would like to thank the members of my dissertation committee whose insight and encouragement has been steadfast throughout the course of my graduate research: Dr. Ruben Gonzalez and Dr. Ann McDermott. Additional thanks to Dr. Wei Min and Dr. Maribel Vazquez for their contributions as dissertation committee members during this meaningful period in my graduate career.

This work would not have been possible without the invaluable contributions of Dr. Asja Guzman, a remarkable colleague beside whom I have had the pleasure of working during most of my time at Columbia University. I am also grateful to several members of my group who have made contributions great and small to this research: Dr. Jieling Zhu, Dr. Keewook Paeng, Yen Nguyen, Alex Devanny, Victor Alemany, and Daniel Lee. Furthermore, I'd like to thank the rest of the members of the Kaufman group who have made this time memorable. Although I cannot make an exhaustive list, please know how thankful I am; in particular: Dr. Lindsay Leone, Dat Tien Hoang, and Alyssa Manz. Special thanks also go to Ruby and Hickory Kaufman-Reichman for their attendance and attention during most subgroup meetings.

Lastly, thanks to my friends and family for their unwavering support: my parents, Frances Fingeroot and Dr. Jerrold Ziperstein; my sister and brother-in-law Robyn and Ed Grodin; and my New York-forged family, especially Dr. Joshua Palmer.

1 Introduction

Breast cancer is the second most commonly diagnosed form of cancer with the second highest mortality rate for women in the United States, after skin cancer and lung cancer, respectively.[1,2] Possible explanations for the high rate of breast cancer diagnosis include greater numbers of women regularly getting screened as well as ongoing improvements to the screening process that allow detection at an earlier stage than ever before. Additionally, lifestyle factors like obesity, age, and reproductive and breastfeeding practices can alter risk for developing breast cancer.[3] While improvements in screening have contributed to a steadily increasing number of breast cancer diagnoses, advancements in characterizing and personalizing treatment have aided in decreasing breast cancer mortality rate.[4] Nonetheless, breast cancer mortality rate remains high, affirming the ongoing need for improvements in understanding the threat of breast cancer progression and how to effectively treat it.

The current clinical paradigm for detecting breast cancer involves regularly scheduled mammograms, or x-rays, of breast tissue.[5] If an area looks suspicious or irregular, a tissue biopsy is taken and examined by a pathologist who evaluates the sample for the presence of cancer cells, tumor size, tumor grade, and hormone receptor status, which doctors use to predict therapeutic response and risk of recurrence. More recently, a shift is underway towards the use of gene expression profiling to create more patient-specific treatment plans. For example, genomic breast cancer tests like Oncotype DX, MammaPrint, and PAM50 have been developed that monitor certain sets of genes (21, 70, and 50, respectively) evaluated for their ability to predict cancer

subtype, prognosis, and therapeutic response.[6] As a relatively new technology, emerging data lead to continuing development, validation, and evaluation of these tests.

Accurate early diagnosis requires an understanding of which abnormal cells will become invasive. Thus far, the field of breast cancer detection has been dominated by pathology-based evaluations, with a recent shift towards bioinformatics approaches like genetic profiling. We argue in this thesis that physiologically relevant *in vitro* methods provide important complementary modes to understanding critical factors in invasion and metastasis and may even be useful clinically, in identification of early stage breast cancers with invasive capacity.

1.1 Composition of breast tissue

Healthy breast tissue is essentially composed of cells organized into branching ducts within an extracellular matrix (ECM) of connective tissue, collagen I, basement membrane, and fat.[7] Each mammary gland contains 11-48 lobes, with each lobe containing dozens of lobules.[8] Lobules are clusters of 10-100 sacs called acini, where milk production occurs. The acini and connecting ducts consist of luminal epithelial cells lining the inner surfaces of breast ducts and glands and myoepithelial cells forming a thin layer between luminal cells and basement membrane, which can contract to aid in milk excretion during lactation.[9] It may be noted that the terms "luminal" and "basal" are also used with slightly different meanings for clinical and pathological categorizations of breast cancers, as will be described in Section 1.3. Structurally supporting the duct system are adipose cells, collagen I fibers, and other ECM components.

Throughout a woman's lifetime, breast composition undergoes several phases of change and development, as well as periods of regulation and maintenance. Broadly, the ductal system within the breasts are maintained by epithelial cells, which are cuboidal in shape and organize into single-layered sheets that line acini and ducts, and a surrounding layer of stellate-shaped myoepithelial cells (Figure 1).[10] Growth during embryo development, changes to milk glands during menstrual cycles, extensive lobule formation and lactation during pregnancy, and gland involution during menopause are all regulated modifications to breast structures that necessitate changes in cell shape during cell division and differentiation.[11,12] Mutations to cells that lead to unregulated proliferation and motility, however, characterize a transition to cancer development.

1.2 Features of breast cancer

Cancer begins in healthy cells that accumulate mutations causing dysregulation of tissue maintenance, altered sensitivity to growth factors and antigrowth signals, enhanced cell proliferation, resistance to apoptosis, and sustained angiogenesis[13] followed by epithelial to mesenchymal transition (EMT)[14]. The role of EMT as a facilitator of metastasis has been proposed for cancer cells whose response to signaling cues within the primary tumor enable them to invade local blood or lymphatic vessels, circulate, and invade remote organs, where they can undergo mesenchymal to epithelial transition and form secondary tumors.[15] EMT is associated with inactivation of E-cadherin cell-cell junctions[16] or other cell-cell adhesion molecules[17], changes in cell polarity, shape, and motility, increased production of ECM components, and resistance to apoptosis, contributing to enhanced migratory and invasive behavior.[18] Additional features of

metastatic cells include increased protease activity[19,20] and the ability to shift integrin expression to adapt to new environments[21,22].

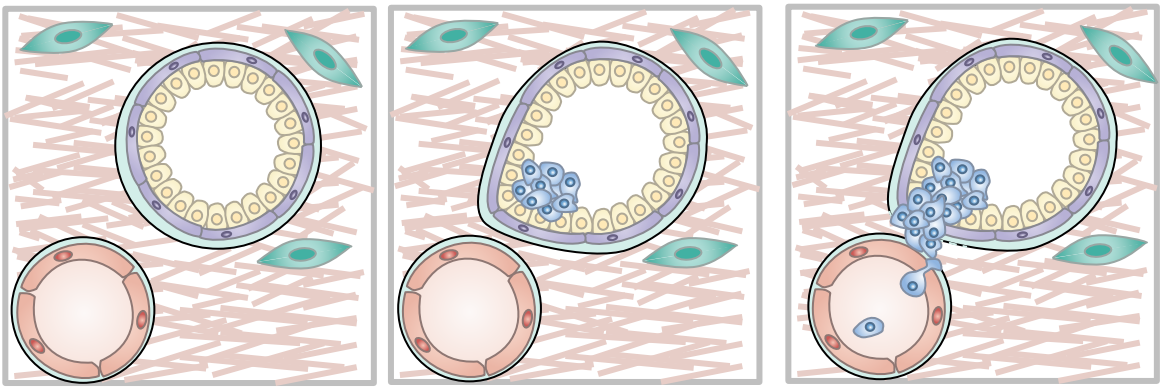

Figure 1 Progression of breast cancer metastasis. Cancer cells are presented in blue, epithelial cells are yellow, myoepithelial cells are purple, basement membrane is light blue, fibroblasts are green, blood vessel is red, and surrounding pink fibers are collagen I-rich ECM. From left to right: healthy breast tissue is shown before cancer cells form, blue cells indicate initial tumor growth in the breast duct, and final image shows invasive tumors cells that have breached the basement membrane and have intravasated into a nearby blood vessel. Image adapted from Reference [10].

The tumor that forms originally is referred to as a primary tumor. Tumors that have not invaded into surrounding tissues are called *in situ* (noninvasive, pre-invasive, pre-cancer) and may be surgically removed, treated with radiation or medication, or monitored for evidence of invasive behavior.[23] If the tumor reaches surrounding tissues, it is classified as an invasive (infiltrating) form of cancer. Cancer cells utilize changes in cell morphology and integrin-mediated ECM sensing during key events in metastasis including breaching basement membrane, intravasating

into blood or lymphatic vessels, and extravasating to other organs. Metastasis is known to occur collectively or individually, with cancer cells having the ability to adapt their mode of invasion to overcome environmental challenges.[24–26] Figure 1 illustrates the progression of healthy breast duct cells to initial stages of invasive breast cancer.

1.3 Classifications of breast cancer

Breast cancer tumors are traditionally classified by histological grade, tumor size, and lymph node stage. The grading system was developed as a reproducible method for doctors to evaluate the appearance of abnormal tumor cells. Evaluations are based on the following features: the percentage of tubule formation- does the tumor tissue have normal breast duct structures; degree of nuclear pleomorphism- do the nuclei of the cells have regular size, shape, and number; and mitotic rate- how many cells are actively dividing.[27] Each category is evaluated with a score of one to three, one being normal-like and three being abnormal, and the total score is translated into grades. Grade 1 is "well differentiated" for scores 3-5, Grade 2 is "moderately differentiated" for scores 6-7, and Grade 3 is "poorly differentiated" for scores 8-9. Lower grade generally describes slower growing tumors and higher grade describes more aggressive tumors. Stages 0-IV refer to how big the primary tumor has grown and how far it has spread in the body, with stage 0 or I referring to small tumors that have not reached lymph nodes, stage II including tumors of an intermediate phase (either bigger and have not reached lymph nodes or smaller and have reached lymph nodes), stage III referring to tumors that have spread to lymph nodes, and stage IV referring to cancers that have spread to other organs.[28] Doctors use histological grade, cancer stage, hormone receptor and HER2 status, and information of patients' general health to predict prognosis and

designate appropriate treatment plans. Better screening has led to more cancer detected at an early stage, complicating guidance for treatment.

In research settings, breast cancers are commonly classified by their subtype: luminal A/B, triple-negative/basal-like, HER2 positive, or normal-like. These subtypes were originally based on the clustering of gene expression profiles from samples from 42 individuals[29] and has since expanded to include claudin-low, molecular apocrine, and interferon-related subtypes.[30] Although tumors within each group show some diversity, there are distinctive traits that are generally shared among tumors of a given subtype. Luminal tumors are ER (estrogen receptor) positive, mostly low grade, and can be PR (progesterone receptor) and HER2 positive or negative.[31] Basal-like tumors show the most diversity across the subtype, but are generally ER, PR, and HER2 negative.[30] HER2 positive subtype indicates upregulated HER2 expression; nonetheless, there are HER2 positive tumors that cluster more closely to luminal and basal-like groups.[32] Claudin-low tumors are generally ER negative, PR negative, and HER2 negative, but are distinguished from basal-like tumors by more enriched EMT features and stem cell associated processes.[33] As new biomarkers are discovered, classification of breast tumors continues to be refined in an attempt to aid researchers in understanding the diversity of breast tumors and developing more effective targeted strategies for treatment.

1.4 Breast cancer cell lines

Cell lines are derived from cells isolated from primary cultures. Most cells can only proliferate a limited number of times before reaching senescence. However, cells may also undergo spontaneous or chemically- or virally-induced transformations to be able to continually proliferate.

Not all cancer cell lines undergo spontaneous immortalization - although more aggressive cancer lines are more likely than less aggressive lines to spontaneously immortalize - and some non-cancer cell lines do. Many of these continuous or immortalized cell lines are commercially available and widely used for researching the physiology, biochemistry, and behavior of normal or cancerous cells. Cell lines are identified by an alphanumeric code and the organism, tissue, and disease from which the line was derived.

Each cell line is genetically homogeneous. This provides several advantages, such as ease of handling, ability to amass large numbers of cells needed for certain experiments, ability to replicate results over time and between laboratories, and avoidance of ethical issues surrounding animal or human experiments.[34] However, they are prone to genotypic and phenotypic drift during ongoing culture, so use is generally limited to cells passaged fewer than 25 times. Whereas primary cells from a cancer patient may be more representative of early stage cancer progression, their slow proliferation, finite lifespan before senescence, difficulty in obtaining large numbers, and overgrowth of stromal fibroblasts in cultured tissues from primary samples[35] remain challenges for research purposes. For these reasons, cell lines have been chosen for the following work, with the hope of expanding to primary breast cancer cells in the near future.

All breast cancer cell lines used in these studies were originally derived from breast primary tumors, pleural effusions, ascites or metastatic sites in individual patients.[36] Similar to patient samples, breast cancer cell lines can also be classified into subtypes and by hormone-receptor status. Hierarchical clustering of gene expression profiles of several established breast cancer cell lines revealed basal-luminal distinctions consistent with cancer subtypes, but with one luminal type and two basal types defined.[37,38] In this work, the following breast cancer cell lines

were used: MDA-MB-231, Hs 578T, MDA-MB-468, MDA-MB-157, ZR-75-1, and MDA-MB-453. The MCF10A cell line was also used; this cell line originated from spontaneously immortalized cells derived from benign breast tissue of a woman with fibrocystic disease.[39]

1.5 Interactions between cells and environment

Much cancer research is performed through patient studies or animal models or by doing experiments on cells on two dimensional (2D) substrates. These methods are complementary, with the former providing physiological relevance but limited control and the latter allowing for greater control over variables of interest. In recent years, there has been growing interest in exploring the reciprocal relationship between cells and their environment. For *in vitro* experiments, this has led to a shift towards studying cells in three dimensional (3D) matrices in an attempt to more closely approximate the *in vivo* environment.[40–42] Breast cancer researchers were some of the first to acknowledge the importance of dimensionality, ECM composition, and stiffness in regulating cell behavior.[43–49] Whereas normal breast cells cultured on 2D plastic remain relatively undifferentiated, cells within ECM gels form normal mammary acini and duct structures. [44,45,50,51] Mixing compliant basement membrane extract (BME) made of laminin, collagen IV, and other components with fibrillar collagen I in defined proportions creates gels with stiffnesses near that of normal and malignant breast tissue.[49] *In vitro* studies of breast tissues have been expanded to other *in vitro* cell studies including cancer cell motility[52] and cancer explants[53].

Cancer cells and ECM are known to exchange signals in both directions. Cancer cells can degrade or remodel existing matrix components as well as synthesize new components, while altered matrix architecture can provide signals to cells that control malignant phenotype.[54] While

it is known that high breast density, which is associated with high collagen content, is a substantial risk factor for developing breast cancer,[55] much remains to be understood regarding the significant role collagen content and organization plays in breast cancer invasion. There are at least 28 types of collagen, some of which form fibrils and others which form non-fibrillar basement membrane components. Collagen type I is a fibril-forming species that provides structural support in healthy breast tissue. It has also been shown to be over-deposited near the invasion front of tumors.[56] Collagen type IV is non-fibrillar and is essential for basement membrane integrity, which lines epithelial cell layers.[57] For metastasis to occur, tumor cells must overcome the collagen IV- and I-rich physical barriers to invasion.

Cells sense and adhere to ECM though integrins.[58,59] Integrins are transmembrane proteins composed of two subunits, α and β, that form ligand-specific binding sites for ECM components such as collagen and laminin. The presence and density of integrins varies by cell type and cell line. Collagen I is recognized by integrins α2β1, α1β1, α10β1, and α11β1.[60–62] The integrin α2β1 in particular has been implicated as the only integrin that can generate traction on collagen I fibers.[63] Laminin, a component of basement membrane, can be recognized by α3β1, α6β1, α6β4, and α7β1.[64,65] Other ECM components that contain the Arg-Gly-Asp sequence (RGD) like fibronectin are recognized by another independent set of integrins,[66] as summarized in Figure 2. By virtue of their role in binding to components of ECM, integrin adhesions play roles in regulating cell growth, polarization, migration, and differentiation, tissue organization, and matrix remodeling.[67]

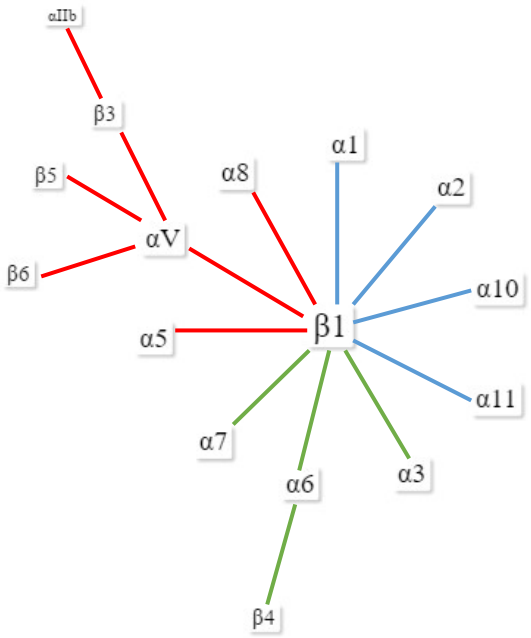

Figure 2 Integrin subfamilies. Integrins consist of 1 of 18 α subunits and 1 of 8 β subunits, with some subunits able to combine with several different subunits. The image shows several of the possible combinations organized into three subfamilies: collagen-binding integrins (blue), laminin-binding integrins (green), and RGD-binding integrins (red). Image adapted from reference [59].

1.6 *In vitro* experimental measures of motility and invasion

There are considerable advantages to conducting *in vitro* experiments over *in vivo* experiments to probe aspects of breast cancer, including control over variables of interest, better visualization of the experiment in progress, cost, speed, and ethical considerations. Several *in vitro* invasion assays that have been used in these studies are highlighted below and depicted in Figure 3, each selected for their ability to reveal a different aspect of breast cancer cell morphology and

interaction with extracellular environments while providing control over potentially confounding variables.

One of the simplest techniques to investigate cells *in vitro* is a morphology assay. In this case, the shape of cells is monitored and compared between different 2D or 3D seeding environments. Live cells can be viewed by transmittance microscopy, transfected with GFP, or labeled with a live cell tag or alternatively fixed and stained with fluorescent dyes to see actin arrangement or integrin clustering. Some examples of seeding environments include on tissue culture plastic dishes or on top of or dispersed within a gel of collagen, BME, or other matrix of interest.

The cell exclusion zone assay, also referred to as a gap assay, is a variation of the commonly used wound healing or scratch assay. In this experiment, two confluent areas of cells on a 2D surface are monitored as they migrate towards one another across a precise distance. This provides the advantages of simple and cheap setup and quantifiable analysis of live cell migration.

Transwell assays are pseudo-3D assays in which cells on top of a porous membrane migrate through pores toward a nutrient gradient or other chemoattractant.[68,69] This is considered by some to be a rather simplified approach to modeling migration or invasion[70] and has several limitations. Primarily, the behavior of cells on a stiff porous membrane is not reflective of what cells experience *in vivo* in dimensionality, cell-cell contacts, or pliability of the ECM environment. It is also difficult to compare results across cell lines, as the sizes of cells vary and therefore the challenge of squeezing through pores of a defined size are not consistent across samples, leading to differences in the optimal timeframe required for cells to pass through the membrane.

Nonetheless, the assay can still be used for certain research applications keeping these limitations in mind.

Although not used for the research presented here, time-lapse experiments monitoring cells dispersed in physiologically relevant gels have been utilized to study various aspects of cell migratory behavior including speed, directionality, and persistence.[71,72]

Spheroids are a useful *in vitro* model of cancer invasion in that they recapitulate cell-cell and cell-environment contacts of *in vivo* tumors better than many other common methods of studying cancer cell invasion and are compatible with a range of commercially available gel-forming ECM components such as collagen and BME. Not all cells form compact spheroids, however. The MDA-MB-231 breast cancer cell line, for example, can form spheroids in hanging drops without any supplementary components, whereas the MDA-MB-468 breast cancer cell line cannot. To keep spheroid formation methodology consistent across cell lines in our studies, spheroids were always made using supplementary BME and centrifugation as described in section 2.7.1. Spheroid behavior can be monitored during formation or after implantation on top of or within collagen gels or other matrices of interest. Spheroid invasion assays are time and labor-intensive but are considered by many research labs to be highly physiologically relevant models of cell invasion.[73]

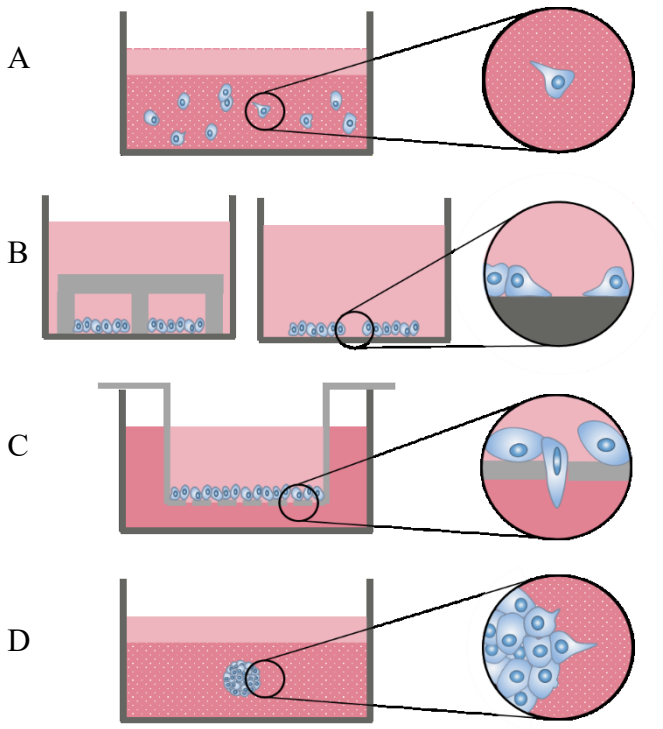

Figure 3 Schematic of *in vitro* morphology, migration, and invasion assays. Cells and nuclei are shown in blue, growth medium in pink, collagen in dark pink with pattern, and experimental inserts in gray. Images on left are of initial experimental setup and black circles on right show enlarged image of a later time point. (A) Morphology assay showing cells in a 3D gel overlaid with growth medium can also be conducted on 2D. After 24 hours, samples are fixed, actin is stained with phalloidin, and cells are imaged. (B) Gap closure 2D migration assay: cells are grown to confluence within the chambers of a temporary insert. Insert is removed at the beginning of the experiment, leaving a gap between the confluent areas, and cells migrate into the gap. (C) Transwell pseudo-3D assay: cells squeeze through the pores at the bottom of a Transwell insert towards a stronger nutrient gradient. (D) Multicellular tumor spheroids are implanted in a collagen gel overlaid with growth medium. Over time, cells may rearrange surrounding collagen fibers and invade into the collagen gel.

1.7 Motivation

The work presented here aims to model several poorly or incompletely understood breast cancer behaviors. Understanding what cell morphology can reveal about invasive capacity as well as the role that the extracellular environment plays in regulating these characteristics will be crucial in moving breast cancer research forward.

In chapter 3, we explore the role of fibrillar matrix architecture and other physical challenges in the establishment of invasive phenotype. Several biochemical and physical properties of the extracellular environment are associated with breast cancer progression and metastasis. High tissue density and elevated amounts of fibrillar collagen have been associated with higher risk of breast cancer and poor prognosis.[74,75] High collagen density contributes to higher stiffness around breast tumors, which correlates with breast cancer aggressiveness.[76] Reorganization of the collagen network has also been correlated to poor prognosis, as cells can migrate along radially aligned collagen fibers.[77,78] This study demonstrates that breast cancer cells can establish an invasive phenotype and invade sterically constrained environments when a fibrillar component is present in the ECM.

In chapter 4, the potential for cell morphology-based assays to predict invasive behavior in various dimensional contexts will be assessed. Anecdotal evidence has suggested that a stellate morphology in cancer cells is associated with more invasive behavior. This is consistent with the fact that cancer cells undergo EMT often accompanied by a mesenchymal-like elongated morphology.[79,80] A recent study showed that between paired osteosarcoma cell lines of a less invasive parent line and a more invasive line derived by *in vivo* selection, the more invasive lines were distinguishably more mesenchymal-like in shape in 75% of the samples.[81] Stellate

morphology has also been shown to cluster with nonhierarchical gene profiling expressions, indicating changes in shape may reflect genetic changes that lead to invasiveness of cancer cells.[82] Ultimately, this work shows that cell aggregate morphology is not fully independent of dimensionality and biochemistry of the environment and is not a robust predictor of invasive capacity. However, invasion from a spheroid into collagen I was found to correlate with hierarchical clustering of gene profiling expressions concerning genes known to regulate cancer progression, regardless of morphological class or mode of invasion. This suggests cancer cells can adapt their mode of invasion to overcome physical challenges in the ECM.

Finally in chapter 5, we will examine to what extent and by what means the presence of invasive breast cancer cells contribute to the invasive potential of less aggressive cells, with a view towards whether structural changes to the ECM by one cell line can confer invasive behavior to a cell line not otherwise invasive. Pairs of cell lines varying in cell morphology, invasive capacity, and integrin expressions were prepared as co-culture spheroids. Segregation of cell subtypes during spheroid formation was monitored in the presence and absence of BME. Furthermore, invasion from co-culture spheroids showed under what conditions noninvasive cells broke away from the spheroid core behind invasive leader cells.

This work explores how cancer cells adapt to and overcome challenges in the ECM. Cells can identify the composition of ECM through matrix-specific integrins and show a range of capacities for remodeling the extracellular environment. This, in turn, plays a role in regulating cell morphology and invasive behavior. It is our intention that a better understanding of the role of ECM in cancer progression will lead to enhanced understanding of cancer invasive capacity and

the causal relationship with ECM reorganization as well as identification of new drug targets for breast cancer and other invasive cancers.

2 Materials and methods

2.1 Cell care

2.1.1 Cell lines

The MCF-10A cell line was a gift from the Carol Prives lab (Biological Sciences, Columbia University). All other cell lines (MDA-MB-231, MDA-MB-468, MDA-MB-157, MDA-MB-453, Hs 578T, and ZR-75-1) were obtained from American Type Culture Collection. All cell lines are human breast cancer cell lines, except for the MCF-10A cell line, which is an immortalized breast epithelial cell line.

2.1.2 Subculture

MDA-MB-231, Hs 578T, and MDA-MB-468 cell lines were cultured in growth medium consisting of 1x high glucose DMEM, 10% (v/v) FBS, 1% (v/v) penicillin/streptomycin solution, and 1% (v/v) 100x nonessential amino acid solution. MDA-MB-157 and ZR-75-1 cell lines were cultured in growth medium consisting of RPMI-1640, 10% FBS, 1% penicillin/streptomycin solution, and 1% nonessential amino acid solution. The MCF-10A cell line was cultured in DMEM-F12 medium supplemented with 20 ng/mL human epidermal growth factor (EGF), 100 ng/mL cholera toxin, 10 µg/mL insulin, 500 ng/mL hydrocortisone, 5% horse serum, and 1% penicillin/streptomycin solution. All base media bottles were stored at 4˚C when not in use. When FBS and penicillin/streptomycin solution were delivered frozen, they were stored at 4˚C and allowed the thaw before preparing aliquots in 50 mL and 15 mL falcon tubes, respectively, and storing them at -20˚C. When new supplemented media bottles were to be prepared, tubes were

thawed in a 37˚C water bath and added to the appropriate base media bottles of DMEM, DMEM-F12, or RPMI-1640. Nonessential amino acid solution was stored at 4˚C.

The following supplements were only required for MCF-10A medium. Human EGF was received in powder form, dissolved in sterile water to a concentration of 100 µg/mL, aliquoted into 150 µL volumes, and stored at -20˚C. When needed, a single aliquot was thawed in a 37˚C water bath and the remainder was discarded. Cholera toxin was received in powder form, dissolved in sterile water to a concentration of 1 mg/mL, and stored at 4˚C. Insulin was received as a 10 mg/mL solution and was stored at 4˚C. Hydrocortisone was received in powder form, dissolved in 95% ethanol to a concentration of 10 mg/mL, and stored at -20˚C. Horse serum was delivered frozen, allowed to thaw at 4˚C, aliquoted in 50 mL falcon tubes, and stored at -20˚C. When needed, aliquots were thawed in a 37˚C water bath.

Cells were generally maintained in 10 cm tissue culture treated plastic petri dishes in 10 mL of growth medium or for certain purposes in tissue culture treated plastic 6-well plates in 5 mL of growth medium. Cells were kept in an incubator at 37˚C with 5% carbon dioxide.

Cells were subcultured when 70-80% confluent, or about every 3 days. Phosphate-buffered saline (PBS) and either trypsin or accutase were warmed to 37˚C in a water bath before splitting. First, growth medium was removed via a Pasteur pipette using an aspirator-pump system and replaced with PBS. PBS was removed and replaced with trypsin or accutase. The 10 cm dishes required 5 mL PBS and 2 mL trypsin or accutase and each well of the 6-well plates required 2 mL PBS and 500 µL trypsin or accutase. The dish was then put back in the incubator for 5-20 minutes to allow the cells to detach from the plate. Growth medium was then added to the dish and the cell suspension was transferred to a falcon tube. From that cell suspension, dilutions could be made for

experiments or for subculture. Most cells lines were generally subcultured 1:3, except for the MCF-10A cell line which needed to be subcultured 1:30. Cells were maintained for up to 25 passages.

2.1.3 Thawing and freezing cells

Up to 30 vials of early passage cells of each cell line were kept in aliquots for long-term storage in a -80˚C freezer.

To thaw cells, a vial was placed in a floating tray in a 37˚C water bath, taking care not to immerse the cap under water. As soon as the cell solution thawed, the suspension was transferred to a 15 mL falcon tube. The vial was rinsed twice with 1 mL warm growth medium, which was added to the falcon tube. Growth medium was added to the tube for a total of 10 mL. The suspension was then centrifuged for three minutes at 1800 rpm. The supernatant was discarded. The cell pellet was resuspended in 10 mL growth medium and plated in a 10 cm dish, which was placed in the incubator for general culturing.

To freeze cells, warm growth medium was supplemented with 5% DMSO (v/v). The cells were treated as above in section 2.1.2 up to the step of transferring the cell suspension to a falcon tube. The cell suspension was then centrifuged for three minutes at 1800 rpm and resuspended in the freezing medium supplemented with DMSO in 2 mL per 10 cm dish. The suspension was then transferred in 1 mL per 1.5 mL cryogenic tube labeled with the cell line, passage number, date, and initials of the person taking care of the cells, which were then placed in the -80˚C freezer for long term storage.

2.1.4 Counting

For almost all experimental purposes, it is necessary to know and control the number of cells per condition. To accomplish this, a hemocytometer was used to count the concentration of cells in a cell suspension. Cells were counted in the 4 corner squares of the hemocytometer and calculated according to the equation: $cell\ suspension = \frac{count\ of\ cells}{4} \times 10^4$. Preferably at least 100 cells were counted. To obtain a lower cell suspension, cells were diluted into a larger volume and used immediately. To obtain a more concentrated cell suspension, cells were centrifuged, resuspended in a smaller volume, recounted, and then diluted to the desired concentration.

2.1.5 Transfection

Transfection was done according to lipofectamine 3000 protocol.[83] Cells were plated at 10^5 cells in 500 µL in 24-well plates the day before transfection to achieve 70% confluence. On the day of transfection, 1 mL of optiMEM was brought to room temperature. Then 0.5 µg of lifeact-tagGFP2 actin plasmid and 1 µL of P3000 per 25 µL of optiMEM were mixed in an Eppendorf tube and separately 0.75 µL of lipofectamine 3000 per 25 µL of optiMEM were mixed in an Eppendorf tube, preparing 25 µL of each mixture per well to be transfected. The solutions were mixed together and left at room temperature for five minutes before being added to a well. Up to 20% transfection was achieved by one to three days. To image, a 488 nm laser was used with a DM570 dichroic mirror so that the 506 nm fluorescence could be seen in channel 1 of the microscope.

For stable transfection, the cells would need to be further treated with G418 antibiotic to eliminate any non-transfected cells. According to previous studies, G418 must be used at 800

μg/mL for eight weeks to achieve stable transfection of the MDA-MB-231 cell line[84], although this was not achieved in our group.

2.1.6 Live cell tags

CellTracker Red CMTPX dye and Vybrant DiD Cell-labeling solution were used for live cell imaging. DiD was received as a 1 mM solution. CMTPX was received as a powder and was dissolved in DMSO to a concentration of 1 mM. Sub-confluent attached cells were treated with 5 μM DiD or 15 μM CMTPX for 1 hour prior to detachment and spheroid preparation.

2.1.7 Immunocytochemistry

To fix cells either on plastic or in collagen gels and fluorescently label desired components of the cells, the following protocol was used. Warm 4% formalin solution was added to the samples and allowed to sit at room temperature for 20 minutes. Samples were washed three times with PBS for 10 minutes. Then 0.5% triton-X detergent was added to the samples for 10 minutes to permeabilize the cells. Samples were again washed three times with PBS for 10 minutes. Alexa Fluor 568 phalloidin (F-actin stain) that was previously dissolved in 1.5 mL PBS and stored at -20˚C was added at 1:50 in 50 μL PBS and samples were left at 4˚C overnight. When samples were ready to be imaged, samples were first washed with PBS. For cadherin staining, cells were fixed in formalin solution for 10 minutes at room temperature, washed with PBS, blocked for nonspecific staining with bovine serum albumin for 30 minutes, and washed with PBS again before primary antibody for E- or N-cadherin was added to the cells for 1 hour at room temperature. Cells

were then washed with PBS and FITC-conjugated secondary antibody was added. The cells were left overnight at 4°C and washed with PBS before imaging.

2.1.8 Gel preparation

Gels were prepared from commercially available stocks of bovine pepsin-treated collagen (PT), rat tail acid-solubilized collagen (AS), or Matrigel BME from Engelbreth-Holm-Swarm mouse sarcoma cells (BME). Concentrations varied between batches, but generally were 5.9-6.1 mg/mL PT, 8.0-11.0 mg/mL AS, and 9.0-11.0 mg/mL BME. Collagen stocks were stored at 4˚C. BME was delivered frozen, allowed to thaw at 4˚C, aliquoted into 1.5 mL tubes, and stored at -20˚C. Tubes were thawed overnight at 4˚C before use. Solutions of water, 10x DMEM, 1 M HEPES buffered at pH 7.3, 7.5% sodium bicarbonate, and 1 N sodium hydroxide (NaOH) were filter sterilized and stored at 4˚C. When making a gel, all components were kept on ice including the tube in which the sample was being prepared. Collagen gels or mixed collagen and BME gels were prepared with 10% (v/v) 10x DMEM, 2.5% (v/v) HEPES, 2.5% (v/v) sodium bicarbonate, and approximately 1% NaOH. The amount of collagen or BME was calculated according to the stock concentration, but generally collagen was used at 1-4 mg/mL and BME was used at 1-3 mg/mL. The remainder of the volume consisted of water or growth medium. For collagen gels, the water, DMEM, HEPES, and sodium bicarbonate were mixed up to an hour ahead of time and left on ice. When the complete collagen solution was needed, the collagen was added by reverse pipetting, then enough NaOH was added to bring the solution to pH 7.4, and the mixture was transferred to the experimental dishes. This step needed to be done quickly and with pre-chilled pipette tips to keep the solution from starting to gel too soon. Reverse pipetting is a technique used

to accurately measure viscous solutions by going to the second stop on the pipette before picking up the volume and releasing very slowly and then when delivering the desired volume doing so slowly and only to the first stop. Collagen-BME mixtures were prepared according to the previous steps and adding BME by reverse pipetting with chilled tips as the last step. BME gels alone were made by adding the desired volume of BME to growth medium only.

2.2 Experimental dishes

Fluorodishes were used to conduct most experiments because the glass coverslip bottom of the dishes were thin enough to image through for most imaging purposes. For spheroid and cells in gels experiments, the volume used for each sample was reduced by gluing cloning cylinders to the dishes. Cylinders were first disinfected by soaking in 70% ethanol. A foam swab was used to apply ultraviolet-curing Norland optical adhesive to one side of the cloning cylinders. Three cylinders were arranged on each fluorodish. The dishes were set under an ultraviolet light for 20 minutes. A thin piece of nylon mesh that had also been disinfected by soaking in 70% ethanol was used to line the inner wall of each cylinder to help anchor gel samples.

2.3 Morphology experiments

Cell morphology experiments were conducted in disperse and aggregate conditions on glass, in collagen, in mixed collagen with BME, and in BME. For disperse and aggregate cells on glass, cell suspensions were added to cylinders on fluorodishes and incubated for 24 hours. For disperse and aggregate cells in collagen or in mixed collagen with BME, cell suspensions were prepared and left on ice while collagen solutions were prepared. Gels of 1 mg/mL collagen with

or without 1 or 3 mg/mL BME were prepared as described above omitting water and instead adding cells in suspension as the final step before plating 70 µL of the solution in cylinders on fluorodishes in triplicate. The samples were left in the incubator for two hours and then overlaid with 50 µL growth medium. The samples were returned to the incubator for the remainder of 24 hours from plating. For disperse cells in BME, BME was added to cell suspensions to reach a final concentration of 3 mg/mL BME. For aggregates in BME, cells were pelleted by centrifugation at 1800 rpm for three minutes, 3 mg/mL BME solution was prepared and transferred to cylinders on fluorodishes, and 1 µL volumes of the cell pellet were streaked in the solutions. The samples were left in the incubator for two hours, overlaid with 50 µL growth medium, and returned to the incubator for the remainder of 24 hours from plating. Samples were then fixed and stained with phalloidin as described in Section 2.1.7 and imaged as described in Section 2.10.1.

2.4 Contraction experiment

A solution of 1 mg/mL PT collagen containing $5x10^5$ cells/mL was prepared as described for disperse cells in collagen above and 500 µL was plated on the 23 mm coverslip bottom of a fluorodish. Samples were incubated for one hour, overlaid with 2 mL growth medium, and manually released from the coverslip bottom by running a 20-200 µL pipette tip around the edge of the dish. Samples were incubated for four more hours to allow time for contraction. Images of the contracted gels were taken and analyzed according to Section 2.10.4. Data from two independent experiments performed in biological triplicate were averaged.

2.5 Transwell migration assay

To prepare cells for the Transwell migration assay, cells were washed with warm PBS and detached with accutase. Cells were then suspended at 3.75 x 10^5 cells/mL in DMEM containing 2% (v/v) FBS and 1% (v/v) penicillin/streptomycin solution with or without 10-20 µM blebbistatin or an equivalent concentration of DMSO. A 200 µL volume of this cell suspension was added to the upper well of a Transwell insert with either 3 or 8 µm size pores, which was placed in 500 µL of DMEM containing 10% (v/v) FBS and 1% (v/v) penicillin/streptomycin solution with or without 10 µM blebbistatin or an equivalent concentration of DMSO in a 24-well plate. The plate was then incubated for 24 hours to allow for cells to migrate from the top of the Transwell insert to the bottom. The samples were fixed with acetone at -20˚C, stained with 0.01% propidium iodide for one hour at 37˚C, and washed with PBS. The membrane of the Transwell insert was cut out with a razor and mounted on a coverslip with vectashield mounting medium for imaging. The cell count from 20 images in duplicate experiments were averaged.

2.6 Cell exclusion zone assay

Ibidi culture inserts were placed at the center of a fluorodish. A cell suspension was prepared and added to both wells of the inserts at 1x10^5 cells in 80 µL. Hs 578T cells were instead prepared at 1x10^4 cells in 80 µL as they were larger and flatter than the other cell lines. After overnight incubation, the growth media in the wells were removed and replaced with DMEM containing 2% (v/v) FBS and 1% (v/v) penicillin/streptomycin solution. After another 24 hours, the inserts were removed, marking the beginning of migration time. The dishes were washed with growth medium until the gaps between the two confluent areas were clear of any cells. The dishes

were left in the incubator with 1 mL of growth media for the remainder of the experiment and removed only for imaging. Two independent experiments were performed in biological triplicate for each cell line.

2.7 Spheroid experiments

2.7.1 Formation

Multicellular tumor spheroids were formed by either hanging drop method or a BME-supplemented centrifugation method. For hanging drop spheroids, 30 µL of $4x10^5$ cells/mL cell suspension was added to each channel of a Perfecta 3D Biomatrix system. Reservoirs at the edge of the plate were filled with growth medium. The spheroids were incubated for six days before harvesting and using for experiments. This method was successful for the MDA-MB-231 cell line but not for the MDA-MB-468 cell line, so the alternative method of BME-supplemented formation of spheroids was used for experiments that would compare results across cell lines.

Low attachment 96-well round bottom plates were used for BME-supplemented spheroid formation. Lipidure-coated plates were used until they were discontinued in 2015, at which point they were replaced with Nunclon sphera microplates. The 96-well plates were chilled for at least one hour and BME was thawed at 4˚C prior to use. The 96-well plates and BME were kept on ice as the cells were detached and counted. A cell suspension was prepared in cold growth medium at $1x10^4$ cells/mL and 0.2575 mg/mL BME. The suspension was transferred to a chilled plastic reservoir and a multichannel pipette was used with chilled tips to add 200 µL to each well. The plates were kept on ice until they were centrifuged for ten minutes at 1000 G and 4˚C. The spheroids were then incubated for one day. Before implanting spheroids, the spheroids were treated

with cell recovery solution. To do this, a 96-well plate was kept on ice and filled with 200 µL cell recovery solution in each well. Spheroids were transferred in 30 µL drops to the top of an inverted plate using cut tips to prevent spheroids from sticking inside the tips. Using cut tips, the spheroids were individually transferred in 5 µL to the cell recovery solution wells and left on ice. After one hour, spheroids were transferred in 30 µL drops to the top of another inverted plate using cut tips, and then individually transferred in 5 µL to experimental gel conditions.

2.7.2 Invasion

Collagen or mixed gel solutions were prepared according to Section 2.1.8. Solutions were transferred to cylinders at 200 µL per cylinder. Spheroids were added to the center of the solution in 5 µL. The dishes were incubated for the remainder of the experiment. After one hour, 50 µL of warm growth medium was added to the top of the gel and 1 mL of growth medium was added to the dish surrounding the cylinders.

2.7.3 Co-culture

Co-culture spheroids were prepared with and without BME from two cell lines treated with DiD and CMTPX live cell dyes. For BME-free spheroid formation, a cell suspension was prepared in cold growth medium at $5x10^3$ cells/mL of each of the two cell lines. Each well of a 96-well low-attachment plate was filled with 200 µL of the solution. The plate was kept at 37˚C except for imaging every two hours for the duration of the experiment. BME-supplemented spheroids were formed similar to the description in Section 2.7.1 from a suspension of cold growth medium at $5x10^3$ cells/mL of each of the two cell lines and 0.2575 mg/mL BME. The spheroids were kept at

37˚C except for imaging every two hours for the duration of formation experiments or incubated for one day before treatment with cell recovery solution and implantation.

2.8 FACS

Cells were detached from the cell culture plate with accutase, resuspended in phenol red-free DMEM with HEPES and 10% FBS, divided into tubes for staining, and kept on ice for the remainder of the procedure. Cells were washed with PBS containing 1% FBS in between steps, left on ice for one hour in primary antibody and then for 40 minutes in secondary antibody. Finally, cells were resuspended in PBS and measurements were taken on a flow cytometer (Becton Dickinson FACSCalibur with BD CellQuest Pro software). The following primary antibodies were employed: α1 and α2 (Millipore), β1 (Beckman Coulter, Brea, CA), α10 (Santa Cruz Biotechnology, Dallas, TX), α11 (Thermo Fisher Scientific) integrin subunits and α2β1 integrin (Abcam, Cambridge, MA), E-cadherin (Thermo Fisher), and N-cadherin (Thermo Fisher). FITC-conjugated secondary antibodies were obtained from Thermo Fisher Scientific and Abcam.

2.9 Rheology

Rheological experiments were conducted on an Anton Paar MCR 302 with a modified glass bottom and built-in Peltier temperature control. A 1˚ polycarbonate cone geometry with evaporation blocker was used. In all cases, 750 mL of neutralized collagen, BME, or collagen/BME solution was applied to the measuring stage at 37˚C or 22˚C. The sample was allowed to gel for 10-30 minutes depending on the gel type. Measurements were then performed in oscillatory mode at $\omega = 1$ Hz and $\gamma = 0.8\%$, within the linear viscoelastic regime. Storage

modulus G' (Pa) and loss modulus G'' (Pa) were measured every 30 seconds for 10 minutes, and all tests were repeated 2-3 times.

2.10 Microscopy and image analysis

An inverted confocal laser scanning microscope (Olympus Fluoview 300) with a photomultiplier tube detector and 10x air (NA = 0.4) or 60x oil (NA = 1.42) objective was used for all microscopic data collection. Details are outlined below, along with alternate forms of data collection and image analysis when microscopy images were not necessary.

2.10.1 Cell morphology

Morphology was assessed by visualizing actin cytoskeleton labeled with Alexa Fluor 568 phalloidin (ex578/em600). A 543 nm HeNe laser was used to excite and a longpass DM570 dichroic mirror was used to separate excitation from emission. Images were taken with the 60x objective. For cells plated on top of matrices (pseudo-3D), the samples were flipped upside down on a coverslip to accommodate the limited working distance of the objective. Imaging E- and N-cadherin was done with a 488 nm excitation laser, longpass DM570 dichroic mirror, 510 nm bandpass filter, and 60x objective. Stacks of images were taken up to 2.5 μm apart for 10-20 μm to ensure the entire cell and its protrusions were imaged. Maximum intensity projections were created from stacks to easily visualize each sample. See the appendix for scripts that can be used in ImageJ to efficiently z-project a folder of multitiff files.

2.10.2 Collagen

Collagen was imaged by confocal reflectance microscopy (CRM) using a 60x objective and 488 nm laser.

2.10.3 Cell exclusion zone

Transmittances images were taken immediately after washing and at 6, 24, and 48 hours on the Olympus Fluoview300 using 488 nm excitation and the 10x objective. Data were averaged from two independent experiments performed in biological triplicate.

2.10.4 Contraction

Images were taken upon release and four hours after release using an 8 megapixel digital camera. Contraction is expressed as a percentage decrease of gel area. Data were averaged from two independent experiments performed in biological triplicate.

2.10.5 Transwell

An epi-fluorescence microscope was used to image Transwell inserts. Quantification was done on 20 images from each sample.

2.10.6 Spheroid

For unlabeled spheroids, transmittance images were taken 2 and 24 hours after implantation. For co-culture spheroids labeled with DiD (ex644/em665) or CMTPX (ex577/em602), formation images were taken with a 10x objective every 2 hours for 10 hours and

invasion images were taken every day for 5 days. DiD was observed using a 10x objective, 633 nm HeNe excitation laser, DM570 mirror, and BA660IF filter. CMTPX was observed using a 10x objective, 543 nm HeNe excitation laser, DM570 mirror, and BA575-630 filter. For each set of co-culture spheroids, single slice images in DiD and CMTPX settings were taken of six samples and one sample was additionally imaged as a z-stack every 5 μm. Images of each spheroid from DiD and CMTPX channels were combined with DiD artificially colored red and CMTPX artificially colored green. See the appendix for scripts that can be used in ImageJ to efficiently combine separate images in DiD and CMTPX settings within a single folder into composite images of overlaid red (DiD) and green (CMTPX) colored images.

3 The effect of fibrillar matrix architecture on tumor cell invasion of physically challenging environments

3.1 Introduction

Extracellular matrix (ECM) is a complex mixture of structural macromolecules and cytokines that regulates key cellular processes including polarization, differentiation, and proliferation through biochemical and biophysical cues. Altered ECM properties have been associated with numerous pathological conditions including atherosclerosis[85], fibrotic diseases[86–88], and cancer[49,89]. In all cases, changes to the ECM are not simply symptoms of disease but are contributors to the pathogenic process.

In cancer, alterations in ECM composition and organization have been implicated in the progression of malignant tumors from circumscribed masses to locally invading entities to eventual metastatic disease. While cancer progression is regulated by a complex interplay of genetic and epigenetic changes, evolving interactions between tumor cells and the surrounding ECM play a critical role in the metastatic cascade.[90,91]

The importance of the local environment and changes to that environment have attracted particular attention among breast cancer researchers, as high breast tissue density has been associated with both higher risk of breast cancer and poor prognosis in patients.[74,75] High breast tissue density is due to higher than average amounts of the fibrillar structural proteins collagen I, and elevated amounts of this protein as well as fibrillar collagen III in and around tumors have been demonstrated by both histology and genetic profiling.[92–96]

ECM surrounding breast tumors differs not only in biochemical composition from that of normal tissue but also in physical properties, notably stiffness.[97] A recent study correlated the stiffness of and around breast tumors with their aggressiveness.[76] The effect of stiffness on cell spreading and migratory capacity has been well studied on 2D substrates.[98,99] Such studies have also been undertaken in more physiologically relevant 3D environments, though isolating effects of stiffness from those of ligand availability and network architecture is a significant challenge in the 3D context.[100–104]

Beyond differences in composition and stiffness, the ECM surrounding invasive breast tumors also demonstrates changes in network architecture relative to normal ECM. Increased deposition of fibrillar collagen may lead to decreased porosity near the tumor. Moreover, cellular remodeling of fibrillar collagen may lead to heterogeneities in density and network organization. Indeed, architectural changes in ECM have been correlated with breast cancer prognosis. Alignment and orientation of collagen I fibers perpendicular to the tumor boundary has been associated with recurrence after surgical excision and metastasis, and breast cancer cells have been shown to migrate preferentially along radially aligned collagen fibers at the interface of the primary tumor and ECM.[77,78]

In sum, accumulating evidence suggests that the presence and particular organization of fibrillar collagen I is a marker of and a causal factor in breast cancer invasion. Here, we dissect the contributions of biophysical properties of fibrillar collagen I to the invasion efficiency of breast cancer cells. In particular, the invasion of triple negative highly aggressive breast adenocarcinoma cells (MDA-MB-231) cultured as multicellular tumor spheroids in both 3D (cells immersed within a matrix) and pseudo-3D (cells placed atop a thick matrix) settings was studied. The multicellular

invasion efficiency as reflected by invasive distance was analyzed. Invasive mode as reflected by cell polarization, establishment of protrusions, and ECM rearrangement on both the spheroid and single cell level was also investigated. The 3D matrices employed were composed of either fibrillar collagen I, non-fibrillar basement membrane extract (BME), or a mixture of collagen I and BME. The matrices were prepared so as to exhibit stiffnesses that varied over two orders of magnitude and displayed distinct network architectures with varying porosity and fibrillar dimensions.

3.2 Results

To establish the range of ECM composition, mechanical properties, and network architectures that support multicellular spheroid invasion of triple negative breast adenocarcinoma (MDA-MB-231) cells, we studied spheroid invasion in fibrillar (collagen I), non-fibrillar (BME), and composite matrices in both true 3D (cells immersed within the matrix) and pseudo-3D scenarios (cells placed atop a thick matrix) (Figure 4a and b).

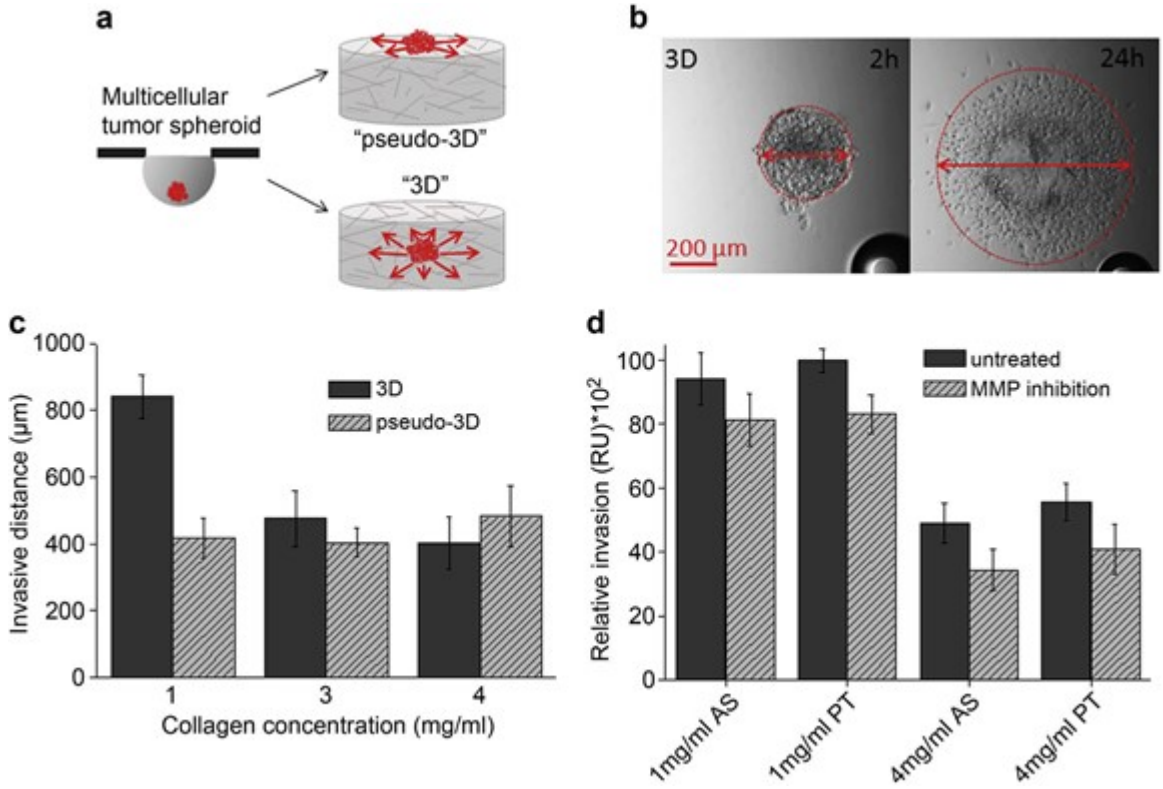

Figure 4 MDA-MB-231 spheroid invasion in 3D collagen matrices with different collagen concentrations. (a) Experimental setup for invasion analysis of a spheroid on top ("pseudo-3D") and within ("3D") biopolymer gels. (b) Transmitted light images of a representative spheroid implanted in a collagen gel at two hours and 24 hours after implantation. Red line depicts the diameter of the spheroid before and after invasion. Invasive distance is defined as the difference between these diameters. Scale bar = 200 µm. (c) Spheroid invasion at 24 hours in 3D (solid) and pseudo-3D (shaded) PT collagen gels. Mean values ± SD are shown, sample number n > 15 for every 3D condition and n > 5 for every pseudo-3D condition. (d) Comparison of spheroid invasion at 24 hours in 3D AS and PT collagen without (solid) and with (shaded) protease inhibition. Relative mean values normalized to the 1.0 mg/mL PT untreated control ± SD are shown. n = 6 - 10 for every condition.

3.2.1 Impact of physical matrix characteristics on 3D spheroid invasion

The impact of collagen concentration on spheroid invasion in fibrillar pseudo-3D and true 3D settings over 24 hours was assessed using pepsin-treated (PT) collagen to generate the matrices. In pseudo-3D, the invasion showed no statistically significant dependence on collagen density. In contrast, for spheroids embedded in these environments, where the full 3D architecture of the network plays a role, a clear decrease of invasion with increasing collagen concentration was seen (Figure 4c). We suggest that the physical constraints of the system imposed by the increased number of collagen fibers and resulting dense meshwork limit the invasive behavior.

To dissect the contributions of stiffness and various aspects of network architecture to spheroid invasion efficiency, invasion in a tunable acid-solubilized (AS) collagen system was investigated. First, we established that invasion as a function of collagen concentration in 3D AS collagen gelled at 37˚C mirrors that in 3D PT collagen as shown in Figure 4c. When gelled at 37˚C, 1.0 mg/mL AS collagen matrices have comparable viscoelasticity and pore size to PT collagen gels of the same concentration. Biochemically, AS collagen differs from PT collagen in that its monomers bear non-helical telopeptides that are sites for enzymatic cross-linking. We compared MDA-MB-231 spheroid invasive distances and invading cell morphology in telopeptide-intact (AS) and -deficient (PT) collagen gels of 1.0 mg/mL and 4.0 mg/mL collagen with and without pharmacological protease inhibition. We found that the presence of telopeptides did not influence invasion efficiency in 3D collagen matrices at either concentration (Figure 4d). The migratory phenotype observed was very similar in all cases: cells emerging from the spheroid were polarized and invaded individually, generally in an axial orientation relative to the spheroid. At 24 hours after implantation, some cells well beyond the periphery of the spheroid demonstrated

a stellate morphology bearing long filopodia while other cells were round. In both AS and PT collagen at 1.0 and 4.0 mg/mL, a mixed population of strongly polarized and round cells was evident, with no clear difference in the proportion of cells of each morphological class in these environments. Moreover, in AS and PT collagen at 1.0 and 4.0 mg/mL collagen, the effect of protease inhibition on invasive distance was limited (Figure 4d), and no obvious morphological changes were detected in the invading cells. Given these results, AS and PT collagen matrices were considered comparable substrates for the cells, and a tunable AS collagen system was then employed to decouple the effects of stiffness and network architecture on invasion efficiency.

Matrix properties of AS collagen change substantially with gelation temperature. AS (and PT) collagen gelled at 37˚C yields a matrix of thin well-dispersed fibrils, while AS collagen gelled at lower temperatures results in a matrix of highly bundled fibers (Figure 5a).[105,106] While such gels have larger pore size relative to a gel of the same concentration formed at physiological temperature, they also have increased stiffness since elasticity depends on both network porosity and properties of the struts constituting the fibrillar network (Figure 5a; Table 1).[106]

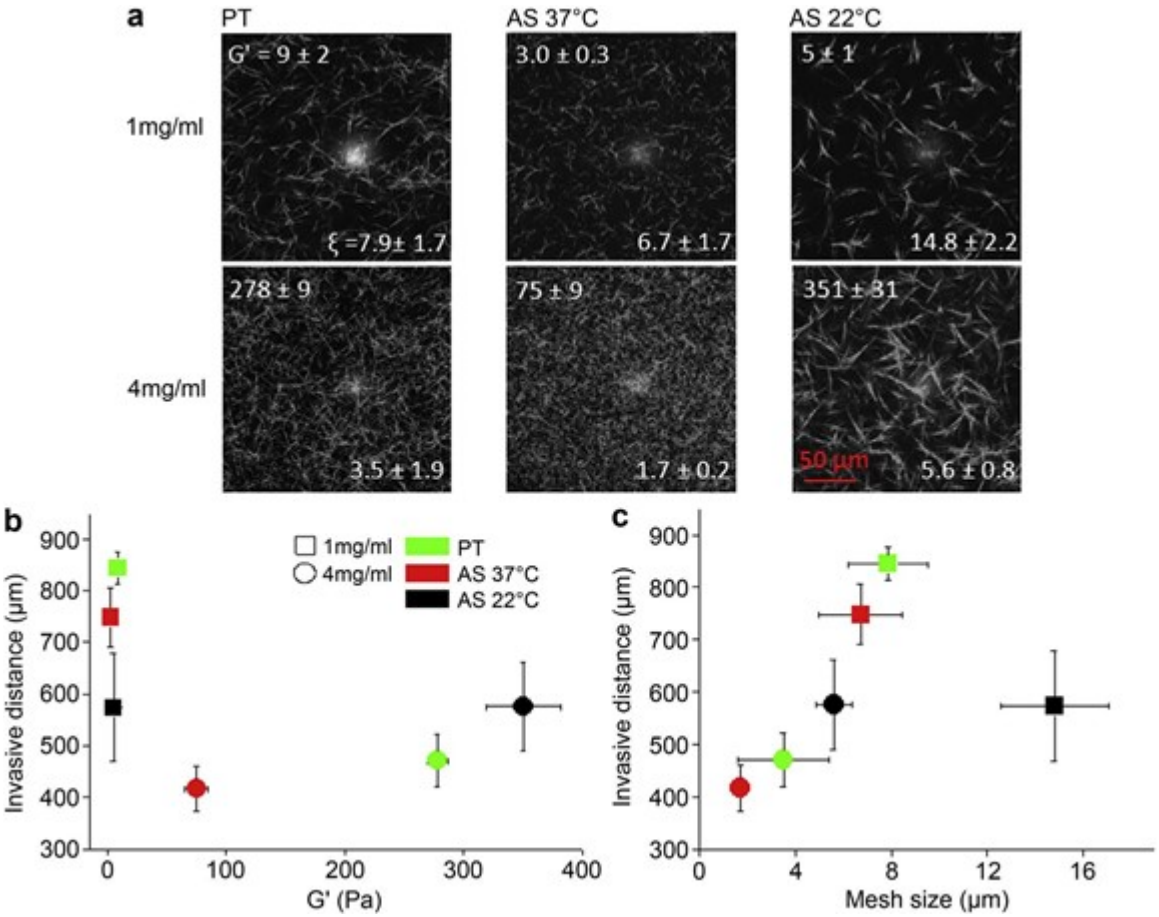

Figure 5 Dependence of invasion on fibrillar matrix biophysical properties. (a) CRM images of PT collagen (left), AS collagen gelled at 37˚C (middle), and AS collagen gelled at 22˚C (right) at 1.0 mg/mL (top) and 4.0 mg/mL (bottom). Bright spots visible in some CRM images are artifacts due to reflection from optical elements within the microscope and are removed prior to pore size analysis as described in Reference [113]. Scale bar = 50 µm. Text in the upper left corner of each panel shows the storage modulus G' (Pa) ± SD, and text in the lower right corner shows the average pore size ξ (µm) ± SD over n ≥ 5 gels. (b, c) Spheroid 3D invasive distance as a function of matrix (b) storage modulus, G', and (c) pore size, ξ. All values are given ± SD. Error bars are not visible if smaller than symbols. Legend in (b) applies to (b) and (c).

Matrix	*Storage modulus G' (Pa)*	*Pore size (μm)*
1.0 mg/ml AS 22˚C	5 ± 1	14.8 ± 2.2
1.0 mg/ml AS 37˚C	3.0 ± 0.3	6.7 ± 1.7
4.0 mg/ml AS 22˚C	351 ± 31	5.6 ± 0.8
4.0 mg/ml AS 37˚C	75 ± 9	1.7 ± 0.2
1.0 mg/ml PT	9 ± 2	7.9 ± 1.7
4.0 mg/ml PT	278 ± 9	3.5 ± 1.9
1.0 mg/ml BME	0.13 ± 0.05	N/A
3.0 mg/ml BME	0.8 ± 0.3	N/A
4.5 mg/ml BME[107]	3 ± 1	0.11 ± 0.07
1.0 mg/ml PT+1.0 mg/ml BME	12 ± 1	N/A
1.0 mg/ml PT+3.0 mg/ml BME	22 ± 3	N/A

Table 1 Matrix type, storage modulus G', and calculated pore size. For matrices containing BME, CRM cannot reveal pore size and therefore pore size is not available (N/A) for these gels except when reported elsewhere[107].

Analysis of invasive distances at 24 hours for spheroids embedded in each matrix type represented by Figure 5a revealed that spheroid invasion in 3D fibrillar collagen I matrices is a robust cellular behavior. Indeed, invasive distances at least as large as the initial spheroid diameter were measured in collagen gels with storage moduli spanning two orders of magnitude (3 - 350 Pa) and pore size spanning one order of magnitude (1.5 - 15 mm) (Figure 5; Table 1). Optimal

invasion was observed in 1.0 mg/ mL PT collagen, which is a highly compliant gel ($G^{'}$ = 9 Pa) with pore size approximating the MDA-MB-231 nuclear dimension (ξ = 8 μm, nucleus cross section = 6 - 8 μm).[108] Inspection of invasive distance as a function of collagen concentration, elasticity of the matrix, fiber thickness, and network pore size shows that among these variables pore size is the strongest determinant for MDA-MB-231 spheroid invasion efficiency in 3D fibrillar collagen systems (Figure 5b and c). Statistical analysis via Pearson's product-moment correlation demonstrated no significant correlation between invasion and storage modulus (r = -0.47); indeed three matrices with very similar low $G^{'}$ values exhibited a range of invasive capacity from moderate to maximal (Figure 5b). On the other hand, the pore size of the fibrillar matrix did correlate with invasion efficiency. This correlation was biphasic, and a positive Pearson correlation between pore size and invasion for a range of pore sizes from 1.5 to 9.6 μm was seen (r = 0.96). Optimal pore size was about 8 μm, and limited invasion was seen at both small pore sizes where steric constraints are expected to be important and at the largest pore size ($\xi \approx$ 15 mm) where reduced substrate availability may play a role. The degree of bundling of the collagen fibers did not have a clear effect on MDA-MB-231 spheroid invasion, with comparable invasion in matrices of similar pore size but different fiber thickness (Figure 5c).

The limited invasion observed in the smallest pore size environments suggests sub-nuclear pore size is a key rate-limiting factor during 3D invasion. If this is the case, cellular players involved in cell contraction are likely to be central for efficient 3D invasion. To test this hypothesis, cell migration was analyzed under inhibition of cell contractility by blocking myosin II phosphorylation through blebbistatin application.[109,110] Individual cells and spheroids under myosin II inhibition were subjected to Transwell migration assays utilizing stiff membranes of

defined pore size or invasion assays in collagen I matrices with comparable pore sizes. In these assays, MDA-MB-231 cells had obvious difficulty moving through 3 μm pores even without inhibition, showing that sub-nuclear pore size can strongly inhibit invasion (Figure 6a). Myosin II inhibition in these assays nearly abolished migration through restricting pores while reducing it about 40% in membranes with non-restricting pores (Figure 6a). Restricting pore size in collagen matrices had a lesser effect on spheroid invasion overall, and blebbistatin treatment caused a comparable reduction of invasion distance in collagen lattices with non-restricting average pore size (8 μm) and those with subcellular sized pores (3 μm) (Figure 6b). These findings suggested that the deformability of the pore and/or the presence of collagen fibers might assist tumor cells in invading physically constraining 3D environments.

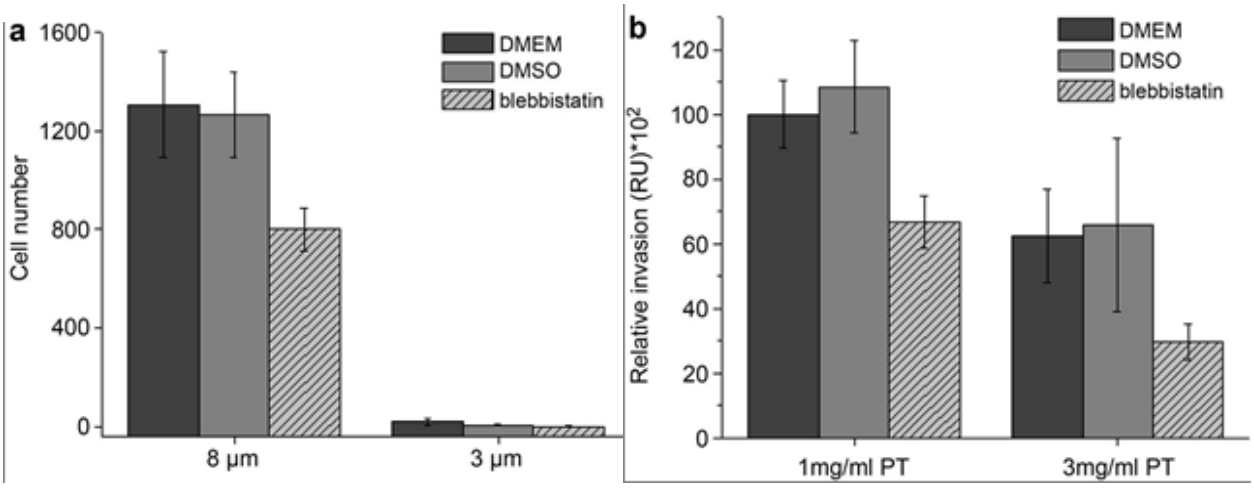

Figure 6 Role of myosin-driven cell contractility in MDA-MB-231 invasion. (a) Transmigration of MDA-MB-231 cells in Transwell assays with (shaded) and without (solid) blebbistatin-mediated myosin II inhibition. Graph shows average cell counts ± SD per field of view of cells migrated within 24 hours through a membrane with 8 µm or 3 µm pores. For quantification, 20 images were taken from each sample and conditions were tested in at least duplicate. (b) Spheroid invasion in low (1.0 mg/mL) and high (3.0 mg/mL) density collagen gels under blebbistatin-mediated myosin II inhibition. n = 4 - 6 for every condition.

3.2.2 Invasion mode and efficiency in non-fibrillar matrices

To investigate 3D invasion without the physical cues of collagen fibers, spheroid invasion assays were performed on pseudo-3D and in true 3D matrices composed of BME in various concentrations (Figure 7). BME consists primarily of laminin and collagen IV, which form sheet-like structures providing a dense meshwork with sub-micron pores [107,111,112], in contrast to the relatively large pore size, fibrillar architecture of collagen I networks. While the network architecture of BME gels is distinct from that of fibrillar collagen matrices, their viscoelastic

properties are similar, with the BME gels used in this study having comparable storage moduli to 1.0 mg/mL PT and AS (37˚C) collagen I matrices (Figure 7b, inset; Table 1).

MDA-MB-231 spheroids, which efficiently invaded all tested collagen systems, failed to invade the highly compliant BME matrices to a comparable degree at any chosen concentration (Figure 7). Placing the spheroids atop a BME matrix was not sufficient to rescue the invasive behavior, although the cells do not experience any steric hindrance in this pseudo-3D setting (Figure 7a). Thus, the dramatic reduction of tumor cell invasiveness in these non-fibrillar matrices is not due to the elastic properties of the matrix nor is it exclusively caused by the physical constraints experienced by the cells. Beside the strongly reduced invasion distance, the morphology of the invading front was greatly altered in BME in comparison to fibrillar collagen matrices in both pseudo-3D and true 3D scenarios. Both atop and within BME matrices, the hallmarks of individual mesenchymal migration were lost, and the tumor spheroid adopted a collective mode of invasion accompanied by reduced cell polarity at the invading front (Figure 7a).

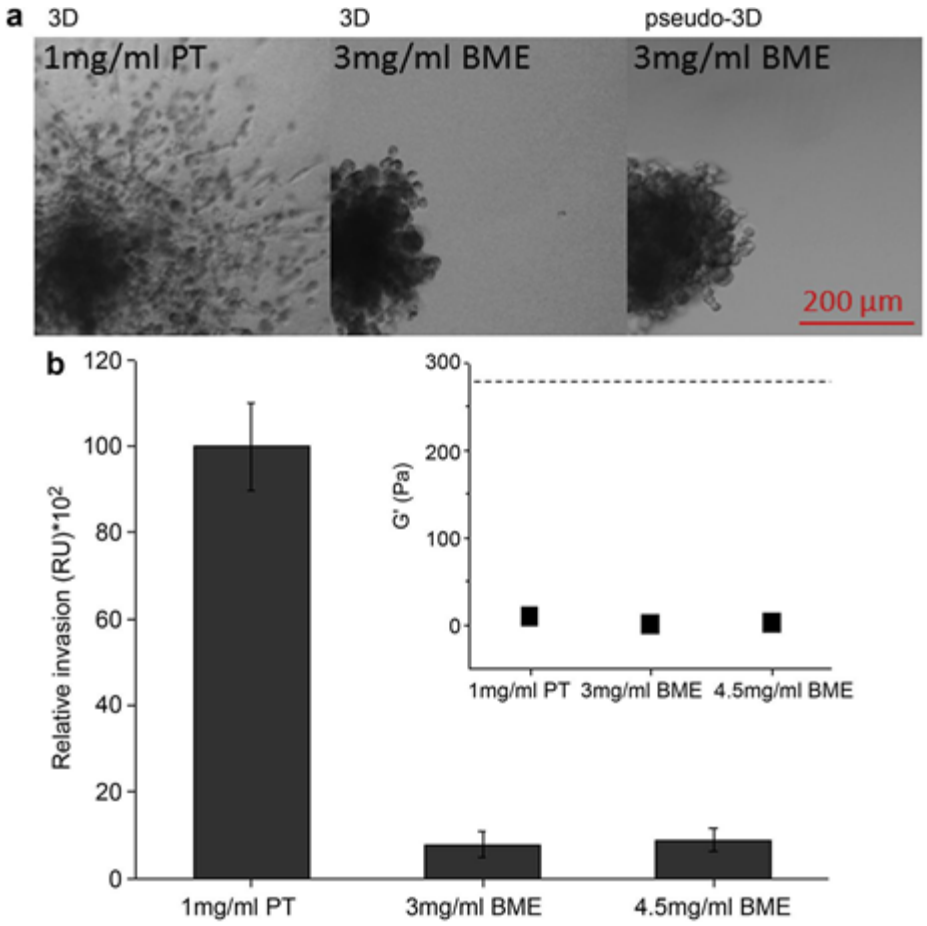

Figure 7 Spheroid invasion in non-fibrillar environments. (a) Representative transmitted light images of spheroids after 24 hours of invasion in 1.0 mg/mL collagen (left), in 3.0 mg/mL BME (middle), and on 3.0 mg/mL BME (right). Scale bar = 200 µm. A representative portion of each spheroid is shown to allow observation of full invasive distance. (b) Quantification of spheroid invasion in the non-fibrillar BME compared to invasion in fibrillar collagen matrix. $n \geq 5$ for each condition. Inset: Storage moduli ($G^{'}$) of 1.0 mg/mL PT collagen, 3.0 mg/mL BME, and 4.5 mg/mL BME; dotted line indicates the storage modulus of 4.0 mg/mL PT collagen. For these measurements, all sample chambers were precoated with the matrix employed.

To elucidate the molecular underpinnings of the differences in invasion mode and efficiency in collagen and BME, establishment of cell polarity and protrusions indicative of migratory behavior was assessed for individual cells within and atop fibrillar, non-fibrillar, and composite matrices. Cells were stained for actin cytoskeleton and categorized into polarized and non-polarized subpopulations by morphology and actin distribution at the cell periphery, with round cells lacking heterogeneous actin accumulation regarded as non-polarized (Figure 8 and Figure 9). Cell protrusions were categorized as actin-polymerization-based (filopodia) or actomyosin contractility-based (blebs), and the occurrence of such protrusions in the polarized and non-polarized cell subpopulation was determined. The population of polarized cells, which was predominant for cells both in and atop collagen matrices, was fully lost in the non-fibrillar BME environment regardless of whether the cells were within or atop the matrix (Figure 8b). The establishment of either type of cell protrusions was reduced by 90% in the non-fibrillar matrix. The loss of stable cell protrusions occurred also for cells atop the non-fibrillar gel, even though steric constraints for the cells were absent in this scenario (Figure 8c).

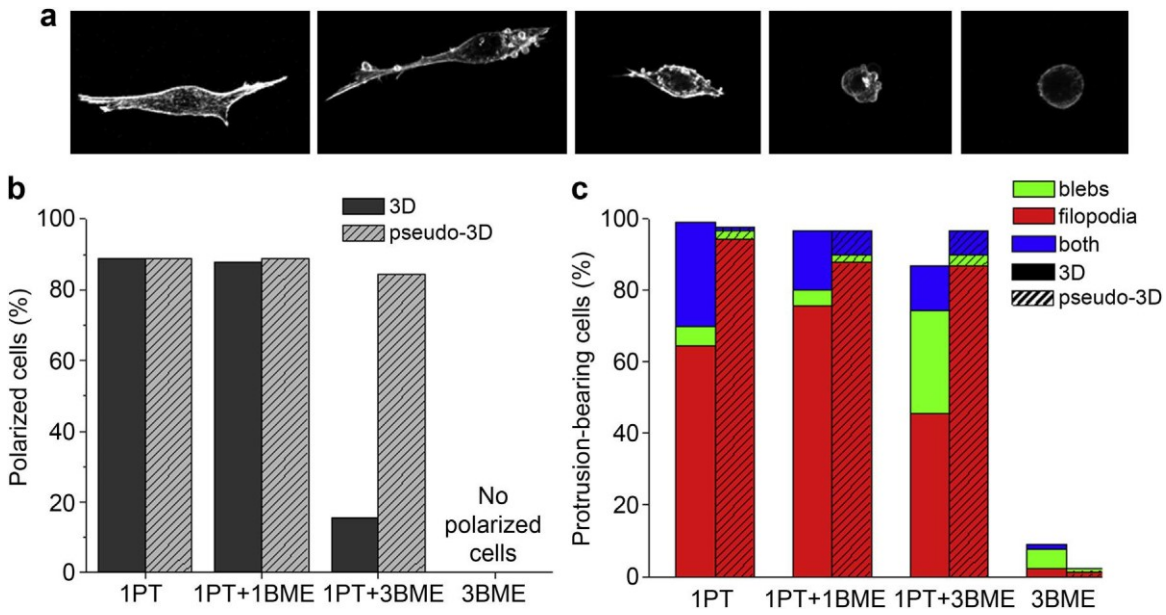

Figure 8 Cell polarity and cell protrusions in various 3D environments. (a) Representative confocal fluorescence maximum projections of phalloidin-stained MDA-MB-231 cells embedded in 3D matrices depicting the range of cell types observed. Left to right images depict a polarized cell with filopodia, two polarized cells with filopodia and blebs, a non-polarized cell with blebs, and a non-polarized cell lacking protrusions. Z-stacks from two phalloidin-stained cells depicting both the cell and surrounding collagen are shown in Figure 9. (b) Percentage of polarized MDA-MB-231 cells in various 3D (solid) and pseudo-3D (shaded) environments, n=90 with data pooled from two independent experiments. (c) Protrusion classes in various 3D (sold) and pseudo-3D (shaded) environments, n=90 with data pooled from two independent experiments.

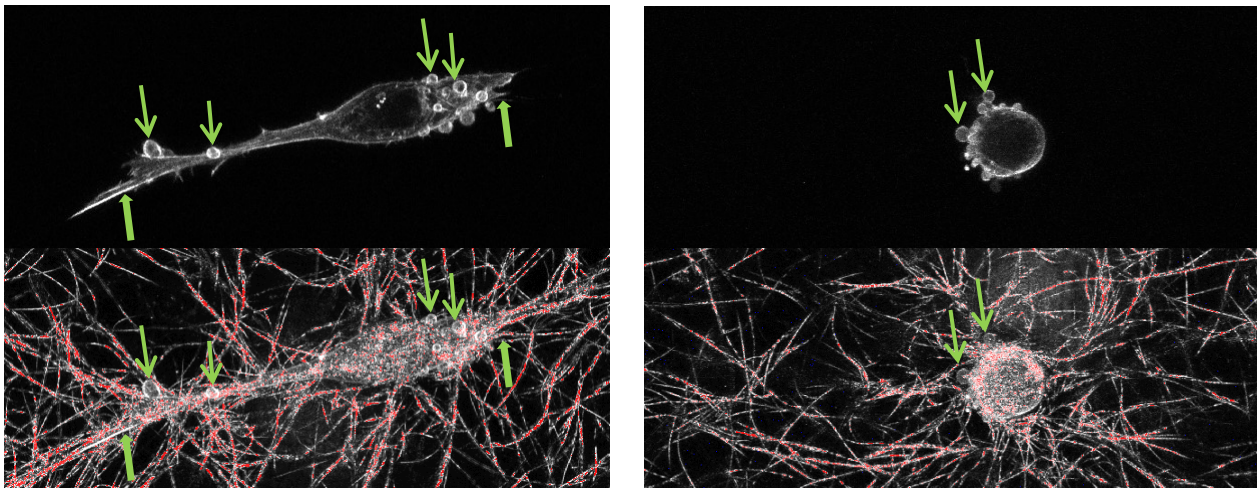

Figure 9 Cell morphology and protrusions in 3D matrices. Cells embedded in 3D matrices were fixed, and the actin cytoskeleton was stained with fluorescently labeled phalloidin. Z-stacks of cells and surrounding collagen were taken by recording slices every 2.5 µm with confocal fluorescence and reflectance microscopy, respectively. Two representative cells with different morphology and protrusions are shown. The upper panel shows the maximum projection of the fluorescence image only while the lower panel shows the overlaid fluorescence and reflectance maximum projections. The cell at left is polarized and bears both filopodia (block arrows) and blebs (line arrows); this cell is also shown in Figure 8. The cell at right is non-polarized and displays only blebs.

3.2.3 Effect of fibrillar collagen in establishing a migratory phenotype

The effects of the introduction of fibrillar collagen into the non-fibrillar BME matrix on cell polarity and protrusion formation were next assessed. To this end, cells were implanted in composite matrices consisting of collagen I and varying concentrations of BME. One type of composite matrix comprised 1.0 mg/mL PT collagen and 3.0 mg/mL BME (1PT + 3BME). This composite was expected to have the same steric constraints present in the 3.0 mg/mL BME matrix

plus a fibrillar matrix of PT collagen. Confocal imaging confirmed that collagen network architecture was similar in the presence and absence of BME (data not shown). The average storage modulus of the 1PT + 3BME gels was 22 Pa, somewhat higher than that of the corresponding non-composite gels, but more than an order of magnitude lower than the stiffest gels used in this study (Table 1). A second type of composite matrix composed of 1.0 mg/mL PT collagen and 1.0 mg/mL BME (1PT + 1BME) was also investigated. BME at 1.0 mg/mL formed a very weak gel ($G' = 0.13$ Pa) incapable of supporting a spheroid. The composite matrix had a storage modulus quite similar to that of PT collagen alone. The BME in this matrix was thus liquid-like and expected to have very limited effect on the network architecture of the gel.

The introduction of collagen fibers indeed reestablished polarity in cells on and in BME containing gels (Figure 8b). For cells within composite matrices, the ratio of polarized to non-polarized cells correlated with the storage modulus of the matrix, which depended on whether the BME was in the liquid-like (1PT + 1BME) or fully gelled (1PT + 3BME) state. A similar trend was observed for establishment of cell protrusions, with the proportion of filopodia to blebs decreasing with increasing BME concentration in the 3D scenario. The polarization and formation of cell protrusions of cells atop composite matrices were not influenced by the variations in compliancy and gelation state of the BME component as long as fibrillar collagen was present.

3.2.4 Invasion efficiency in composite matrices containing fibrillar collagen

Next, we analyzed whether the reestablishment of cell polarity and cell protrusions through the addition of fibrillar collagen was sufficient to reestablish spheroid invasion in pseudo-3D and true 3D composite matrices. In the pseudo-3D setting, the introduction of collagen fibers was

sufficient to fully rescue the invasive behavior of the spheroids regardless of the collagen:BME ratio. In the pseudo-3D composite matrices, invasive distance, morphology of the emigrating cells, and individual mode of migration were all comparable to those observed in 1.0 mg/mL PT collagen gels. In contrast, in a true 3D setting, invasion efficiency varied depending on the collagen:BME ratio (Figure 10). Although invasion in the high BME content composite matrix was significantly less than in a 1.0 mg/mL collagen I lattice, it was increased by a factor of three relative to that in the pure BME matrix of the same BME concentration. Importantly, the introduction of collagen fibers not only strongly increased invasive distance but also reconstituted the predominantly individual mesenchymal mode of migration observed in single component fibrillar matrices (Figure 10a). Interestingly, the 3D invasion observed over 24 hours correlated with the degree of collagen fiber reorganization that took place as early as 2 hours after spheroid implantation. In 1.0 mg/mL PT collagen, the most efficiently invaded environment studied, extensive collagen reorganization around the spheroid periphery was evident. Conversely, in composite matrices with high BME content, there was only limited early matrix reorganization and modest invasion (Figure 10b).

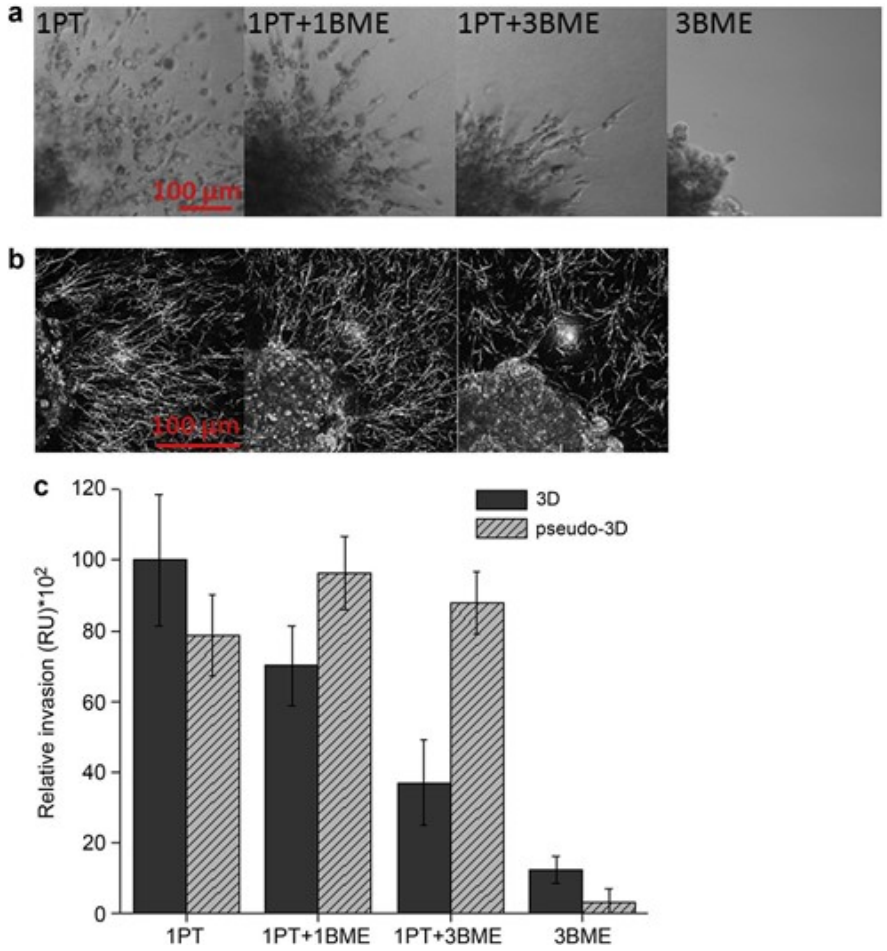

Figure 10 Spheroid invasion efficiency in and on BME matrices increases with introduction of fibrillar collagen. (a) Representative transmitted light images of spheroids after 24 hours of invasion in, from left to right, 1.0 mg/mL collagen (1PT), 1.0 mg/mL collagen + 1.0 mg/mL BME (1PT + 1BME), 1.0 mg/mL collagen + 3.0 mg/mL BME (1PT + 3BME), and 3.0 mg/mL BME (3BME). Scale bar = 100 µm. A representative portion of each spheroid is shown to allow observation of full invasive distance. (b) Representative CRM images of a representative portion of spheroids two hours after implantation in, from left to right, 1PT, 1PT + 1BME, and 1PT + 3BME. Scale bar = 100 µm. Spheroids in (b) are not the same as those shown in (a). (c) Spheroid invasion in (solid) and on (shaded) various fibrillar, non-fibrillar, and composite environments. $n \geq 9$ for each 3D condition, $n \geq 4$ for each pseudo-3D condition. For these measurements, all sample chambers were precoated with the matrix employed.

3.3 Discussion

In this study, the contributions of substrate stiffness, pore size, and especially fibrillar versus non-fibrillar network architecture to the efficiency and mode of tumor cell invasion were investigated.

Invasion of tumor spheroids placed atop (pseudo-3D) fibrillar matrices showed no clear correlation with collagen concentration while invasion within such matrices was limited at higher collagen concentrations, apparently by the steric constraints experienced by cells (Figure 4c). This is in accordance with other works on the impact of physical limitations on 3D invasion.[113–115] To more clearly differentiate the impact of steric (pore size) and mechanical (stiffness) matrix properties from the bulk substrate concentration, a tunable collagen system that allows pore size and compliancy to be modulated independent of collagen concentration was employed.[114] Analysis of invasion within this tunable collagen system demonstrated that in a true 3D environment the invasion-limiting impact of small pore sizes dominates over possible advantageous effects of higher stiffness or increased ligand availability present in high density matrices, an effect that cannot be assessed in 2D or pseudo-3D settings. While pore size smaller than nuclear size increasingly limited invasive distance, with very similar sensitivity to pore size seen across different cancer cell types[114,115], overall the invasive behavior of MDA-MB-231 spheroids in collagen gels was robust: only intermediate quantitative changes (≈ 2 fold) in invasive distance were evident and no obvious changes in migratory phenotype over a broad range of pore size, fiber dimensions, and substrate stiffness were observed (Figure 5).

Relatively effective invasion was seen even in cells invading high density gels with protease inhibition. Matrix metalloproteinases (MMPs) have been found to be deregulated and

have been proposed to play a role in the progression of multiple cancers including breast cancer.[116–118] Recent *in vitro* work suggested that inhibiting MMP activity in telopeptide-bearing AS collagen may abolish invasion while doing so in telopeptide-deficient PT collagen may force cells to adopt an amoeboid mode of invasion.[115] In this work, invasive distance of spheroids in collagen gels with (AS) or without (PT) intact telopeptides was comparable at both low (1.0 mg/mL) and high (4.0 mg/mL) collagen concentration (Figure 4d). Pharmacological inhibition of MMPs reproducibly reduced invasive distance in AS and PT collagen matrices by similar amounts and did not effect an obvious switch in migratory phenotype in any matrix type. The observation that protease inhibition limited invasion similarly in all collagen gels suggests roles for these proteases beyond that of collagen degradation.[119]

Though pore size was found to be the strongest determinant of invasion efficiency in 3D fibrillar matrices (Figure 5), the effect was less stark than would be expected from results seen in transmigration assays with and without blebbistatin-mediated inhibition of cell contractility (Figure 6). This may be related to the deformability of the collagen system and suggested that the presence of collagen fibers may assist cell migration through small pores. To test this hypothesis, cell invasion was measured in non-fibrillar (BME) and mixed fibrillar/non-fibrillar environments (collagen/BME composites) of similar elasticity.

MDA-MB-231 spheroids failed to efficiently invade 3D BME matrices at any concentration (2.5 - 9 mg/mL BME). The stiffness and pore size of BME matrices are correlated with its protein content, and while stiffness of employed BME matrices was comparable to low density collagen gels, average pore size in all cases is expected to be smaller than 1 μm.[107,111,112] While subcellular pore size in fibrillar collagen networks induced only a moderate quantitative

change in spheroid invasion (40 - 50%), the non-fibrillar environment led to a 90% reduction in invasive distance. Moreover, a qualitative switch of invasive mode from individual migration with a robust population of cells with typical mesenchymal phenotype to collective motion with few extended, polarized cells was seen (Figure 7), consistent with previous measurements of primary human breast carcinoma behavior.[120] This dramatic loss of invasive behavior cannot be explained by lack of appropriate surface receptors. MDA-MB-231 cells express clearly detectable amounts of α2β1 integrin[121], which apart from being a collagen I receptor can also bind laminin and collagen IV, the primary components of BME.[122] Moreover, high expression of α3β1 integrin, one of the main laminin-binding integrins, has been reported for MDA-MB-231 cells.[121,123] The failure to invade BME matrices was also not due to stiffness of the matrix, as BME gel storage moduli were comparable to those of collagen gels supporting significant invasion (Figure 7, Table 1, Figure 11). Interestingly, the invasive behavior was not reconstituted by placing the spheroids atop thick BME matrices, which offer the cells the same biochemical substrate without the physical constraints of the 3D environment. Thus, the failure of spheroids to invade the non-fibrillar BME matrix is not due primarily to physical constraints of subcellular pores or the absence of suitable cell surface receptors. We suggest instead that it is due to the lack of suitable spatial organization of adhesion ligands.

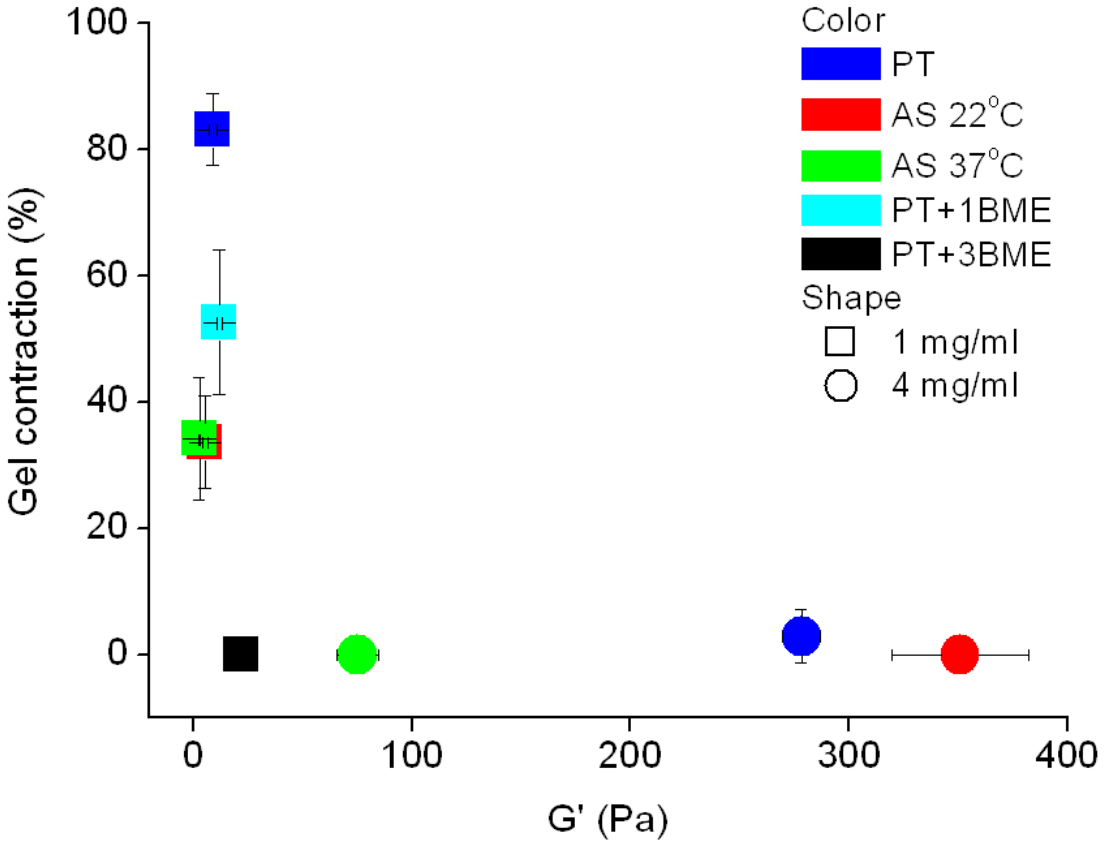

Figure 11 Analysis of correlation between the degree of matrix contraction by dispersed cells and the viscoelastic properties of the matrix as reflected by storage modulus, G'. Efficient gel contraction was observed exclusively for fibrillar matrices with low storage moduli.

Analysis of morphology and protrusions of cells implanted in and atop different types of 3D matrices support the view that organization of ligands is critical to establishing a migratory phenotype not only in but also on adhesive substrates. This analysis revealed that cell polarization and the formation of stable cell protrusions - two hallmarks of migratory behavior - were heavily compromised or fully lost in non-fibrillar matrices (Figure 8). As with invasion, the establishment of cell polarity and the formation of protrusions were compromised not primarily by the steric

constraints of the sheet-like BME matrix, as cell polarity was not rescued through plating cells atop the matrix. Rather, both cell polarity and protrusions were reestablished upon the introduction of fibrillar collagen into the BME matrix (Figure 8b). These results suggest that cell polarity and protrusions require the physical cues provided by the fibrillar substrate regardless of whether the cell is confronted with additional physical challenges. In true 3D environments, where steric constraints may be present, fibrillar architecture is necessary but not sufficient to fully reconstitute characteristics of 3D invasion seen in permissive fibrillar collagen environments. A strong reduction of the polarized cell population was seen with increasing BME content in collagen/BME composite matrices (Figure 8b). While the same increase in BME concentration resulted in only a minimally reduced percentage of protrusion-bearing cells, a clear shift from actin-polymerization-based protrusions (filopodia) to pressure-driven blebs, spherical protrusions that are associated with an alternate mode of cell motility[124], was evident. Taken together, these findings suggest that steric impairment of the environment counteracts and limits actin-polymerization-dependent processes employed in migratory behavior. These results demonstrate that efficiency of 3D invasion strongly correlates with cell polarization and type of cell protrusions on a single cell level, features that have previously been suggested to be indicators of metastatic potential.[125,126]

Cell polarization and adoption of a mesenchymal migratory phenotype also correlated with the degree cells reorganized the collagen matrix preceding invasion (Figure 10). In general, matrices in which rapid collagen rearrangement around the spheroid front occurred also supported efficient spheroid invasion. Interestingly, the collagen conditions that allowed for efficient reorganization did not fully coincide with the conditions in which significant matrix contraction through individual cells was observed (Figure 11 and Figure 12). While matrix contraction

strongly correlated with the viscoelastic properties of the matrix and took place only in fibrillar matrices with $G' < 10$ Pa, efficient spheroid reorganization and invasion was observed not only in those gels but also in the stiffest collagen gels investigated, those composed of fiber bundles (Figure 5a, Figure 12). Among all gels, including those supportive of invasion but not contracted in contraction assays, invasive distance correlated with degree of reorganization in the immediate environment of the spheroid (Figure 10). It remains to be clarified whether the ability for spheroids to reorganize collagen and invade a matrix that dispersed cells fail to contract is due to higher expression of mechanotransductory components by cells grown in aggregate, more efficient compartmentalization of these molecules, and/or the geometry of the spheroid front that encourages cell polarization through anisotropic presentation of ECM ligands around leading invasive cells. No matter the origin of these effects, these results as well as the demonstration of the importance of the full 3D network architecture on invasion efficiency underline the utility of multicellular aggregates as *in vitro* models for studying key events of the metastatic process.

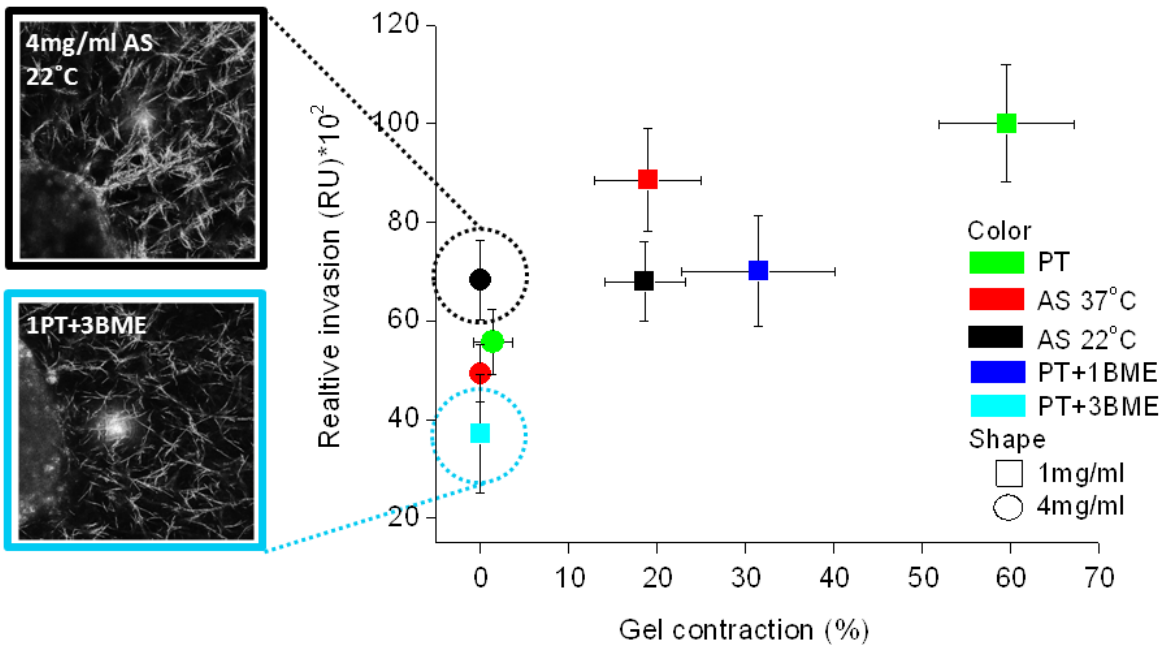

Figure 12 Analysis of correlation between spheroid invasion and degree of gel contraction by dispersed cells in various types of matrices. Both responses were measured at t = 24 hours. Mean values ± SD are depicted. While gels that were well contracted also supported significant invasion, some gels that could not be contracted also supported at least moderate invasion. The insets show CRM images of spheroids in two different 3D matrices at t = 2 hours after implantation. While neither of the depicted matrices (4 mg/ml AS collagen gelled at 22˚C and 1 mg/ml PT collagen + 1 mg/ml BME) was contracted by individual cells, the collagen matrix was efficiently reorganized by spheroids, while the composite matrix was not. The degree of matrix reorganization – but not degree of matrix contraction – correlated with the invasive efficiency of spheroids in the matrices. Matrices that were more readily reorganized were also more readily invaded.

3.4 Conclusion

This study elucidates the crucial role of the biophysical cues provided by fibrillar collagen for cancer cell invasion in sterically challenging environments. We demonstrate the dominant role of pore size over stiffness for invasion efficiency in fibrillar environments and the indispensable role of fibrillar substrate for invasion in composite matrices. The presence of collagen fibers assists tumor cells in invading otherwise unfavorable environments by inducing cell polarization and formation of stable cell protrusions. This study demonstrates that the presence of fibrillar substrate is sufficient to allow breast cancer cells to establish a migratory phenotype and invade environments that otherwise inhibit migration through steric constraints. Finally, we suggest that the 3D composite collagen and BME matrices introduced in this study may be particularly suitable systems for assessment of cell behavior as they test not only the effects of physical cues provided by fibrillar substrates and contributions of force generation but also can be tuned to probe cell ability to invoke alternate migratory phenotypes necessary in dense non-fibrillar environments.

4 Breast cancer cell line aggregate morphology does not predict invasive capacity

4.1 Introduction

Despite critical improvements in treatment and a strong trend towards early diagnosis in developed countries, breast cancer continues to be a leading cause of death worldwide. Almost all such deaths result from breast cancer metastasis to distant organs whose critical functions are compromised. This cancer progression occurs in several stages, but all localized breast cancers that become metastatic must invade locally before the intravasation that leads to metastasis to distant sites. That local invasion occurs first through the thin layer of basement membrane composed primarily of collagen IV and laminins that surrounds tumors and then through the dense extracellular matrix (ECM) of the breast that is dominated by the presence of fibrillar collagen I. Given that localized breast cancers can only become metastatic if they can breach the basement membrane and invade collagen I-rich environments, either basement membrane or collagen I may be an appropriate *in vitro* environment in which to assess a breast cancer's ability to invade. Many studies on normal and pathological breast cell development are performed in 3D environments of basement membrane extract (BME), also known as laminin-rich ECM.[100,127–138] These studies follow from pioneering work on breast cancer that was crucial in establishing the importance of cellular microenvironment and specifically, dimensionality on cell behavior.[139–142]

Several years ago, a promising assay to identify breast cancer cells with invasive capacity that utilized 3D BME was reported.[82,143,144] This work correlated cell aggregate morphology in 3D BME with gene expression signatures.[38,82] While cells cultured on 2D plastic were reported

to appear nondescript, cell aggregates allowed to develop in 3D BME formed one of four morphological classes: stellate, grape-like, mass, or round.[82] This study evaluated 25 available cell lines and showed that aggregate morphology – from most (stellate) to least (round) aggressive – correlated with some measures of cell invasive capacity, primarily the Transwell migration assay in which cells migrate through a pore-bearing membrane along a nutrient gradient. Moreover, this work showed that cells with similar aggregate morphologies were frequently grouped in hierarchical gene clustering, which itself has been shown to have some prognostic significance.[29,145] These observations suggested the utility of 3D aggregate morphology as a proxy for cell invasive capacity, possibly with translational value.

We assessed whether aggregate morphology correlated with invasive capacity in *in vitro* assays beyond the Transwell assay. In particular, we investigated correlation between cell aggregate morphology and multicellular invasion in 3D collagen I matrices that recapitulate key biophysical aspects of the *in vivo* stromal breast tissue. In spite of the rich history of using BME in breast cancer cell studies and the promising assay described above, collagen I-rich environments may be more appropriate settings in which to study key events in breast cancer progression.[146] Indeed, accumulating evidence shows that density and particular organization of collagen I is causally related to both breast cancer risk and poor prognosis.[75,147] Moreover, a tumor associated collagen signature (TACS-3) characterized by bundled collagen fibers aligned perpendicular to the tumor/stromal boundary was recently shown to correlate with poor patient outcome.[77,78,147–151]

We investigated morphological characteristics and dynamic behavior of six cell lines that had been reported to adopt either stellate (MDA-MB-231, Hs 578T, and MDA-MB-157) or grape-

like (MDA-MB-468, ZR-75-1, and MDA-MB-453) aggregate morphologies in BME in earlier work.[82] We examined whether morphology on 2D or in 3D predicts migratory capacity in two contexts. Specifically, we performed cell morphology assays in isolation and in aggregate on 2D glass and in 3D BME or collagen I environments followed by 2D migratory and 3D traction generation and invasion assays. This study reveals that while 2D morphology in aggregate (and in some cases in isolation) is sufficient to predict 3D morphology in both isolation and aggregate, 3D aggregate morphology is not predictive of invasive capacity in 3D collagen. Examples of cells with discordance in stationary and migratory phenotype were identified, with one cell line with stellate aggregate morphology lacking invasive capacity and one cell line demonstrating grape-like aggregate morphology showing high invasive capacity in collagen I environments. We suggest invasion in collagen I environments can predict ability to invade in vivo.

4.2 Results

4.2.1 2D and 3D isolated and aggregate morphology are correlated

Six breast cancer cell lines were investigated in this work, three that were previously identified as demonstrating stellate aggregate morphology (MDA-MB-231, Hs 578T, MDA-MB-157) and three that were identified as demonstrating grape-like aggregate morphology (MDA-MB-468, ZR-75-1, and MDA-MB-453 cells) in BME.[82] Key characteristics of the cell lines employed in this study are shown in Table 2.

Cell line	Receptor status* ER PR HER2	Aggregate morphology[+]	Aggregate morphology[#]
MDA-MB-231	- - -	stellate	stellate
Hs 578T	- - -	stellate	stellate
MDA-MB-157	- - -	stellate	stellate
MDA-MB-468	- - -	grape-like	grape-like
ZR-75-1	+ - - /+ + -	grape-like	mass
MDA-MB-453	- - - /- - +	grape-like	grape-like

Table 2 Characteristics of cell line investigated: receptor status and aggregate morphology.

*Tumor receptor status: + = positive and - = negative for ER = estrogen receptor, PR = progesterone receptor, and HER2 = human epidermal growth factor receptor 2. In cases where discrepancy between reports is present across publications, both reported receptor statuses are shown.[82,190]

[+]Aggregate morphology in a "3D on top" BME assay (cells on a BME gel and covered with an additional thin layer of BME) as reported by Kenny et al.[82]

[#]Aggregate morphology on 2D glass and in 3D 1.0 mg/mL collagen I matrix from this study.

Cell aggregate morphology was first analyzed in 3D BME. Most cell lines were found to exhibit the same aggregate morphology as reported previously despite a somewhat different approach to aggregate preparation compared to that presented in previously published studies (Figure 13).[82,143] MDA-MB-231 and Hs 578T cells were stellate in BME. MDA-MB-157 cells exhibited some aspects of stellate aggregate morphology, their reported morphology, though their extension was less pronounced than the other two cell lines in this category. Among the cell lines previously reported to form grape-like cell aggregates, MDA-MB-453 cells displayed clear grape-

like aggregate morphology while MDA-MB-468 and ZR-75-1 cells displayed aspects of grape-like and mass aggregate morphology, with some flattening of the cells at points of cell-cell contact.

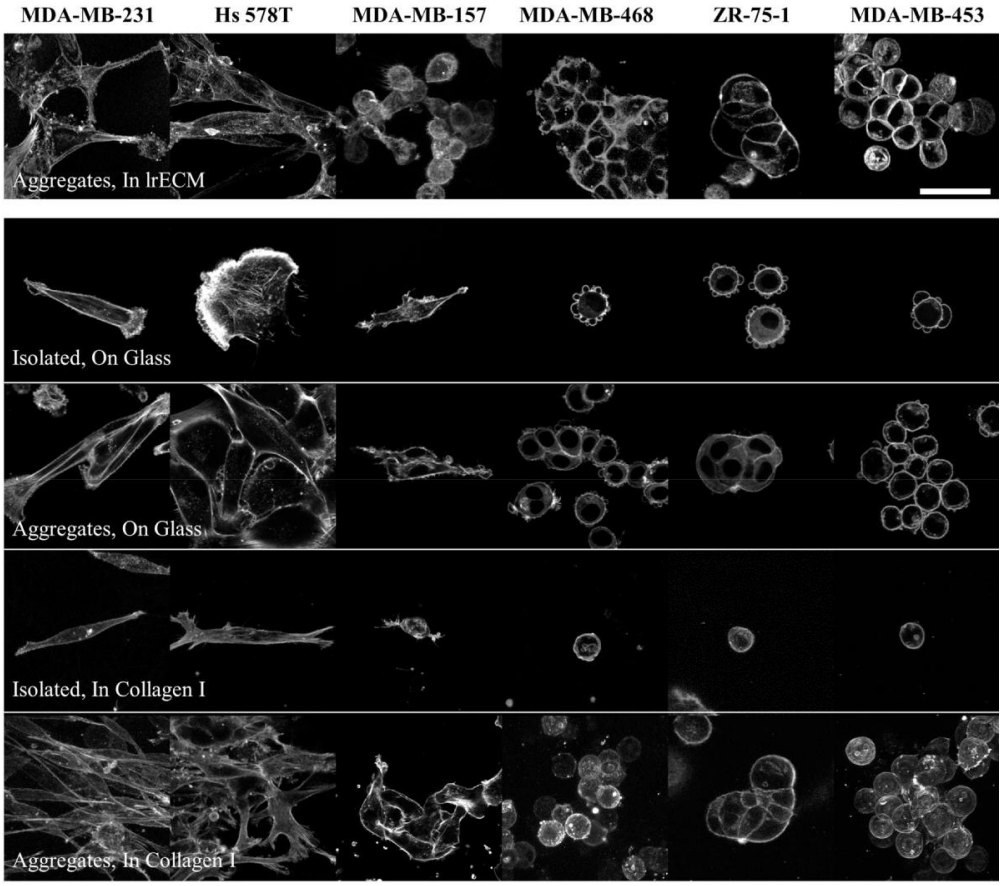

Figure 13 Morphology of representative isolated cells and aggregates of each investigated cell line in 3D 10 mg/mL BME, on 2D glass, and in 3D 1.0 mg/mL collagen I matrices. Cells were fixed after 24 hours of culture and stained for F-actin. Scale bar is 50 μm.

Cells from each cell line were next cultured on 2D glass. MDA-MB-231 and MDA-MB-157 cells cultured at low density on this surface typically displayed an extended spindle-like cell body with protrusions at the leading and trailing edges, while Hs 578T cells were flatter, less anisotropic, and showing lamellipodial ruffling. Cells of these three cell lines retained similar

morphologies when cultured at higher densities that allow for cell-cell contact and aggregate formation, with the MDA-MB-231 and MDA-MB-157 cells showing significant alignment along their long axes, a signature of stellate aggregate morphology. Cells previously identified as grape-like in 3D BME culture were round and demonstrated bleb-like protrusions when cultured in isolation on the 2D substrates. At higher density on these substrates, MDA-MB-453 and MDA-MB-468 cells displayed classical grape-like aggregate morphology while ZR-75-1 cells demonstrated mass aggregate morphology.

In 3D 1.0 mg/mL collagen gels, MDA-MB-231 cells displayed very similar appearance both in isolation and in aggregate to that displayed on the 2D substrate. Hs 578T cells in 3D collagen adopted a thinner, more extended morphology in isolation in 3D collagen I than on 2D. In aggregate these cells demonstrated stellate aggregate morphology in 3D collagen I although there was somewhat less alignment along the long axes of the cells than was obvious in the MDA-MB-231 aggregates. Like MDA-MB-231 cells, MDA-MB-157 cells looked very similar when cultured on 2D and in 3D collagen I. While these cells were anisotropic, there was less extension than in the other two stellate cell lines described and less alignment along a particular direction. The three cell lines that demonstrated round morphology in isolation when cultured on 2D continued to do so when cultured in 3D collagen I. They also demonstrated very similar aggregate morphology on 2D and in 3D culture, with the MDA-MB-453 and MDA-MB-468 cells demonstrating typical grape-like aggregate morphology, and ZR-75-1 demonstrating mass aggregate morphology.

In sum, the three cell lines investigated that had been identified as demonstrating stellate aggregates in 3D BME also do so in 3D collagen I. Two of the three cell lines that had previously

been identified as demonstrating grape-like aggregate morphology in BME do so in 3D collagen I, while one (ZR-75-1) yields mass aggregates. In all cases, aggregate morphology displayed by cells cultured in 2D on glass is a good predictor of 3D aggregate morphology in collagen I matrices. As such, if 3D aggregate morphology is a predictor for invasive capacity, the even simpler assay of aggregate morphology on 2D may be similarly predictive.

4.2.2 Isolated and aggregate morphologies are uncorrelated with 2D migratory behavior

The correlation between isolated and aggregate cell morphology and migratory speed was tested in 2D cell exclusion zone/gap assays. Migratory mode (collective vs. individual migration) and speed of gap closure may be expected to correlate with aggregate morphology as both depend in part on the number and strength of cell-cell and cell-environmental contacts.

Among cells with stellate aggregate morphology in 3D collagen I and on 2D tissue culture treated glass, the MDA-MB-231 cells migrated most rapidly. After six hours, the cell front of the MDA-MB-231 monolayers had closed substantially, with select cells having reached the center of the gap, and by 24 hours, the gap was completely filled in (Figure 14). The Hs 578T and MDA-MB-157 cells also migrated individually, though more slowly than the MDA-MB-231 cells. Some cells had spanned the gap by 24 hours but the gap was not completely filled in by that time point. Cell lines that adopted round morphology in isolation and demonstrated grape-like or mass morphologies in aggregate showed more discrepancy in migratory speed and migratory mode. MDA-MB-468 cells closed the gap very quickly, at a rate similar to MDA-MB-231 cells. Individual cells spanned the gap by six hours and the gap was fully filled in by 24 hours. ZR-75-1 cells migrated collectively with a sheet-like front. These cells required more than 48 hours to close

the gap. MDA-MB-453 cells did not appear to migrate, but did proliferate minimally into the gap over 48hours.

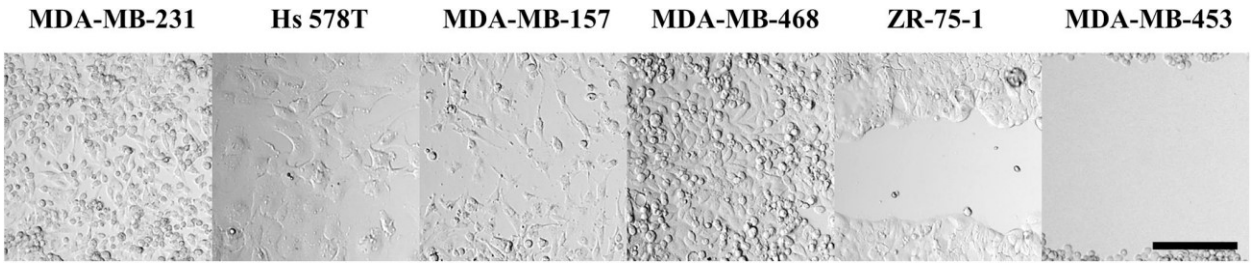

Figure 14 Transmittance images of cells from each cell line investigated in a cell exclusion zone assay at 24 hours. Initial gap distance is 500 μm, the height of the images. Scale bar is 200 μm.

In sum, while we found strong correlation between 2D and 3D morphologies both in isolation and aggregate, we found limited correlation between aggregate morphology and migratory speed in the gap assay. The MDA-MB-231 and MDA-MB-468 cells were the fastest to traverse the gap, though they are from different aggregate morphology classes. Moreover, cell lines that formed grape-like aggregates represented cells both among the fastest (MDA-MB-468) and slowest (MDA-MB-453) in this assay.

4.2.3 Isolated and aggregate morphologies are uncorrelated with 3D invasion in collagen

While no correlation between morphology and 2D migratory speed was observed, given that correlation was seen previously between aggregate morphology and invasive capacity in Transwell assays, it is possible that the dimensionality of the migratory or invasive assay is critical in revealing correlations between cell morphology and invasive behavior. We assessed 3D invasive

capacity through spheroid invasion assays in collagen I environments. In such assays, both cell-cell and cell-environmental contacts found *in vivo* are recapitulated.

The ability of cell lines to form spheroids speaks in part to their capacity to form tight cell-cell adhesions. Interestingly, cells that demonstrate stellate aggregate morphology tend to form tight spheroids well. In the most commonly used method to produce spheroids, hanging drop culture, while all three stellate cell lines formed compact spheroids, none of the other cell lines did. As such, a different approach to generate spheroids was used that was suitable for all cell lines, as described in section 2.7.1.[152]

Images of representative spheroids at 2 and 24 hours after implantation into the collagen I gels are shown in Figure 15. At the two hour time point, initial invading cells were seen in MDA-MB-231 and Hs 578T spheroids (Figure 15a). At this same time point, evidence of cells generating traction on surrounding collagen was seen in most cell lines, as evidenced by collagen fibers aligned radially near the spheroid edge. This alignment was seen not only in the cell lines with early onset of invasion (at two hours) but also in MDA-MB-157, MDA-MB-468, and ZR-75-1 spheroids. Only the MDA-MB-453 spheroids appeared surrounded by an isotropic matrix at this time point.

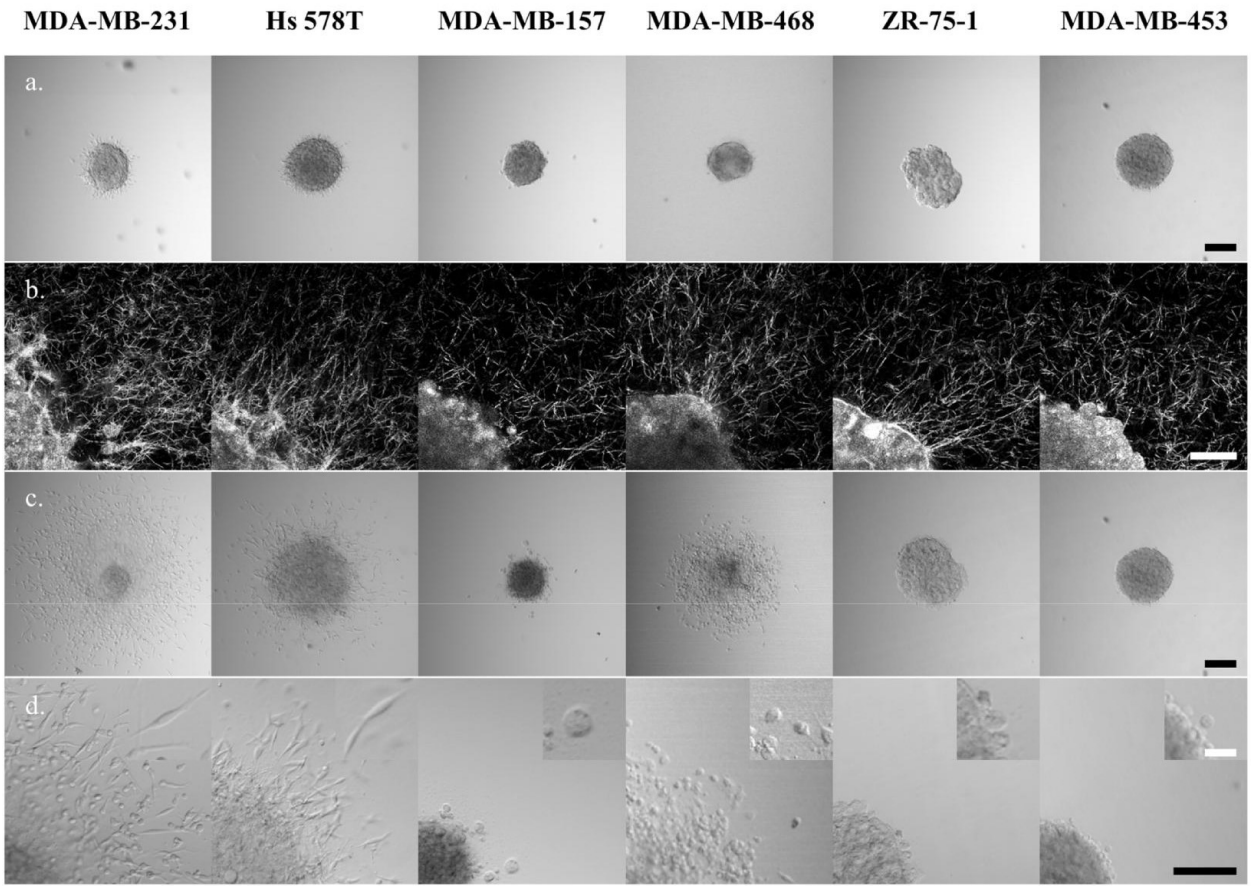

Figure 15 Spheroids of each investigated cell line at 2 hours and 24 hours after implantation in 1.0 mg/mL collagen I. (a) Transmittance images at 2 hours. (b) Confocal reflectance images of collagen surrounding the spheroids (and a portion of the spheroid in the lower left corner) at 2 hours. (c) Transmittance images at 24 hours. (d) Magnified view of cells invading from the spheroid at 24 hours. Additional magnification shown in the inset highlights invading cell morphology. Black scale bars = 200 μm and white scale bars = 50 μm. Confocal reflectance images (row b) have had an optical artifact that causes a bright spot in the center of the field of view removed by replacement of this spot with a representative area from elsewhere in the image.

Three of the cell lines investigated were found to substantially invade 3D collagen I matrices within 24 hours after spheroid implantation: MDA-MB-231, Hs 578T, and MDA-MB-468, the first two of which form stellate and the last grape-like aggregates. Of all cell lines investigated, when prepared as spheroids the MDA-MB-231 cells were most invasive, both in terms of cell speed and invasive cell density. Moreover, the original spheroid core largely disassembled as cells from that core disseminated into the surroundings, indicative of particularly aggressive invasive behavior. The invasive MDA-MB-231 cells primarily adopted a stellate morphology during invasion, and many cells invaded a distance of 400 μm within 24 hours, a rate of approximately 0.3 μm/min, similar to that reported previously for single cells in a similarly dense collagen I environment.[153]

The other cell lines with stellate aggregate morphology displayed different invasive behaviors. Hs 578T spheroids demonstrated substantial invasion with cells exhibiting primarily stellate morphology, invading moderately quickly and at moderate density in comparison to the MDA-MB-231 cells. Unlike in MDA-MB-231 spheroids, the dense spheroid core did not disseminate but instead expanded substantially over the 24 hours. The third cell line with stellate aggregate morphology, MDA-MB-157, demonstrated very limited invasion with only a few (round) cells dispersing from the spheroid core.

The cell lines that adopted round morphology in isolation also displayed a diversity of invasive behaviors. MDA-MB-468 spheroids invaded efficiently, with round but polarized cells that dispersed approximately as quickly as Hs 578T cells and as densely as MDA-MB-231 cells into the surrounding collagen matrix. In contrast, ZR-75-1 cells and MDA-MB-453 cells showed no clear evidence of invasion in these collagen I environments.

4.2.4 Cell contractility is necessary but insufficient to predict invasion in collagen surroundings

In the spheroid assay, of the cells with stellate aggregate morphology, MDA-MB-231 and Hs 578T cells invaded successfully. The invasive cells of both cell lines demonstrated typical mesenchymal invasion, with strongly polarized morphology and a motility cycle in which tractional forces were generated on their surroundings before the cell body was pulled forward. The tractional force generation was evidenced by remodeling of surrounding collagen fibers into radial patterns around the spheroid within several hours of spheroid implantation and before notable invasion (Figure 15b). Of the three cell lines in which cells demonstrated round morphology in isolation and grape-like or mass morphology in aggregate, again there was no clear correlation between aggregate morphology and invasion in the spheroid assay. Among these cells, MDA-MB-468 cells invaded the collagen gels with similar speed to the Hs 578T cells and similar density to the MDA-MB-231 cells. The other three cell lines (MDA-MB-157, ZR-75-1, and MDA-MB-453) showed limited or no invasion in the spheroid assay. The MDA-MB-468 cells migrated with a different phenotype than the MDA-MB-231 and Hs 578T cells, exhibiting round morphology during the majority of the migratory cycle and bleb-based protrusions instead of the filopodia and related actin-driven protrusions seen in typical mesenchymal invasion. Despite this bleb-mediated migratory mode, the cells did appear to pull on collagen fibers in their environment (Figure 15b), suggesting that traction generation is also important in this migratory mode. These observations suggested that ability to generate traction on and reorganize collagen fibers is a necessary activity to allow for invasion in the spheroid assay. To test this hypothesis, integrin profiling and collagen contractility assays were performed.

The integrins that preferentially bind to collagen contain the β1 subunit. As measured via fluorescence-activated cell sorting (FACS), all cell lines assessed in this study have significant amounts of β1 integrin, with particularly high levels seen in the MDA-MB-231 and Hs 578T cells (Figure 16). Most cell lines also have significant amounts of the α2 subunit that pairs with the β1 subunit to form the α2β1 integrin that is the functional receptor for collagen I fibrils.[60] The exception is the MDA-MB-157 cell line. In all cases, the level of α2 subunit was limiting and paralleled the detected level of α2β1 integrins. The presence of significant levels of α2β1 integrins in all cell lines but MDA-MB-157 suggests that each of the other cell lines has the capacity to generate traction on and reorganize collagen I. We also measured the levels of other subunits that when coupled with the β1 subunit may bind to collagen: α1, α10, and α11.[154] No cell line exhibited high levels of these integrin subunits, though MDA-MB-231 and Hs 578T cells exhibited detectable levels of α1 integrins. The integrins that are relevant for collagen I binding are the same ones relevant for binding collagen IV and laminin, the key components of basement membrane and laminin-rich ECM.[155] As such, integrin requirements for invasion in collagen I environments are expected to be similar to those in BME. The results presented in Figure 16 suggest that each cell line, save MDA-MB-157, has the capacity to adhere to and generate traction on collagen I fibrils. Thus, the expression level of suitable integrins did not distinguish invasive from noninvasive cells in the collagen I environment.

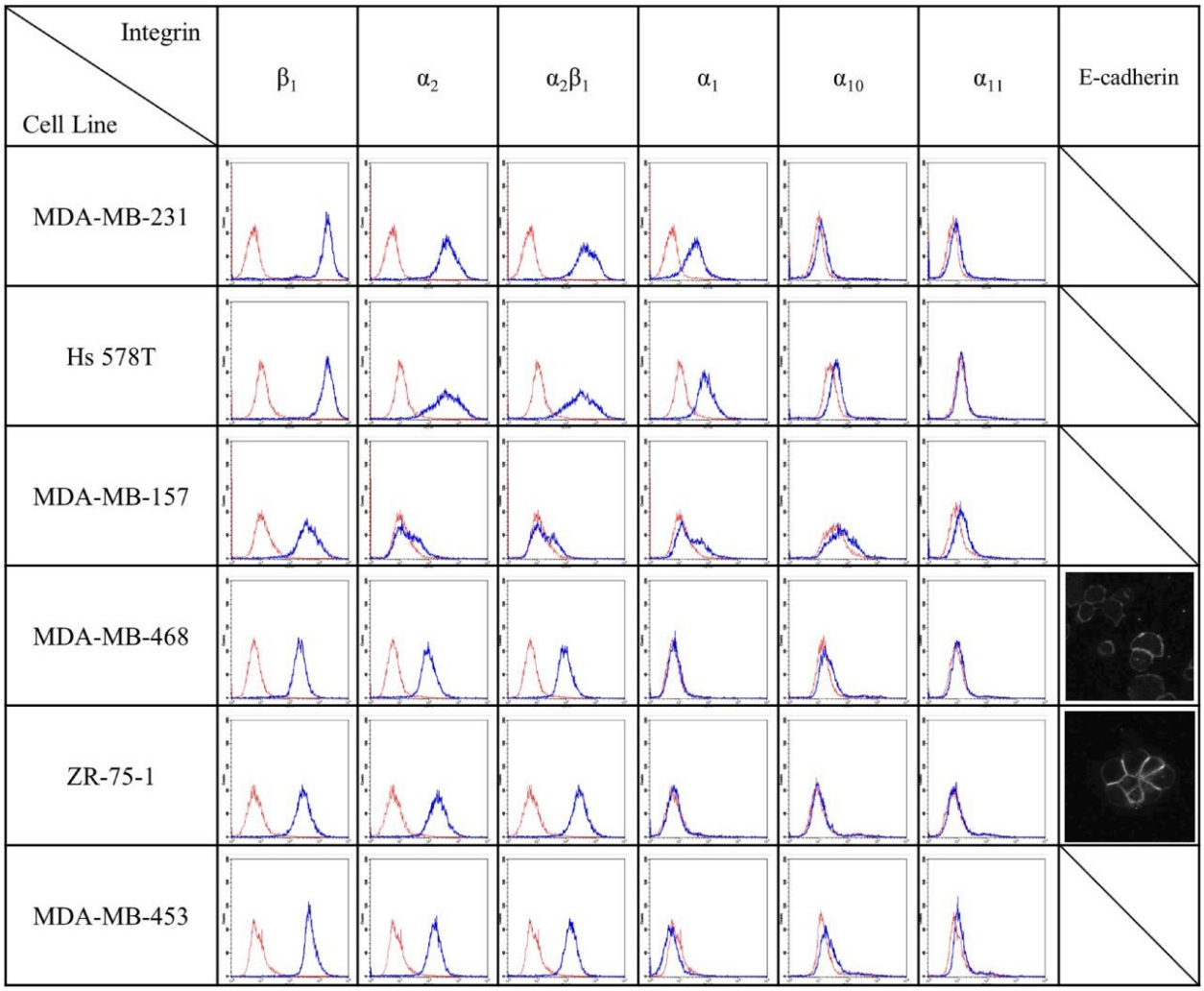

Figure 16 FACS based analysis of integrin receptors relevant to collagen binding. Blue lines show integrin fluorescence intensity and red lines show secondary antibody control fluorescence intensity. Immunocytochemical staining for E-cadherin is shown in the rightmost column for the two cell lines that showed detectable levels in this assay.

While all cell lines investigated (except MDA-MB-157) have suitable integrins for collagen adhesion and traction generation, it is possible that integrin level does not correlate with integrin function. As such, we also measured the ability of cells from each cell line to generate

traction on collagen fibrils through contraction assays. In these assays, dispersed cells were allowed to contract a 1.0 mg/mL collagen gel over four hours. Here, the two stellate cell lines with abundant α2β1 integrins, MDA-MB-231 and Hs 578T, contracted the gels to less than 30% of their initial size within four hours (Figure 17). Of the cells demonstrating grape-like or mass aggregate morphology, MDA-MB-468 and ZR-75-1 cells were moderately efficient at contraction, resulting in gels approximately half their initial size after four hours, while MDA-MB-453 cells were poor contractors. Interestingly, MDA-MB-157 cells showed some contractile ability both in the contraction assay (Figure 17) and in the alignment of collagen around the spheroid (Figure 15B) despite their low levels of relevant integrins. Overall, the contraction assays show some correlation with aggregate morphology, as the two stellate lines with relevant integrins contracted the gel very efficiently while other cell lines with comparable integrin levels either contracted moderately or very inefficiently (MDA-MB-453).

We also found some correlation between collagen contraction and collagen invasion as measured in the spheroid assay (Figure 17). The three invasive cell lines were at least moderately contractile in the contraction assay. However, the ZR-75-1 cells were relatively efficient contractors but did not invade in the spheroid assay at all.

Taken together, the results of the spheroid invasion and collagen contraction assays suggest that collagen contractile ability is necessary but insufficient to allow for cell invasion in a collagen I environment. With neither integrin profiles nor contractile ability clearly distinguishing invasive from noninvasive cells, we investigated levels of cadherins in these cell lines. The existence of strong cell-cell contacts could, for example, explain why tractional force generation on collagen fibrils is necessary but insufficient for invasion from spheroid culture into a surrounding collagen

I matrix. Altered balance of cell-cell and cell-environmental affinity is a key aspect of the epithelial to mesenchymal transition (EMT) that plays a critical role in tumor progression and has been invoked previously to explain varied invasive capacity both experimentally and in simulations.[18,156,157] Previous studies showed high levels of E-cadherin in ZR-75-1 cells, moderate levels in MDA-MB-468 cells, and no detectable E-cadherin in MDA-MB-231, Hs 578T, or MDA-MB-453 cells.[82] Via immunocytochemistry, we confirmed these findings and further found no notable staining in the MDA-MB-157 cells (Figure 16). The high level of E-cadherin expressed by the ZR-75-1 cells may explain why these cells, with appropriate integrins and strong contractile ability, fail to invade in spheroid assay. N-cadherin, which has been shown to contribute to invasive capacity in breast cancer cells, was detectable by immunocytochemical staining only in the Hs 578T cells (data not shown), consistent with a previous report.[158]

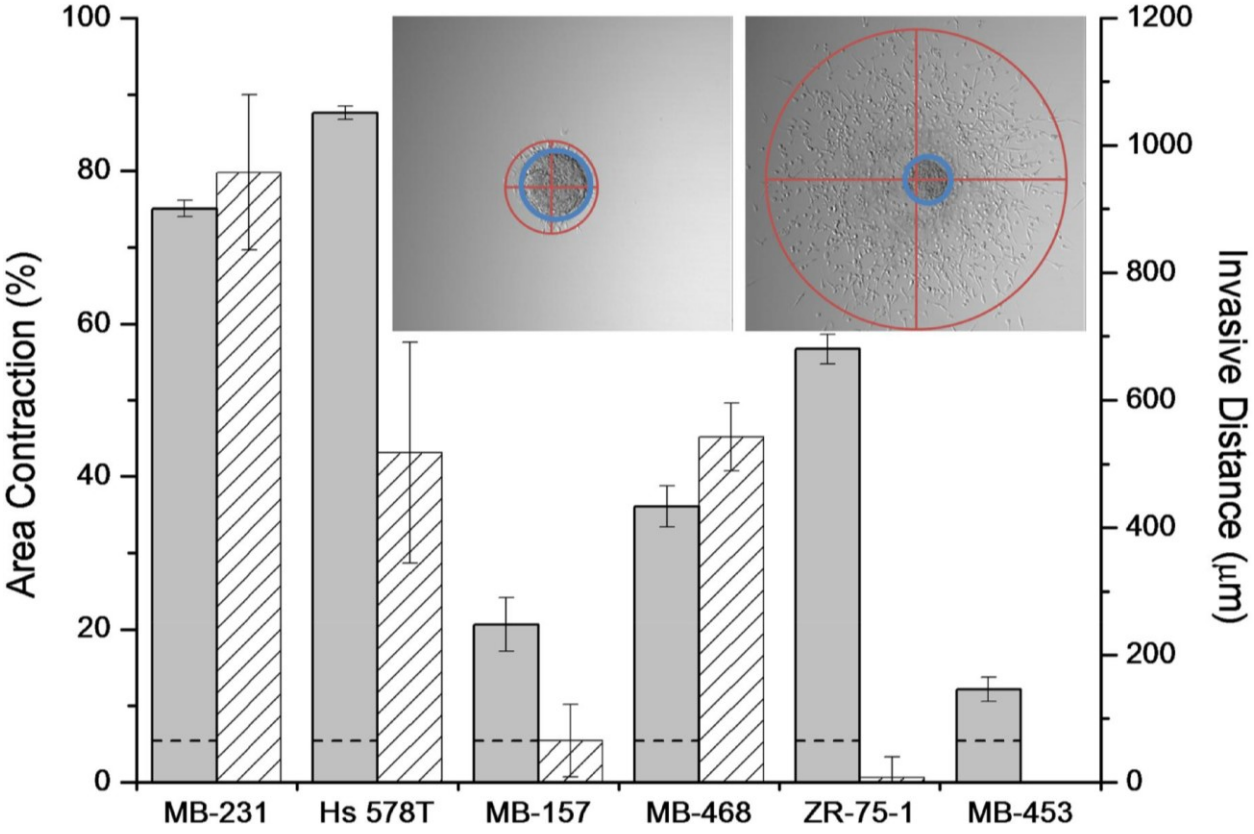

Figure 17 Percent area contraction of collagen I gels with dispersed cells (gray) and invasive distance from spheroids (pattern) for each cell line. Data are average values with error bars indicating standard deviation from three to seven independent experiments each in biological triplicate (for contraction) and 11-18 spheroids in biological replicate (for invasion). Dotted line indicates contraction of collagen I gels without cells. Inset shows extent of invasion (red) and spheroid core (blue) for a representative MDA-MB-231 spheroid. Invasive distance is defined as the diameter of the blue circle (spheroid core) subtracted from the diameter of the red circle (invasion area) drawn at 24 hours. The spheroid core used in the invasive distance calculation is the larger of the spheroid ore at either 2 or 24 hours. Only the Hs 578T cell line exhibited a larger core at 24 hours than at 2 hours.

4.2.5 Cell invasive capacity in collagen I correlates with gene expression signatures

Given that full correlation was not found between any of the static or dynamic cell signatures considered above and spheroid invasive capacity in collagen I environments, we considered correlation between collagen I invasive capacity and gene expression signatures to potentially capture the wide range of factors involved in invasion both in the *in vitro* collagen I environment and in the *in vivo* ECM surrounding tumors.

In recent years, gene expression profiling has been used to classify breast tumors in a manner that has prognostic significance. Early molecular categorization via unsupervised hierarchical gene clustering of human breast tumors showed clustering into four categories – luminal, basal, ERBB2 (the gene associated with HER2 expression), and normal[29] – while later studies stratified luminal tumors and identified another category known as claudin-low[159,160]. Smaller gene sets have since been used to predict recurrence and tailor treatment for women with early stage breast cancers, with a 70 gene set appropriate for both hormone receptor positive and negative cancers and a 21 gene set appropriate for predicting recurrence in hormone receptor positive tumors.[145,161] Both classifiers include genes involved in proliferation and the EMT as well as genes that are outside categories obviously associated with cancer development and progression.

More recently, gene profiling and unsupervised hierarchical clustering have been performed on commonly used breast cancer cell lines to understand their similarities and differences from primary breast tumors and to identify cell lines that may be useful in addressing particular questions.[37,38] Two studies each examined gene expression in more than 50 breast cancer cell lines. Hierarchical clustering of gene expression profiles of these cell lines revealed somewhat different groupings than did profiling of primary breast tumors. Like tumors, cell lines clustered

broadly into luminal and basal categories, though the particular categories established differed somewhat from the tumor categories and were termed luminal, basal A and basal B. [37,38] These two studies identified each of the stellate cell lines investigated here as members of the basal B class, while MDA-MB-468 was categorized as basal A and the ZR-75-1 and MDA-MB-453 cell lines were categorized as luminal. Kao et al. and Prat et al. also used breast tumor classifications to classify the cell lines, with all stellate cell lines clustered in either of the aggressive tumor classifications of claudin-low or ERBB2, the latter despite the fact that none of these cell lines are HER2 positive.[33,37] The grape-like cell lines were not found to all belong to the same category, with both studies identifying MDA-MB-468 cells as basal and MDA-MB-453 cells as either luminal B or luminal. ZR-75-1 cells were categorized as luminal A and luminal, by Kao et al. and Prat et al., respectively. Kao et al. also assessed the breast cancer cell lines in terms of whether they displayed a positive wound healing signature (512 genes), a positive hypoxia signature (123 genes), or poor prognosis as assessed by the 70 gene assay described above.[37,145,162,163] We note that each of these signatures was performed for cells cultured on 2D and that cells cultured in 3D, and particularly in 3D collagen I, may yield somewhat different results.[82] Five of the six cell lines we studied have also been assessed for percentage of cancer stem cells (CSCs), which may reasonably be expected to correlate with invasive and metastatic capacity.[164] Each of these cell lines was found to have measurable but low levels of CSCs as assessed through aldehyde dehydrogenase expression and activity, with less than 1% found in the most invasive MDA-MB-231 cell line. However, not all CSC markers correlate and, like other gene expression profiles, these markers may depend on the dimensionality of cell culture.[165] Table 3 summarizes results for the cell lines investigated in this study.

Among the cell lines tested here, stellate cell aggregate morphology clustered strongly with gene expression profiles as determined either from cell lines or tumors. Such correlations were not as strong in the other cell lines investigated. Among the functional wound-healing and hypoxic gene signatures that have been previously associated with cancer prognosis, two of the three stellate cell lines demonstrated a positive response while none of the grape-like cell lines did. Given the importance of collagen I integrins in wound healing, it is perhaps unsurprising that the two cell lines found to be very efficient contractors of collagen I show positive wound healing signature. Intriguingly, the poor prognosis prediction from the 70 gene assay does not correlate with aggregate morphology nor with the categorizations assigned by unsupervised clustering. However, it does predict poor prognosis in two of the three cell lines found to be invasive in this study, including the MDA-MB-468 cell line that would not be predicted to be aggressive from aggregate morphology, integrin profile, or contractile capacity. This finding suggests the collagen invasion assay, or a related one based on primary tumors or organoids, as an inexpensive functional assay to identify tumors with collagen invasive capacity and poor prognosis.

Cell line	Aggregate Morphology #	Cancer stem cell §	Cell line subtype *	Tumor subtype **	Tumor subtype ***	Gene Signatures for Wound, Hypoxia, 70 Gene +	Collagen contractile capacity #	Collagen relevant integrins#	Collagen invasion capacity#
MDA-MB-231	stellate	0–1%	BB	ERBB2	CLL	+ + +	+	+	+
Hs 578T	stellate	0–1%	BB	ERBB2	CLL	+ + -	+	+	+
MDA-MB-157	stellate	1–5%	BB	ERBB2	CLL	- - -			
MDA-MB-468	grape-like	N/A	BA	B	B	- - +	+	+	+
ZR-75-1	mass	1–5%	L	LA	L	- - -	+	+	
MDA-MB-453	grape-like	1–5%	L	LB	L	- - -		+	

Table 3 Cell line aggregate morphological classes, cancer stem cell (CSC) percentages, subtypes, positivity for wound, hypoxia, and 70 gene signature, and collagen related activities.

§CSC percentages obtained from Reference [164]. MDA-MB-468 cells were not included in this study and thus labeled N/A (not available).

*Subtypes of breast cancer cell lines identified by unsupervised hierarchical clustering: BB = basal B, BA = basal A, L = luminal.[37,38]

**Subtypes of breast cancer cell lines using tumor classifications described in Reference [159] as reported in Reference [37]: ERBB2 = ERBB2 signature; B = basal, LA = luminal A, LB = luminal B.

***Subtypes of breast cancer cell lines using tumor cell classifications as reported in Reference [33]: CLL = claudin-low; B = basal; L = luminal.

4.3 Conclusion

We found that aggregate morphology of six breast cancer cell lines within 3D collagen I gels was very similar to that in BME, though we categorized ZR-75-1 as exhibiting mass aggregates rather than grape-like aggregates. Unlike in previous studies, we found that in some circumstances cell aggregate morphology in 3D physiologically relevant environments could be predicted from cell morphology in simple contexts. Indeed, aggregate cell morphology on 2D in all cases investigated was very similar to that seen in 3D collagen I and 3D BME. Additionally, cell morphology in isolation either in 3D collagen I or on 2D glass was sufficient to establish which cells would adopt a stellate aggregate morphology. Despite the ability to predict 3D aggregate morphology from morphology in simpler contexts, aggregate morphology was not found to fully correlate with cell migratory behavior, collagen contractile behavior, balance of integrin and cadherin expression, or invasion from a spheroid into a collagen I gel. Three of the six cell lines investigated here – MDA-MB-231, Hs 578T, and MDA-MB-468 – were found to be invasive in collagen I gels. Two of these cell lines were from the stellate aggregate morphology class and one was from the grape-like aggregate morphology class. The invasive cell lines were not found to be distinguishable from noninvasive cell lines through consideration of aggregate morphology, integrin and cadherin expression, or collagen contractility capacity, though collagen contractility appears to be necessary but insufficient to predict collagen I invasive capacity. For the set of cell lines studied, all cell lines that demonstrated stellate aggregate morphology and had suitable integrins for collagen I attachment were invasive. For cell lines that demonstrated other aggregate morphologies, no clear predictor was found. However, it is intriguing that two of the three invasive cell lines, including the MDA-MB-468 cells from the grape-like morphological

aggregate class, were associated with poor prognosis signature in a validated 70 gene assay. This suggests that the spheroid invasion assay in collagen I recapitulates key aspects of the *in vivo* tumor environment beyond cell-cell and cell-environmental contacts. This finding also implies that spheroid invasion or related assays can serve as functional assays to identify breast cancers with invasive capacity and poor prognosis, including those that do not have morphological markers of aggressiveness.

5 Spatial separation and transmittal of invasive capacity in co-culture spheroids

5.1 Introduction

Spatial separation of tissues is a well-studied phenomenon in embryonic development,[166–169] but its role in tumor growth and metastasis remains poorly understood.[170,171] Given that tumors are comprised of heterogeneous cell types[172–175] with a range of invasive capacities, studying the compartmentalization of mixed cancer cell populations can aid in understanding how tumor boundaries are defined and disrupted during metastasis. The aims of the following work are to identify motivating factors for cell-type segregation of breast cancer cell lines in the absence and presence of basement membrane extract (BME) and to evaluate induced invasive modes of noninvasive cells in the presence of invasive cells.

The differential adhesion hypothesis of developmental biology suggests that tissue segregation can be modeled as immiscible Newtonian fluids driven by adhesive forces and tissue surface tension, predicting that tissues with higher adhesive forces and higher surface tension will be enveloped by other tissues to minimize total free energy in the system.[176–178] However, this model appears not to hold when applied to cells that have undergone epithelial to mesenchymal transition (EMT), suggesting the complicated biology of tumor dynamics cannot be adequately modeled by Newtonian fluids.[170] The cellular Potts model is a lattice-based computational model that predicts cell behavior. It was originally based on the differential adhesion hypothesis to model cell sorting,[179] but it has since been adapted to model various other biological events in embryo

development and tumor growth[180–182]. The role of extracellular matrix (ECM) has thus far been under-considered in Potts models, with few exceptions.[157,179,183,184]

To recapitulate an aspect of the heterogeneous subpopulations of cancer cells within a solid tumor, spheroids were prepared from a mixture of cell lines that were independently tagged with fluorescent dyes. Co-culture spheroid formation and invasion were monitored to determine to what extent cancer cell subpopulations organize within a tumor. MDA-MB-231 cells and MDA-MB-468 cells were "invasive subpopulations" previously shown to substantially invade in 3D collagen I gels mixed with either the other invasive cell line or a "noninvasive subpopulation" that did not invade from a spheroid on its own in previous experiments. This includes MDA-MB-157, a breast cancer cell line that forms a putatively aggressive stellate morphology with low collagen-binding integrin levels; MCF10A, a non-cancerous breast cell line; and ZR-75-1, a mass-like breast cancer cell line with comparable amounts of α2β1 collagen-binding integrin as the MDA-MB-468 invasive cell line (Figure 16). In total, seven combinations of cell lines were tested: MDA-MB-231 with MDA-MB-468, MDA-MB-231 with MDA-MB-157, MDA-MB-468 with MDA-MB-157, MDA-MB-231 with MCF10A, MDA-MB-468 with MCF10A, MDA-MB-231 with ZR-75-1, and MDA-MB-468 with ZR-75-1.

Whereas certain cell lines may display poor invasive capacity due to weak sensing or remodeling of the extracellular environment on their own, the presence of a leading invasive line may impart invasive capacity by generating pathways within the ECM or transmitting oncogenic signals to less invasive cells via cell-cell communication.[171,185,186] In one experimental study of MCF10A non-cancerous breast epithelial cells with MDA-MB-231 invasive breast cancer cells, MCF10A cells collectively invaded behind leader MDA-MB-231 cells, even though they showed

no invasive capacity on their own.[171] When MMP activity and ROCK-based cell contractility was inhibited in the more invasive MDA-MB-231 cell line, matrix reorganization was blocked and leader-follower behavior between the two cell lines was no longer observed. This suggests ECM remodeling must be considered to understand how invasive behavior may be passed between heterogeneous cell populations.

Three experimental conditions of increasing complexity were utilized for co-culture spheroid studies: spheroid formation without BME, spheroid formation with BME, and invasion of spheroids with BME into collagen I gels. Forming spheroids without BME allowed us to observe cell segregation in the absence of ECM signaling. In cases where BME was supplemented for spheroid formation, changes in cell segregation can be directly attributed to signaling from the additional ECM components. BME also aids in spheroid compaction, resulting in spheroids that can be isolated and implanted into collagen I gels for invasion studies. Without BME, some cell lines and, by extension, co-culture combinations of cell lines were unable to compact tightly enough to be implanted for invasion studies. By studying cell segregation in the absence and presence of ECM components, the importance of particular integrins for laminins (in BME) or collagen I could be evaluated.

Considering that the strength of cell-cell adhesions is a distinguishing factor between pre-cancerous epithelial cells and post-EMT invasive cells and that cell-cell adhesion correlates with tissue surface tension, less invasive cell lines are predicted to gather at the spheroid center and more invasive lines expected to surround them during co-culture spheroid formation. The noninvasive MCF10A cell line is predicted to segregate at the center of spheroids during formation and potentially migrate collectively behind more invasive leader cells regardless of co-culture

partner (MDA-MB-231 or MDA-MB-468), in part due to strong cell-cell adhesions characteristic of epithelial cells that have not undergone EMT and in agreement with previous studies.[170,171] The weakly invasive MDA-MB-157 breast cancer cell line is also predicted to segregate at the center of spheroids and follow invasive cells out. By following tracks made by other cells, the MDA-MB-157 cells may be able to invade without relying on low collagen I-binding integrin levels. ZR-75-1 cells, which show poor invasive capacity in collagen I but adequate levels of collagen I-binding integrins, may not invade regardless of tracks made by other cells. MDA-MB-231 cells and MDA-MB-468 cells display different invasive morphologies but both can degrade ECM using MMPs, reorganize collagen fibers, and generate traction during invasion.[187] They both have the potential to imbue noninvasive cells with invasive capacity via ECM remodeling or cell-cell communication. MDA-MB-468 cells in particular secrete numerous extracellular vesicles, which may serve in communication with distant cells.[188] Between strongly invasive MDA-MB-231 cells and moderately invasive MDA-MB-468 cells, the MDA-MB-468 cells may reach greater distances by following MDA-MB-231 invasion tracks. These experiments will also evaluate whether invasive morphology is at all affected by the primary invader – if follower cells establish a different morphology with MDA-MB-231 cells than with MDA-MB-468 cells, this may suggest a chemical as well as mechanical mode of communication.

5.2 Results

Live cell dyes Vybrant DiD and CellTracker CMTPX were used to distinguish two cell lines prepared in the same spheroid. Each dye was tested on spheroids of single cell lines to assess whether the presence of the dye affected cell behavior (Figure 18). On their own, the use of DiD

or CMTPX did result in a small to moderate decrease in invasive distance when compared to unlabeled cells, with CMTPX showing a slightly stronger effect. For this reason, the experiments involving pairs of cell lines were repeated with dye combinations reversed so that potential dye effects could be assessed and corrected for. In no case did dye reversal change qualitative observations. Additional control experiments were performed: spheroids were prepared with a combination of unlabeled cells and cells of the same line labeled with either DiD or CMTPX to assess whether cells with dyes segregate during spheroid formation. Preliminary results indicate that the use of live cell dyes does not affect cell distribution in a spheroid of a single cell type (data not shown). Other ways of distinguishing cell populations such as non-membrane dyes or GFP-transfected cells are also under consideration.

Spatial separation of subpopulations was monitored for the first 10 hours of spheroid formation for both BME-free and BME-supplemented spheroids. BME-free spheroids appeared as a flat sheet along the bottom of the round-bottom well for the extent of the experiments, whereas BME-supplemented spheroids were already tighter and more round in overall shape in initial images. Interestingly, there was a consistent difference in spatial separation between BME-free and BME-supplemented spheroids for most cell line combinations. Generally, combinations including MDA-MB-231 showed the MDA-MB-231 cell line preferentially collecting towards the outer boundary of spheroids without BME, with a shift towards even mixing for spheroids with BME. In contrast, combinations including MDA-MB-468 showed even mixing between cell lines in the absence of BME and a preference for MDA-MB-468 cells towards the outside of the spheroid when supplemented with BME and mixed with either MDA-MB-231, MDA-MB-157, or ZR-75-1 but not when mixed with MCF10A, which preferentially collected on the outside instead.

Results were consistent for each pair of cell lines when dyes were reversed. Representative images of MDA-MB-231 with MDA-MB-468 and MDA-MB-231 with ZR-75-1 co-culture spheroid formation samples at 10 hours are shown in Figure 19. Quantitative analysis of spheroid segregation and invasion is currently underway (Appendix 3), with representative histograms shown next to sample images in Figure 19. All formation results are summarized in Table 4.

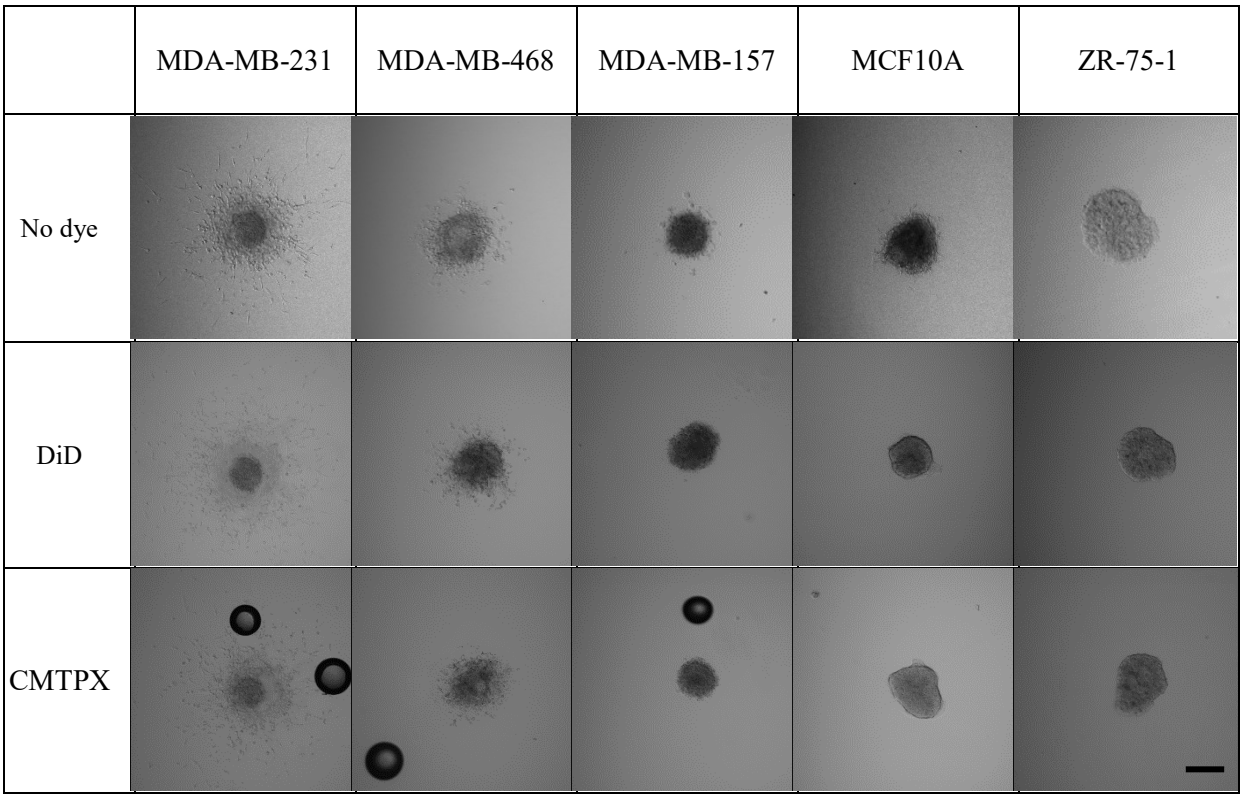

Figure 18 Invasion of representative single cell line spheroids at 24 hours without and with DiD or CMTPX live cell dyes. Scale bar = 200 µm. Bubbles near spheroids can be seen in images of MDA-MB-231, MDA-MB-468, and MDA-MB-157 cells with CMTPX.

	No BME		With BME	
MDA-MB-231 DiD (red) + MDA-MB-468 CMTPX (green)	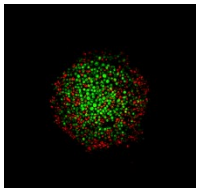	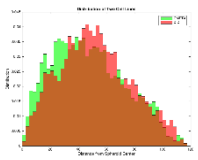	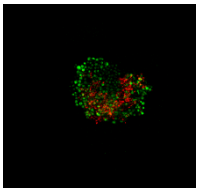	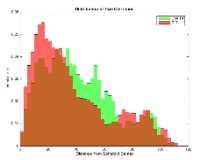
MDA-MB-231 CMTPX (green) + MDA-MB-468 DiD (red)	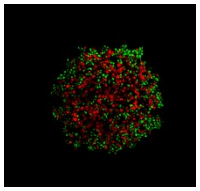	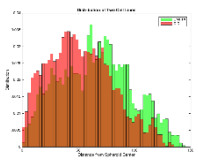	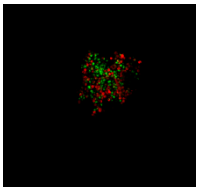	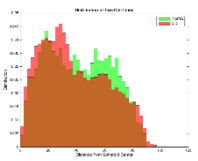
MDA-MB-231 DiD (red) + ZR-75-1 CMTPX (green)	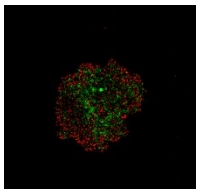	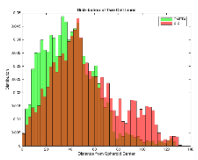	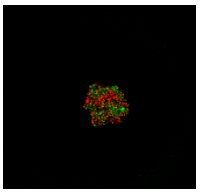	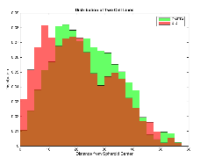
MDA-MB-231 CMTPX (green) + ZR-75-1 DiD (red)	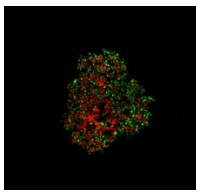	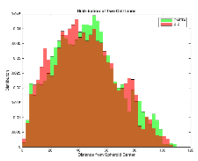	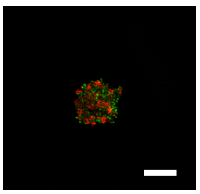	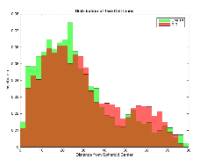

Figure 19 Representative images of co-culture spheroid formation at 10 hours. Scale bar = 200 µm. DiD and CMTPX are artificially colored red and green, respectively. Preliminary quantification of cell line segregation is shown to the right of each image as histograms of distribution vs. distance from center of mass in pixels. MDA-MB-231 and MDA-MB-468 spheroids show MDA-MB-468 cells on the outside in the presence of BME and MDA-MB-231 cells on the outside in the absence of BME. MDA-MB-231 and ZR-75-1 spheroids show a random mixing of cells in the presence of BME and MDA-MB-231 cells in the absence of BME.

Cell line combination	Spheroid composition: cell line with preference for outside	
	No BME	With BME
MDA-MB-231 + MDA-MB-468	MDA-MB-231	MDA-MB-468
MDA-MB-231 + MDA-MB-157	MDA-MB-231	MDA-MB-231
MDA-MB-468 + MDA-MB-157	mix	MDA-MB-468
MDA-MB-231 + MCF10A	MDA-MB-231	mix
MDA-MB-468 + MCF10A	mix or MDA-MB-468	MCF10A
MDA-MB-231 + ZR-75-1	MDA-MB-231	mix
MDA-MB-468 + ZR-75-1	mix	MDA-MB-468

Table 4 Summary of co-culture spheroid formation at 10 hour time point. Results grouped according to cell line combinations regardless of dye order. For most cell line combinations, a difference in separation can be noted between BME and BME-free conditions.

Co-culture spheroids prepared with BME as described in section 2.7.1 were implanted in collagen I gels and imaged daily. Initial images were taken within two hours of implantation and showed general agreement of spatial separation with what was found in formation experiments at 10 hours (Table 4), except for the combination of MDA-MB-231 cells and MDA-MB-468 cells, which showed MDA-MB-231 cells towards the outside of the spheroid. This may be due to the greater invasive capacity and speed of MDA-MB-231 cells compared to MDA-MB-468 cells such that even at two hours following implantation, the MDA-MB-231 cells had already invaded farther

into the collagen gel than the MDA-MB-468 cells. The greatest invasive distance of each pair of cell lines as a whole was reduced by about half when the more invasive cell line (MDA-MB-231 or MDA-MB-468) was dyed with CMTPX, which was not unexpected given the results shown in Figure 18. Generally, MDA-MB-468 invasion from co-culture spheroids was consistent with that of invasion from single cell line MDA-MB-468 spheroids dyed with DiD or CMTPX (Figure 18), however, because invasive distance was so small, it was difficult to interpret results in some samples.

Invasion results from co-culture spheroids segregated into four classes based on the behavior of the less invasive cell line: invasive (MDA-MB-468), collective (MCF10A with MDA-MB-231), individual (MDA-MB-157), and noninvasive (ZR-75-1; MCF10A with MDA-MB-468). Samples were evaluated based on the morphology of the cells that invaded and whether the less invasive line invaded at all, individually, or collectively. Representative images from each class are shown in Figure 20.

For the single case in which two invasive cell lines (MDA-MB-231 and MDA-MB-468) were combined, both cell lines invaded, with MDA-MB-468 cells reaching maximal distances of at least half but no more than what was seen from MDA-MB-231 cells. This is approximately consistent with the single spheroid studies in Figure 18, with some MDA-MB-468 cells reaching greater distances than expected. MDA-MB-231 cells initially invaded with stellate morphology, but started to look more round after two days. This was only observed at such an early time point in the case of MDA-MB-231 cells in the presence of MDA-MB-468 cells.

MCF10A cells showed some collective invasion behind leader MDA-MB-231 cells, consistent with previous studies.[171] In these cases, MDA-MB-231 cells invaded significantly with

stellate morphology over the first 24 hours. MCF10A cells appeared to stream behind them, maintaining a cobblestone morphology. After 2-3 days, most cells looked round.

MDA-MB-157 cells, which show minimal invasive capacity on their own, appeared to invade individually in the presence of MDA-MB-231 or MDA-MB-468. Although relatively few MDA-MB-157 cells invaded from each spheroid, they reached distances as far as MDA-MB-231 or MDA-MB-468 leader cells. MDA-MB-231 cells initially invaded with stellate morphology, but MDA-MB-157 cells appeared round when they invaded.

In several cases, the less invasive cell line showed no significant invasion (ZR-75-1 with MDA-MB-231 or MDA-MB-468; MCF10A with MDA-MB-468). In the case of MDA-MB-231 with ZR-75-1 cells, as MDA-MB-231 cells broke away from the spheroid core, the ZR-75-1 cells that were left behind seemed to loosen, but did not break away to show individual or collective invasion. Nonetheless, extracellular vesicles from ZR-75-1 cells could be recognized at moderate distances from the spheroid core within the collagen gels.

Class	Invasive	Collective	Individual	Noninvasive
Example cell lines in co-culture	MDA-MB-231 + MDA-MB-468	MDA-MB-231 + MCF10A	MDA-MB-231 + MDA-MB-157	MDA-MB-231 + ZR-75-1
Invasion at 24 hours (transmittance)	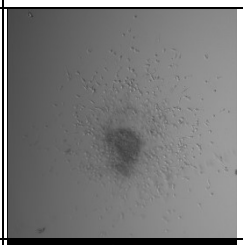	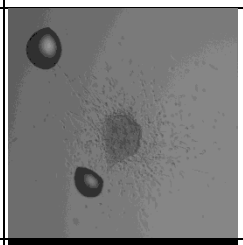	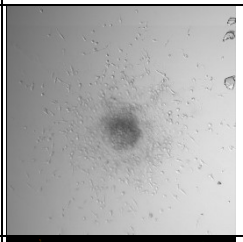	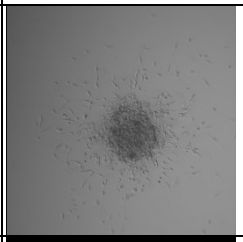
Invasion at 24 hours (MDA-MB-231 in red)	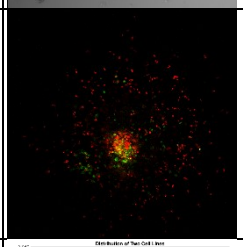	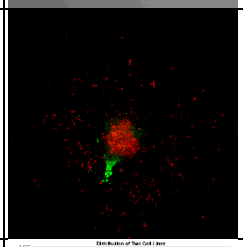	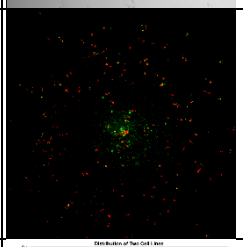	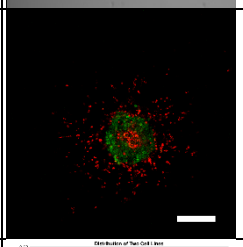
Histogram	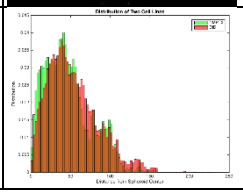	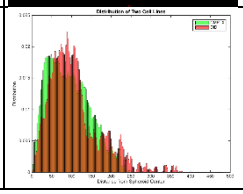	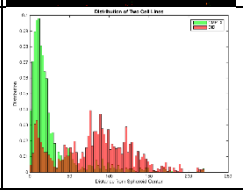	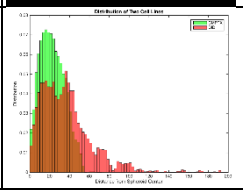

Figure 20 Invasive classes of less invasive cell lines from co-culture spheroids. Representative co-culture spheroids are shown in transmittance and fluorescence channels for each class of co-culture invasion at 24 hours. Scale bar = 200 µm. MDA-MB-231 cells are artificially colored red and cells from the less invasive line are artificially colored green. Preliminary quantification of cell line invasion is shown below each image as histograms of distribution vs. distance from center of mass in pixels.

5.3 Discussion

Experiments of increasing complexity were conducted to evaluate the effects of BME and collagen I-signaling on co-culture segregation and invasion. The simplest evaluation began with monitoring the segregation of two cell lines in co-culture spheroids in the absence of ECM. In this case, only cell-cell contacts were present to influence segregation dynamics. This was followed by co-culture spheroid formation with additional BME. This was not only a consistent method for forming spheroids that could subsequently be implanted into collagen I gels, but also provided an intermediate condition in which cells with suitable integrins for laminin could be stimulated. Finally, co-culture spheroid invasion in collagen I gels was evaluated. In this condition, we could evaluate whether rearrangement of the ECM by an invasive cell line was sufficient to induce invasive capacity in a less invasive cell line.

In the case of BME-free spheroid formation, preference for the outside of the spheroid followed the trend of MDA-MB-231 > MDA-MB-468 > ZR-75-1/MDA-MB-157/MCF10A. Absent signals from ECM components, segregation depended on differences in cell-cell preferences between cell lines. Interestingly, when spheroids were supplemented with BME, MDA-MB-231 and MDA-MB-468 reversed preference for the outside of the spheroid. This may be due to differences in integrin levels for BME components like laminin, such that the line with the higher laminin-binding integrin levels arrange toward the outside of the spheroid where a BME shell forms. Some evidence that MDA-MB-468 cells have high levels of α6 integrin subunit supports this,[189] though further investigation into levels of laminin-specific integrins (α3β1, α6β1, α6β4, and α7β1) in each of these cell lines will be necessary to fully test the theory.

A related trend in spheroid segregation was observed: MDA-MB-231 cells generally segregated to the outside of the spheroid when mixed with less invasive cell lines in the absence of BME but mixed more evenly in the presence of BME. Inversely, MDA-MB-468 cells generally mixed evenly with less invasive lines in the absence of BME but segregated to the outside of the spheroid in the presence of BME. A combination of differences in cell-cell adhesion and laminin-adhesion between cell lines could explain this phenomena. This suggests that less invasive cell lines have stronger cell-cell adhesions than MDA-MB-231, thus segregating to the center of the spheroid, but may have relatively equal levels of laminin integrins, resulting in even mixing in the presence of BME. MDA-MB-468 cells show consistent preference for the outside of the spheroid only in the presence of BME, which may be due to a significant differences in laminin integrin levels compared to the other cell lines.

For co-culture invasion studies, collagen I binding β1 integrins additionally became important. MDA-MB-231 and MDA-MB-468 cells with suitable integrins to rearrange and pull on collagen made tracks during invasion. These tracks were available to other cells with low invasive capacity in order to easily migrate away from the spheroid core, although this was not sufficient in every case to induce invasion in less invasive cell lines. Follower-invasive behavior was seen in MCF10A as collective migration, in MDA-MB-157 as individual migration, and not at all in ZR-75-1.

MCF10A and ZR-75-1 cells, which appear mass-like in aggregates, did not demonstrate the same follower behavior but did maintain strong cell-cell contacts characteristic of the mass-like morphology class. As a result, they either followed collectively or not at all. In contrast, MDA-MB-157 cells cannot bind well to collagen but do natively display a stellate “aggressive”

morphology and can individually migrate through tracks once they are made. However, follower MDA-MB-157 cells appeared round in these contexts, indicating the ability for natively stellate cells to invade is not dependent on regaining stellate morphology. The ability of cells to follow invasive tracks does not seem to depend on contractility either, since ZR-75-1 cells can contract collagen gels but cannot follow invasion whereas MDA-MB-157 cells can follow but cannot contract (Figure 17).

Some evidence suggests the existence of chemical communication between cell lines in addition to mechanical communication. MDA-MB-231 cells, which generally invaded into collagen gels with a stellate morphology, were observed as round within 24 hours in the presence of MDA-MB-468. Extracellular vesicles, observed in the presence of MDA-MB-468 and ZR-75-1 cells, may have facilitated chemical communication between cell lines, precipitating the change in MDA-MB-231 morphology. A shift towards round morphology was also observed in single cell line or co-culture spheroids at much later time points (5 days in culture), which may be due in part to an accumulating shift in pH for cell cultures at extended times.

5.4 Conclusion

Co-culture spheroids tend to form with the more invasive cell line on the outside and the less invasive cell line on the inside. One exception is MDA-MB-231 cells with MDA-MB-468 cells, whose balance shifts in the presence of BME signaling resulting in MDA-MB-468 cells toward the outside of the spheroid. Invasive cell lines invade as individual cells and remodel the extracellular environment, forming tracks that may be utilized by less invasive cells. Follower-invasive behavior of less invasive cell lines depend on cell-cell strength and cell motility but not

necessarily suitable integrin levels for binding to ECM. These secondary cell lines can be classified as invasive, individual follower, collective follower, or noninvasive. As can be seen in these experiments, sensing of ECM components by invasive breast cancer cells plays a role in cell-type segregation and invasion dynamics, with invasive cells influencing the invasive behavior of less invasive cells. The results from our heterogeneous co-culture spheroids that less invasive cells could invade along tracks in collagen made by more invasive cells could also have profound implications for treating real tumors, in that it may be best to treat a tumor like its most aggressive cells, and by preventing those cells from invading, this may prevent all invasion.

6 Final Conclusions and Prospective

Breast cancer mortality rates remain high despite clinical improvements to early diagnosis and new classification systems based on genetic profiling and histopathology. This emphasizes an urgent need to fill gaps in understanding in breast cancer research. In this thesis, we assert the value of physiologically relevant *in vitro* studies presented here and planned for the future that provide important complementary modes to understanding critical factors in invasion and metastasis. The role of reciprocal cell-ECM interactions in regulating cell morphology and invasive behavior highlighted in this work cannot be understated.

More studies will be needed to further explore the link between extracellular environment and invasive capacity. Computer simulations could aid in understanding cell morphology setting and invasive behavior. Our group is currently in the process of designing Potts model simulations that model aggregate morphology and interactions of mass-like and grape-like cells. Experimental studies using different matrices or similar matrices with different mechanical properties can be utilized to distinguish effects of ECM sensing from mechanical sensing of the environment. More complex co-culture spheroids, for example with cancer associated fibroblasts, can be prepared to capture other aspects of tumor heterogeneity and i*n vitro* studies of primary breast cancer organoid invasion can also be explored to recapitulate tumor heterogeneity and invasion.

References

1. American Cancer Society. Cancer Facts & Figures 2016. *Cancer Facts Fig. 2016* 1–9 (2016).

2. Breastcancer.org. U.S. Breast Cancer Statistics. (2016). Available at: http://www.breastcancer.org/symptoms/understand_bc/statistics. (Accessed: 19th June 2016)

3. Dumitrescu, R G; Cotarla, I. Understanding breast cancer risk - where do we stand in 2005 ? *J. Cell. Mol. Med.* **9,** 208–221 (2005).

4. SL, S., JB, K., TD, T., Friedman, C. & PA, W. Cancer mortality surveillance -- United States, 1990-2000. *MMWR Morb. Mortal. Wkly. Rep.* **53,** 1–108 108p (2004).

5. Bevers, T. B. *et al.* NCCN clinical practice guidelines in oncology: breast cancer screening and diagnosis. *J. Natl. Compr. Canc. Netw.* **7,** 1060–96 (2009).

6. Kittaneh, M. & Montero, A. J. Biomarkers in Cancer Molecular Profiling for Breast Cancer : A Comprehensive Review. *Biomark. Cancer* **5,** 61–70 (2013).

7. National Cancer Institute. *Understanding Breast Changes*. (2014).

8. Going, J. J. & Moffat, D. F. Escaping from Flatland: Clinical and biological aspects of human mammary duct anatomy in three dimensions. *J. Pathol.* **203,** 538–544 (2004).

9. Tiede, B. & Kang, Y. From milk to malignancy: the role of mammary stem cells in development, pregnancy and breast cancer. *Cell Res.* **21,** 245–257 (2011).

10. McLachlan, E., Shao, Q. & Laird, D. W. Connexins and gap junctions in mammary gland development and breast cancer progression. *J. Membr. Biol.* **218,** 107–121 (2007).

11. Javed, A. & Lteif, A. Development of the human breast. *Semin. Plast. Surg.* **27,** 5–12 (2013).

12. Macias, H. & Hinck, L. Mammary gland development. *Wiley Interdiscip. Rev. Dev. Biol.* **1,** 533–557 (2013).

13. Hanahan, D. & Weinberg, R. A. Hallmarks of Cancer: The Next Generation. *Cell* **144,** 646–674 (2011).

14. Tsai, J. H. & Yang, J. Epithelial – mesenchymal plasticity in carcinoma metastasis. *Genes Dev.* **27,** 2192–2206 (2013).

15. Kalluri, R. & Weinberg, R. A. The basics of epithelial-mesenchymal transition. *J. Clin. Invest.* **119,** 1420–1428 (2009).

16. Christofori, G. & Semb, H. The role of the cell-adhesion molecule E-cadherin as a tumour-suppressor gene. *Trends Biochem. Sci.* **24,** 73–76 (1999).

17. Johnson, J. P. Cell adhesion molecules of the immunoglobulin supergene family and their role in malignant transformation and progression to metastatic disease. *Cancer Metastasis Rev.* **10,** 11–22 (1991).

18. Thiery, J. P., Acloque, H., Huang, R. Y. J. & Nieto, M. A. Epithelial-Mesenchymal Transitions in Development and Disease. *Cell* **139,** 871–890 (2009).

19. Coussens, L. M. & Werb, Z. Matrix metal loproteinases and the development of cancer. *Chem. Biol.* **3,** 895–904 (1996).

20. Chambers, A. F. & Matrisian, L. M. Changing views of the role of matrix metalloproteinases in metastasis. *JNCI J. Natl. Cancer Inst.* **89,** 1260–1270 (1997).

21. Varner, J. A. & Cheresh, D. A. Integrins and cancer. *Curr. Opin. Cell Biol.* **8,** 724–730 (1996).

22. Lukashev, M. E. & Werb, Z. ECM signalling: Orchestrating cell behaviour and misbehaviour. *Trends Cell Biol.* **8,** 437–441 (1998).

23. Leonard, G. D. & Swain, S. M. Ductal carcinoma in situ, complexities and challenges. *J. Natl. Cancer Inst.* **96,** 906–920 (2004).

24. Van Zijl, F., Krupitza, G. & Mikulits, W. Initial steps of metastasis: Cell invasion and endothelial transmigration. *Mutat. Res. - Rev. Mutat. Res.* **728,** 23–34 (2011).

25. Xu, W. *et al.* Cell Stiffness Is a Biomarker of the Metastatic Potential of Ovarian Cancer Cells. *PLoS One* **7,** (2012).

26. Cross, S. E., Jin, Y.-S., Rao, J. & Gimzewski, J. K. Nanomechanical analysis of cells from cancer patients. *Nat. Nanotechnol.* **2,** 780–783 (2007).

27. Elston, C. W. & Ellis, I. O. Pathological prognostic factors in breast cancer. I. The value of histological grade in breast cancer: experience from a large study with long-term follow-up. *Histopathology* **19,** 403–410 (1991).

28. American Cancer Society. *Breast Cancer Staging 7th Edition*. *American Joint Committee on Cancer* (2010).

29. Perou, C. M. *et al.* Molecular portraits of human breast tumours. *Nature* **406,** 747–752 (2000).

30. Vuong, D., Simpson, P. T., Green, B., Cummings, M. C. & Lakhani, S. R. Molecular classification of breast cancer. *Virchows Arch.* **465,** 1–14 (2014).

31. Cheang, M. C. U. *et al.* Ki67 index, HER2 status, and prognosis of patients with luminal B breast cancer. *J. Natl. Cancer Inst.* **101,** 736–750 (2009).

32. Bernard, P. S. *et al.* Supervised risk predictor of breast cancer based on intrinsic subtypes. *J. Clin. Oncol.* **27,** 1160–1167 (2009).

33. Prat, A. *et al.* Phenotypic and molecular characterization of the claudin-low intrinsic subtype of breast cancer. *Breast Cancer Res.* **12,** R68 (2010).

34. Masters, J. R. Human cancer cell lines: fact and fantasy. *Nat. Rev. Mol. Cell Biol.* **1,** 233–236 (2000).

35. Wang, C. S. *et al.* Selective culture of epithelial cells from primary breast carcinomas using irradiated 3T3 cells as feeder layer. *Pathol. Res. Pract.* **197,** 175–181 (2001).

36. Holliday, D. L. & Speirs, V. Choosing the right cell line for breast cancer research. *Breast Cancer Res.* **13,** 215 (2011).

37. Kao, J. *et al.* Molecular profiling of breast cancer cell lines defines relevant tumor models and provides a resource for cancer gene discovery. *PLoS One* **4,** (2009).

38. Neve, R. M. *et al.* A collection of breast cancer cell lines for the study of functionally distinct cancer subtypes. *Cancer Cell* **10,** 515–527 (2006).

39. Soule, H. D. *et al.* Isolation and Characterization of a Spontaneously Immortalized Isolation and Characterization of a Spontaneously Immortalized Human Breast. *Cancer* 6075–6086 (1990).

40. Nyga, A., Cheema, U. & Loizidou, M. 3D tumour models: Novel in vitro approaches to cancer studies. *J. Cell Commun. Signal.* **5,** 239–248 (2011).

41. Wang, C. *et al.* Three-dimensional *in vitro* cancer models: a short review. *Biofabrication* **6,** 22001 (2014).

42. Griffith, L. G. & Swartz, M. A. Capturing complex 3D tissue physiology in vitro. *Nat. Rev. Mol. cell Biol.* **7,** 211–24 (2006).

43. Roskelley, C. D., Desprez, P. Y. & Bissell, M. J. Extracellular matrix-dependent tissue-specific gene expression in mammary epithelial cells requires both physical and

biochemical signal transduction. *Proc. Natl. Acad. Sci. U. S. A.* **91,** 12378–82 (1994).

44. Bissell, M. J., Rizki, A. & Mian, I. S. Tissue architecture: The ultimate regulator of breast epithelial function. *Curr. Opin. Cell Biol.* **15,** 753–762 (2003).

45. Debnath, J. & Brugge, J. S. Modelling glandular epithelial cancers in three-dimensional cultures. *Nat. Rev. Cancer* **5,** 675–88 (2005).

46. Paszek, M. J. & Weaver, V. M. The Tension Mounts: Mechanics Meets Morphogenesis and Malignancy. *J. Mammary Gland Biol. Neoplasia* **9,** 325–342 (2004).

47. Wozniak, M. A., Desai, R., Solski, P. A., Der, C. J. & Keely, P. J. ROCK-generated contractility regulates breast epithelial cell differentiation in response to the physical properties of a three-dimensional collagen matrix. *J Cell Biol* **163,** 583–595 (2003).

48. Muschler, J. *et al.* A role for dystroglycan in epithelial polarization: Loss of function in breast tumor cells. *Cancer Res.* **62,** 7102–7109 (2002).

49. Paszek, M. J. *et al.* Tensional homeostasis and the malignant phenotype. *Cancer Cell* **8,** 241–254 (2005).

50. Barcellos-Hoff, M. H., Aggeler, J., Ram, T. G. & Bissell, M. J. Functional differentiation and alveolar morphogenesis of primary mammary cultures on reconstituted basement membrane. *Development* **105,** 223–235 (1989).

51. Wozniak, M. A. & Keely, P. J. Use of three-dimensional collagen gels to study mechanotransduction in T47D breast epithelial cells. *Biol. Proced. Online* **7,** 144–61 (2005).

52. Friedl, P. & Bröcker, E. B. The biology of cell locomotion within three-dimensional extracellular matrix. *Cell. Mol. Life Sci.* **57,** 41–64 (2000).

53. Hegerfeldt, Y., Tusch, M., Bröcker, E.-B. & Friedl, P. Collective Cell Movement in

Primary Melanoma Explants. *Cancer Res.* **62,** 2125–2130 (2002).

54. Huang, S. & Ingber, D. E. Cell tension, matrix mechanics, and cancer development. *Cancer Cell* **8,** 175–176 (2005).

55. Provenzano, P. P. *et al.* Collagen density promotes mammary tumor initiation and progression. *BMC Med* **6,** 11 (2008).

56. Luparello, C. Aspects of Collagen Changes in Breast Cancer. *J. Carcinog. Mutagen.* **S13,** (2013).

57. Pöschl, E. *et al.* Collagen IV is essential for basement membrane stability but dispensable for initiation of its assembly during early development. *Development* **131,** 1619–1628 (2004).

58. Schwartz, M. A. Integrin signaling revisited. *Trends Cell Biol.* **11,** 466–470 (2001).

59. Moura-Neto, V. *et al.* in *Glioma Cell Biology* (eds. Sedo, A. & Mentlein, R.) 293–315 (Springer, 2014). doi:10.1007/978-3-7091-1431-5

60. Jokinen, J. *et al.* Integrin-mediated cell adhesion to type I collagen fibrils. *J. Biol. Chem.* **279,** 31956–31963 (2004).

61. Knight, C. G. *et al.* The collagen-binding A-domains of integrins alpha(1)beta(1) and alpha(2)beta(1) recognize the same specific amino acid sequence, GFOGER, in native (triple-helical) collagens. *J. Biol. Chem.* **275,** 35–40 (2000).

62. Tuckwell, D. & Humphries, M. Integrin–collagen binding. *Semin. Cell Dev. Biol.* **7,** 649–657 (1996).

63. Klein, C. E. Integrin alpha 2 beta 1 is upregulated in fibroblasts and highly aggressive melanoma cells in three-dimensional collagen lattices and mediates the reorganization of collagen I fibrils. *J. Cell Biol.* **115,** 1427–1436 (1991).

64. Sonnenberg, A. Laminin receptors in the integrin family. *Pathol. Biol. (Paris).* **40,** 773–8 (1992).

65. Belkin, A. M. & Stepp, M. A. Integrins as receptors for laminins. *Microsc. Res. Tech.* **51,** 280–301 (2000).

66. Ruoslahti, E. RGD and other recognition sequences for integrins. *Annu. Rev. Cell Dev. Biol.* **12,** 697–715 (1996).

67. Hynes, R. O. Cell adhesion: old and new questions. *Trends Cell Biol.* **9,** M33–M37 (1999).

68. Corning. Cancer Research. (2016). Available at: https://www.corning.com/worldwide/en/products/life-sciences/applications/cell-culture/cancer-research.html. (Accessed: 16th June 2016)

69. Chen, Y. Transwell Cell Migration Assay Using Human Breast Epithelial Cancer Cell. *J. Chem. Inf. Model.* **53,** 160 (1989).

70. Moreira, C. G. a, Regan, J. C., Zaidman-Rémy, A., Jacinto, A. & Prag, S. Cell Migration. *Methods* **769,** 111–136 (2011).

71. Harms, B. D., Bassi, G. M., Horwitz, A. R. & Lauffenburger, D. a. Directional persistence of EGF-induced cell migration is associated with stabilization of lamellipodial protrusions. *Biophys. J.* **88,** 1479–88 (2005).

72. Ware, M. F., Wells, A. & Lauffenburger, D. a. Epidermal growth factor alters fibroblast migration speed and directional persistence reciprocally and in a matrix-dependent manner. *J. Cell Sci.* **111,** 2423–2432 (1998).

73. Kramer, N. *et al.* In vitro cell migration and invasion assays. *Mutat. Res. Mutat. Res.* **752,** 10–24 (2013).

74. Cil, T. *et al.* Mammographic density and the risk of breast cancer recurrence after breast-conserving surgery. *Cancer* **115,** 5780–5787 (2009).

75. Boyd, N. F., Martin, L. J., Yaffe, M. J. & Minkin, S. Mammographic density and breast cancer risk: current understanding and future prospects. *Breast Cancer Res.* **13,** 223 (2011).

76. Chang, J. M. *et al.* Stiffness of tumours measured by shear-wave elastography correlated with subtypes of breast cancer. *Eur. Radiol.* **23,** 2450–2458 (2013).

77. Provenzano, P. P. *et al.* Collagen reorganization at the tumor-stromal interface facilitates local invasion. *BMC Med* **4,** 38 (2006).

78. Conklin, M. W. *et al.* Aligned collagen is a prognostic signature for survival in human breast carcinoma. *Am. J. Pathol.* **178,** 1221–1232 (2011).

79. Cowden Dahl, K. D., Dahl, R., Kruichak, J. N. & Hudson, L. G. The epidermal growth factor receptor responsive miR-125a represses mesenchymal morphology in ovarian cancer cells. *Neoplasia* **11,** 1208–15 (2009).

80. Odenwald, M. A., Prosperi, J. R. & Goss, K. H. APC/β-catenin-rich complexes at membrane protrusions regulate mammary tumor cell migration and mesenchymal morphology. *BMC Cancer* **13,** 12 (2013).

81. Lyons, S. M. *et al.* Changes in cell shape are correlated with metastatic potential in murine and human osteosarcomas. *Biol. Open* **5,** 289–299 (2016).

82. Kenny, P. A. *et al.* The morphologies of breast cancer cell lines in three-dimensional assays correlate with their profiles of gene expression. *Mol. Oncol.* **1,** 84–96 (2007).

83. ThermoFisher Scientific. Lipofectamine® 3000 Reagent. 1–2 (2016). Available at: https://www.thermofisher.com/ca/en/home/brands/product-brand/lipofectamine/lipofectamine-3000.html.

84. Wang, K. *et al.* Establishment of a bioluminescent MDA-MB-231 cell line for human triple-negative breast cancer research. *Oncol. Rep.* **27,** 1981–1989 (2012).

85. Kothapalli, D. *et al.* Cardiovascular Protection by ApoE and ApoE-HDL Linked to Suppression of ECM Gene Expression and Arterial Stiffening. *Cell Rep.* **2,** 1259–1271 (2012).

86. Georges, P. C. *et al.* Increased stiffness of the rat liver precedes matrix deposition: implications for fibrosis. *Am. J. Physiol. Gastrointest. Liver Physiol.* **293,** 1147–1154 (2007).

87. Cox, T. R. & Erler, J. T. Remodeling and homeostasis of the extracellular matrix: implications for fibrotic diseases and cancer. *Dis. Model. Mech.* **4,** 165–78 (2011).

88. Perepelyuk, M. *et al.* Hepatic stellate cells and portal fibroblasts are the major cellular sources of collagens and lysyl oxidases in normal liver and early after injury. *Am. J. Physiol. Gastrointest. Liver Physiol.* **304,** G605-14 (2013).

89. Levental, K. R. *et al.* Matrix Crosslinking Forces Tumor Progression by Enhancing Integrin Signaling. *Cell* **139,** 891–906 (2009).

90. Kumar, S. & Weaver, V. M. Mechanics, malignancy, and metastasis: The force journey of a tumor cell. *Cancer Metastasis Rev.* **28,** 113–127 (2009).

91. Lu, P., Weaver, V. M. & Werb, Z. The extracellular matrix: A dynamic niche in cancer progression. *J. Cell Biol.* **196,** 395–406 (2012).

92. Alowami, S., Troup, S., Al-Haddad, S., Kirkpatrick, I. & Watson, P. H. Mammographic density is related to stroma and stromal proteoglycan expression. *Breast Cancer Res.* **5,** R129-35 (2003).

93. Guo, Y. *et al.* Growth factors and stromal matrix proteins associated with mammographic density. *Cancer Epidemiol Biomarkers Prev* **10,** 243–248 (2001).

94. Deak, S. B. *et al.* Desmoplasia in benign and malignant breast disease is characterized by alterations in level of mRNAs coding for types I and III procollagen. *Matrix* **11,** 252–258 (1991).

95. Pathol, J., Stenback, F., Risteli, J., Jukkola, a & Risteli, L. Aberrant type I and type III collagen gene expression in human breast cancer in vivo. *J. Pathol.* **268,** 262–268 (1998).

96. Bergamaschi, A. *et al.* Extracellular matrix signature identifies breast cancer subgroups with different clinical outcome. *J. Pathol.* **214,** 357–367 (2008).

97. Krouskop, T. a, Wheeler, T. M., Kallel, F., Garra, B. S. & Hall, T. Elastic Moduli of Breast and Prostate Tissue under Compression. *Ultrason. Imaging* **20,** 260–274 (1998).

98. Lo, C. M., Wang, H. B., Dembo, M. & Wang, Y. L. Cell movement is guided by the rigidity of the substrate. *Biophys. J.* **79,** 144–152 (2000).

99. Engler, A. J., Sen, S., Sweeney, H. L. & Discher, D. E. Matrix Elasticity Directs Stem Cell Lineage Specification. *Cell* **126,** 677–689 (2006).

100. Zaman, M. H. *et al.* Migration of tumor cells in 3D matrices is governed by matrix stiffness along with cell-matrix adhesion and proteolysis. *Proc. Natl. Acad. Sci. U. S. A.* **103,** 10889–94 (2006).

101. Ulrich, T. A., Lee, T. G., Shon, H. K., Moon, D. W. & Kumar, S. Microscale mechanisms of agarose-induced disruption of collagen remodeling. *Biomaterials* **32,** 5633–5642 (2011).

102. Pathak, a. & Kumar, S. Independent regulation of tumor cell migration by matrix stiffness and confinement. *Proc. Natl. Acad. Sci.* **109,** 10334–10339 (2012).

103. Ehrbar, M. *et al.* Elucidating the role of matrix stiffness in 3D cell migration and remodeling. *Biophys. J.* **100,** 284–293 (2011).

104. Beck, J. N., Singh, A., Rothenberg, A. R., Elisseeff, J. H. & Ewald, A. J. The independent roles of mechanical, structural and adhesion characteristics of 3D hydrogels on the regulation of cancer invasion and dissemination. *Biomaterials* **34,** 9486–9495 (2013).

105. Raub, C. B. *et al.* Noninvasive assessment of collagen gel microstructure and mechanics using multiphoton microscopy. *Biophys. J.* **92,** 2212–2222 (2007).

106. Yang, Y. L., Leone, L. M. & Kaufman, L. J. Elastic moduli of collagen gels can be predicted from two-dimensional confocal microscopy. *Biophys. J.* **97,** 2051–2060 (2009).

107. Abrams, G. A., Goodman, S. L., Nealey, P. F., Franco, M. & Murphy, C. J. Nanoscale topography of the basement membrane underlying the corneal epithelium of the rhesus macaque. *Cell Tissue Res.* **299,** 39–46 (2000).

108. Fu, Y., Chin, L. K., Bourouina, T., Liu, A. Q. & VanDongen, A. M. J. Nuclear deformation during breast cancer cell transmigration. *Lab Chip* **12,** 3774 (2012).

109. Straight, A. F. *et al.* Dissecting temporal and spatial control of cytokinesis with a myosin II Inhibitor. *Science* **299,** 1743–7 (2003).

110. Kovacs, M., Toth, J., Hetenyi, C., Malnasi-Csizmadia, A. & Sellers, J. R. Mechanism of Blebbistatin Inhibition of Myosin II. *J. Biol. Chem.* **279,** 35557–35563 (2004).

111. Yurchenco, P. D. & Ruben, G. C. Basement-Membrane Structure Insitu - Evidence for Lateral Associations in the Type-Iv Collagen Network. *J. Cell Biol.* **105,** 2559–2568 (1987).

112. Kalluri, R. Basement membranes: structure, assembly and role in tumour angiogenesis. *Nat. Rev. Cancer* **3,** 422–433 (2003).

113. Kaufman, L. J. *et al.* Glioma Expansion in Collagen I Matrices: Analyzing Collagen Concentration-Dependent Growth and Motility Patterns. *Biophys. J.* **89,** 635–650 (2005).

114. Yang, Y. L., Motte, S. & Kaufman, L. J. Pore size variable type I collagen gels and their interaction with glioma cells. *Biomaterials* **31,** 5678–5688 (2010).

115. Wolf, K. *et al.* Physical limits of cell migration: Control by ECM space and nuclear deformation and tuning by proteolysis and traction force. *J. Cell Biol.* **201,** 1069–1084 (2013).

116. Murray, G. I., Duncan, M. E., O'Neil, P., Melvin, W. T. & Fothergill, J. E. Matrix metalloproteinase-1 is associated with poor prognosis in colorectal cancer. *Nat. Med.* **2,** 461–462 (1996).

117. Nakopoulou, L. *et al.* Matrix metalloproteinase-1 and -3 in breast cancer: correlation with progesterone receptors and other clinicopathologic features. *Hum. Pathol.* **30,** 436–442 (1999).

118. McGowan, P. M. & Duffy, M. J. Matrix metalloproteinase expression and outcome in patients with breast cancer: analysis of a published database. *Ann. Oncol.* **19,** 1566–72 (2008).

119. Butler, G. S. & Overall, C. M. Updated biological roles for matrix metalloproteinases and new 'intracellular' substrates revealed by degradomics. *Biochemistry* **48,** 10830–10845 (2009).

120. Nguyen-Ngoc, K. V *et al.* ECM microenvironment regulates collective migration and local dissemination in normal and malignant mammary epithelium. *Proc Natl Acad Sci U S A* **109,** E2595-604 (2012).

121. Mierke, C. T., Frey, B., Fellner, M., Herrmann, M. & Fabry, B. Integrin α5β1 facilitates cancer cell invasion through enhanced contractile forces. *J. Cell Sci.* **124,** 369–383 (2011).

122. Plow, E. F., Haas, T. A., Zhang, L., Loftus, J. & Smith, J. W. Ligand binding to integrins. *J. Biol. Chem.* **275,** 21785–21788 (2000).

123. Nishiuchi, R. *et al.* Ligand-binding specificities of laminin-binding integrins: A comprehensive survey of laminin–integrin interactions using recombinant α3β1, α6β1,

α7β1 and α6β4 integrins. *Matrix Biol.* **25,** 189–197 (2006).

124. Charras, G. & Paluch, E. Blebs lead the way: how to migrate without lamellipodia. *Nat. Rev. Mol. Cell Biol.* **9,** 730–736 (2008).

125. Meyer, A. S. *et al.* 2D protrusion but not motility predicts growth factor-induced cancer cell migration in 3D collagen. *J. Cell Biol.* **197,** 721–729 (2012).

126. Klemke, R. L. Trespassing cancer cells: 'fingerprinting' invasive protrusions reveals metastatic culprits. *Curr. Opin. Cell Biol.* **24,** 662–669 (2012).

127. Cukierman, E., Pankov, R., Stevens, D. R. & Yamada, K. M. Taking cell-matrix adhesions to the third dimension. *Science* **294,** 1708–1712 (2001).

128. Cukierman, E., Pankov, R. & Yamada, K. M. Cell interactions with three-dimensional matrices. *Curr. Opin. Cell Biol.* **14,** 633–639 (2002).

129. Yamada, K. M., Pankov, R. & Cukierman, E. Dimensions and dynamics in integrin function. *Brazilian J. Med. Biol. Res.* **36,** 959–966 (2003).

130. Webb, K. *et al.* Comparison of human fibroblast ECM-related gene expression on elastic three-dimensional substrates relative to two-dimensional films of the same material. *Biomaterials* **24,** 4681–4690 (2003).

131. Nelson, C. M. & Bissell, M. J. Of extracellular matrix, scaffolds, and signaling: tissue architecture regulates development, homeostasis, and cancer. *Annu. Rev. Cell Dev. Biol.* **22,** 287–309 (2006).

132. Pedersen, J. A. & Swartz, M. A. Mechanobiology in the third dimension. *Ann. Biomed. Eng.* **33,** 1469–1490 (2005).

133. Lee, J., Cuddihy, M. J. & Kotov, N. A. Three-dimensional cell culture matrices: State of the art. *Tissue Eng. Part B-Reviews* **14,** 61–86 (2008).

134. Zaman, M. H., Matsudaira, P. & Lauffenburger, D. A. Understanding effects of matrix protease and matrix organization on directional persistence and translational speed in three-dimensional cell migration. *Ann. Biomed. Eng.* **35,** 91–100 (2007).

135. Friedl, P. & Gilmour, D. Collective cell migration in morphogenesis, regeneration and cancer. *Nat. Rev. Mol. Cell Biol.* **10,** 445–457 (2009).

136. Friedl, P. & Wolf, K. Tumour-cell invasion and migration: diversity and escape mechanisms. *Nat. Rev. Cancer* **3,** 362–74 (2003).

137. Yamada, K. M. & Cukierman, E. Modeling Tissue Morphogenesis and Cancer in 3D. *Cell* **130,** 601–610 (2007).

138. Wolf, K. *et al.* Multi-step pericellular proteolysis controls the transition from individual to collective cancer cell invasion. *Nat. Cell Biol.* **9,** 893–904 (2007).

139. Boudreau, N., Sympson, C. J., Werb, Z. & Bissell, M. J. Suppression of ICE and apoptosis in mammary epithelial cells by extracellular matrix. *Science* **267,** 891–3 (1995).

140. Weaver, V. M. *et al.* Reversion of the malignant penotype of human breast cells in three-dimensional cutlure and in vivo by integrin blocking antibodies. *J.Cell Biol.* **137,** 231–245 (1997).

141. Wang, F. *et al.* Reciprocal interactions between beta1-integrin and epidermal growth factor receptor in three-dimensional basement membrane breast cultures: a different perspective in epithelial biology. *Proc. Natl. Acad. Sci. U. S. A.* **95,** 14821–14826 (1998).

142. Wang, F. *et al.* Phenotypic reversion or death of cancer cells by altering signaling pathways in three-dimensional contexts. *J. Natl. Cancer Inst.* **94,** 1494–503 (2002).

143. Lee, G. Y., Kenny, P. A., Lee, E. H. & Bissell, M. J. Three-dimensional culture models of normal and malignant breast epithelial cells. *Nat Methods* **4,** 359–365 (2007).

144. Han, J. *et al.* Molecular predictors of 3D morphogenesis by breast cancer cell lines in 3D culture. *PLoS Comput. Biol.* **6,** 1–12 (2010).

145. van 't Veer, L. J. *et al.* Gene expression profiling predicts clinical outcome of breast cancer. *Nature* **415,** 530–536 (2002).

146. Calvo, V. & Kenny, P. a. Visualizing movement in the tumor microenvironment landscape. *Breast Cancer Res.* **15,** 301 (2013).

147. Bredfeldt, J. *et al.* Automated quantification of aligned collagen for human breast carcinoma prognosis. *J. Pathol. Inform.* **5,** 28 (2014).

148. Provenzano, P. P., Inman, D. R., Eliceiri, K. W., Trier, S. M. & Keely, P. J. Contact guidance mediated three-dimensional cell migration is regulated by Rho/ROCK-dependent matrix reorganization. *Biophys J* **95,** 5374–5384 (2008).

149. Gehler, S., Ponik, S. M., Riching, K. M. & Keely, P. J. Bi-directional signaling: extracellular matrix and integrin regulation of breast tumor progression. *Crit. Rev. Eukaryot. Gene Expr.* **23,** 139–57 (2013).

150. Riching, K. M. *et al.* 3D collagen alignment limits protrusions to enhance breast cancer cell persistence. *Biophys. J.* **107,** 2546–2558 (2015).

151. Shi, Q. *et al.* Rapid disorganization of mechanically interacting systems of mammary acini. *Proc. Natl. Acad. Sci. U. S. A.* **111,** 658–63 (2013).

152. Ivascu, A. & Kubbies, M. Rapid generation of single-tumor spheroids for high-throughput cell function and toxicity analysis. *J Biomol Screen* **11,** 922–932 (2006).

153. Kraning-Rush, C. M., Carey, S. P., Lampi, M. C. & Reinhart-King, C. A. Microfabricated collagen tracks facilitate single cell metastatic invasion in 3D. *Integr. Biol.* **5,** 606 (2013).

154. Leitinger, B. Transmembrane collagen receptors. *Annu Rev Cell Dev Biol* **27,** 265–290

(2011).

155. Humphries, J. D., Byron, A. & Humphries, M. J. Integrin ligands at a glance. *J. Cell Sci.* **119,** 3901–3903 (2006).

156. Hegedüs, B., Marga, F., Jakab, K., Sharpe-Timms, K. L. & Forgacs, G. The Interplay of Cell-Cell and Cell-Matrix Interactions in the Invasive Properties of Brain Tumors. *Biophys. J.* **91,** 2708–2716 (2006).

157. Rubenstein, B. M. & Kaufman, L. J. The role of extracellular matrix in glioma invasion: a cellular Potts model approach. *Biophys. J.* **95,** 5661–80 (2008).

158. Hazan, R. B., Phillips, G. R., Qiao, R. F., Norton, L. & Aaronson, S. A. Exogenous expression of N-cadherin in breast cancer cells induces cell migration, invasion, and metastasis. *J. Cell Biol.* **148,** 779–790 (2000).

159. Sorlie, T. *et al.* Gene expression patterns of breast carcinomas distinguish tumor subclasses with clinical implications. *Proc. Natl. Acad. Sci. U. S. A.* **98,** 10869–74 (2001).

160. Herschkowitz, J. I. *et al.* Identification of conserved gene expression features between murine mammary carcinoma models and human breast tumors. *Genome Biol.* **8,** 76 (2007).

161. Paik, S. *et al.* A multigene assay to predict recurrence of tamoxifen-treated, node-negative breast cancer. *N. Engl. J. Med.* **351,** 2817–26 (2004).

162. Chang, H. Y. *et al.* Gene expression signature of fibroblast serum response predicts human cancer progression: Similarities between tumors and wounds. *PLoS Biol.* **2,** 206–214 (2004).

163. Chi, J. T. *et al.* Gene expression programs in response to hypoxia: cell type specificity and prognostic significance in human cancers. *PLoS Med.* **3,** e47 (2006).

164. Charafe-Jauffret, E. *et al.* Breast cancer cell lines contain functional cancer stem sells with metastatic capacity and a distinct molecular signature. *Cancer Res.* **69,** 1302–1313 (2009).

165. Liu, Y. *et al.* Lack of correlation of stem cell markers in breast cancer stem cells. *Br. J. Cancer* **110,** 2063–71 (2014).

166. Garcia-Bellido, A., Ripoll, P. & Morata, G. Developmental Compartmentalisation of the Wing Disk of Drosophila. *Nat. New Biol.* **245,** 251–253 (1973).

167. Rev, A., Dev, C., Downloaded, B., Irvine, K. D. & Rauskolb, C. B OUNDARIES IN D EVELOPMENT : Formation and Function. *Most* 189–214 (2001).

168. Dahmann, C., Oates, A. C. & Brand, M. Boundary formation and maintenance in tissue development. *Nat. Rev. Genet.* **12,** 43–55 (2011).

169. Foty, R. A. & Steinberg, M. S. Cadherin-mediated cell-cell adhesion and tissue segregation in relation to malignancy. *Int. J. Dev. Biol.* **48,** 397–409 (2004).

170. Pawlizak, S. *et al.* Testing the differential adhesion hypothesis across the epithelial-mesenchymal transition. *New J. Phys.* **17,** 83049 (2015).

171. Carey, S. P., Starchenko, A., McGregor, A. L. & Reinhart-King, C. A. Leading malignant cells initiate collective epithelial cell invasion in a three-dimensional heterotypic tumor spheroid model. *Clin. Exp. Metastasis* **30,** 615–630 (2013).

172. Michor, F. & Polyak, K. The origins and implications of intratumor heterogeneity. *Cancer Prev. Res.* **3,** 1361–1364 (2010).

173. Heppner, G. H. Tumor heterogeneity. *Cancer Res.* **44,** 2259–2265 (1984).

174. Marusyk, A. & Polyak, K. Tumor heterogeneity: causes and consequences. *Biochim Biophys Acta* **1805,** 1–28 (2011).

175. Zellmer, V. R. *et al.* Evolving concepts of tumor heterogeneity. *Cell Biosci.* **4,** 69 (2014).

176. Steinberg, M. S. Reconstruction of Tissues by Dissociated Cells. *Science (80-.).* **141,** 401–408 (1963).

177. Foty, R. a, Pfleger, C. M., Forgacs, G. & Steinberg, M. S. Surface tensions of embryonic tissues predict their mutual envelopment behavior. *Development* **122,** 1611–20 (1996).

178. Steinberg, M. S. Differential adhesion in morphogenesis: a modern view. *Curr. Opin. Genet. Dev.* **17,** 281–286 (2007).

179. Graner, F. & Glazier, J. A. Simulation of biological cell sorting using a two-dimensional extended Potts model. *Phys. Rev. Lett.* **69,** 2013–2016 (1992).

180. Merks, R. M. H., Brodsky, S. V., Goligorksy, M. S., Newman, S. A. & Glazier, J. A. Cell elongation is key to in silico replication of in vitro vasculogenesis and subsequent remodeling. *Dev. Biol.* **289,** 44–54 (2006).

181. Hirashima, T., Iwasa, Y. & Morishita, Y. Dynamic modeling of branching morphogenesis of ureteric bud in early kidney development. *J. Theor. Biol.* **259,** 58–66 (2009).

182. Hester, S. D., Belmonte, J. M., Gens, J. S., Clendenon, S. G. & Glazier, J. A. A multi-cell, multi-scale model of vertebrate segmentation and somite formation. *PLoS Comput. Biol.* **7,** (2011).

183. Scianna, M. & Preziosi, L. A cellular Potts model for the MMP-dependent and -independent cancer cell migration in matrix microtracks of different dimensions. *Comput. Mech.* **53,** 485–497 (2014).

184. Glazier, J. & Graner, F. Simulation of the differential adhesion driven rearrangement of biological cells. *Phys. Rev. E. Stat. Phys. Plasmas. Fluids. Relat. Interdiscip. Topics* **47,** 2128–2154 (1993).

185. Cesi, G., Walbrecq, G., Margue, C. & Kreis, S. Transferring intercellular signals and traits between cancer cells: extracellular vesicles as 'homing pigeons'. *Cell Commun. Signal.* **14,** 13 (2016).

186. Kanada, M., Bachmann, M. H. & Contag, C. H. Signaling by Extracellular Vesicles Advances Cancer Hallmarks. *Trends in Cancer* **2,** 84–94 (2016).

187. Ziperstein, M. J., Guzman, A. & Kaufman, L. J. Breast cancer cell line aggregate morphology does not predict invasive capacity. *PLoS One* **10,** 1–17 (2015).

188. Gonzalez, E. *et al.* Human mammospheres secrete hormone-regulated active extracellular vesicles. *PLoS One* **9,** (2014).

189. Vieira, A. F. *et al.* P-cadherin signals through the laminin receptor α6β4 integrin to induce stem cell and invasive properties in basal-like breast cancer cells. *Oncotarget* **5,** 679–692 (2014).

190. Lehmann, B. D. B. *et al.* Identification of human triple-negative breast cancer subtypes and preclinical models for selection of targeted therapies. *J. Clin. Invest.* **121,** 2750–2767 (2011).

Appendix 1 Abbreviations

Basement membrane extract ..... BME

Confocal reflectance microscopy ..... CRM

Dimethyl sulfoxide ..... DMSO

Epithelial to mesenchymal transition ..... EMT

Extracellular matrix ..... ECM

Fetal bovine serum ..... FBS

Fluorescence-activated cell sorting ..... FACS

Matrix metalloproteinase ..... MMP

Three dimensional 3D

Two dimensional 2D

Appendix 2 ImageJ scripts

Batch z-projections

To create maximum intensity z-projections of multiple multi-tiff files in a common folder, the following script can be used in ImageJ. To use, save the following as a .ijm file and run Plugins > Install. The file name should now be accessible under Plugins. When the program runs, it will ask for a source directory, file type (“TIFF”), and a destination directory. The new projection images will be saved with the same name as the original files. The slices to be projected can be adjusted in line 10, but will be consistent for all files in the folder.

```
1  dir1 = getDirectory("Choose Source Directory ");
2  format = getFormat();
3  dir2 = getDirectory("Choose Destination Directory ");
4  list = getFileList(dir1);
5  setBatchMode(true);
6  for (i=0; i<list.length; i++) {
7   showProgress(i+1, list.length);
8   open(dir1+list[i]);
9
10 run("Z Project...", "start=1 stop=21 projection=[Max Intensity]");
11
12  if (format=="8-bit TIFF" || format=="GIF")
```

```
13      convertTo8Bit();
14      saveAs(format, dir2+list[i]);
15      close();
16     }
17     function getFormat() {
18      formats = newArray("TIFF", "8-bit TIFF", "JPEG", "GIF", "PNG",
19      "PGM", "BMP", "FITS", "Text Image", "ZIP", "Raw");
20      Dialog.create("Batch Convert");
21      Dialog.addChoice("Convert to: ", formats, "TIFF");
22      Dialog.show();
23      return Dialog.getChoice();
24     }
25     function convertTo8Bit() {
26      if (bitDepth==24)
27      run("8-bit Color", "number=256");
28      else
29      run("8-bit");
30     }
```

Batch crop images

Similarly, to crop multiple tiff files in a common folder, the following script can be used in ImageJ. To use, save the following as a .ijm file and run Plugins > Install. The file name should now be accessible under Plugins. When the program runs, it will ask for a source directory, file type ("TIFF"), and a destination directory. The new cropped images will be saved with the same name as the original files. The area to be cropped can be adjusted in line 10 and is written in the order (initial pixel count from left, initial pixel count from bottom, final pixel count from left, final pixel count from bottom), but will be consistent for all files in the folder. Lines 12 and 13 can be deleted if automatic brightness and contrast adjustment is not desired. Multitiff files must be removed from the folder before running the program, as they will cause the program to crash and any remaining images in the folder will not be cropped.

```
1  dir1 = getDirectory("Choose Source Directory ");
2  format = getFormat();
3  dir2 = getDirectory("Choose Destination Directory ");
4  list = getFileList(dir1);
5  setBatchMode(true);
6  for (i=0; i<list.length; i++) {
7   showProgress(i+1, list.length);
8   open(dir1+list[i]);
9
10 makeRectangle(0, 0, getWidth/2, getHeight);
11 run("Crop");
```

```
12  run("Brightness/Contrast...");
13  run("Enhance Contrast", "saturated=0.01");
14
15   if (format=="8-bit TIFF" || format=="GIF")
16   convertTo8Bit();
17   saveAs(format, dir2+list[i]);
18   close();
19  }
20  function getFormat() {
21   formats = newArray("TIFF", "8-bit TIFF", "JPEG", "GIF", "PNG",
22   "PGM", "BMP", "FITS", "Text Image", "ZIP", "Raw");
23   Dialog.create("Batch Convert");
24   Dialog.addChoice("Convert to: ", formats, "TIFF");
25   Dialog.show();
26   return Dialog.getChoice();
27  }
28  function convertTo8Bit() {
29   if (bitDepth==24)
30   run("8-bit Color", "number=256");
31   else
32   run("8-bit");
33  }
```

Overlay images

To create composite images in which grayscale images are overlaid in different colors, the following script can be used in ImageJ. To use, save the following as a .ijm file and run Plugins > Install. The file name should now be accessible under Plugins. When the program runs, it will ask for a Source Directory and the number of columns in the final image. Labels can be omitted by removing the text "label" from line 10. In line 17, colors are defined as C1 red, C2 green, C3 blue, C4 gray, C5 cyan, C6 magenta, and C7 yellow and can be adjusted accordingly. Since the code runs on all images in a folder – separate samples showing as subsequent rows in the final image – the image can be cropped and samples saved individually by running Image>Stacks>Tools>Montage to Stack>images per row = 1, images per column = number of samples. For original images A-H shown in Figure 21 and indicating 2 columns (for 2 time points), the final image will look like Figure 22.

```
1  source_dir = getDirectory("Source Directory");
2  stack1=source_dir+File.separator;
3  list=getFileList(source_dir);
4  columnsize = getNumber("Number of Columns: ", columnsize);
5  colsize= columnsize*2
6  rowsize=list.length/columnsize/2
7  run("Image Sequence...", "open=&stack1 scale=100 sort");
8
9  run("Make Montage...", "columns=colsize rows=rowsize scale=1 first=1 increment=1 border=0
10 font=12 label");
```

```
selectWindow("");
close();
run("Montage to Stack...", "images_per_row=2 images_per_column=1 border=0");
selectWindow("Montage");
close();
run("Stack to Images");
run("Merge Channels...", "c1=Stack-0001 c2=Stack-0002");
```

Figure 21 Sample images A-H. A-D = sample 1, E-H = sample 2. A-B and E-F are imaged in the red channel. C-D and G-H are imaged in the green channel. A, C, E, and G are imaged at time point 1. B, D, F, and H are imaged at time point 2.

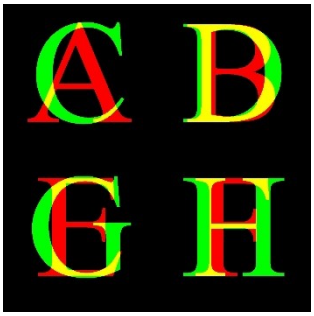

Figure 22 Final composite of samples images A-H. Pixels appear yellow where bright spots in red and green channels intersect. Image can be further cropped to isolate sample 1 (top row) from sample 2 (bottom row) in ImageJ by Image> Stacks> Tools> Montage to Stack> images per row: 1, images per column: 2 and Image> Stacks> Stack to Images.

Appendix 3 Matlab code

Segregation analysis of co-culture spheroid images

This matlab code was written to create histograms based on the number of pixels in red and green channels relative to the distance from the center of mass. Images from red and green channels are converted to binary before inputting them into the program. In the program, the red and green images are treated equally in a single matrix to find the center of mass. Then, the distance of each pixel from the center of mass is calculated separately for each color. Output shows a histogram of the distribution of pixel distances from the center of mass for red and green channels.

```
clear all;
close all;
clc;

doAgain = 1;

while doAgain == 1
    %pick image to input
    prompt = 'What is the image name (exclude .tif)? : ';
    name = input(prompt, 's');
    file = '.tif';
    imageName = strcat(name,file);
```

```
13
14      %input file
15      im = imread(imageName);
16      R = im(:,:,1);
17      G = im(:,:,2);
18
19      %find the center of mass
20      Im_gray = rgb2gray(im);
21
22      [y,x] = find(Im_gray);
23      CenterOfMass = [mean(x),mean(y)];
24
25      %show center of mass on image
26      imshow(Im_gray);
27      hold on
28      plot(CenterOfMass(:,1),CenterOfMass(:,2), 'r*')
29      hold off
30
31      saveName = strcat(name,'_Center_of_Mass');
32
33      print(saveName,'-dtiffn');
34
```

```
35      %make a matrix of radial distribution for color red
36      [x,y] = find(R);
37
38      x1 = x - CenterOfMass(1,1);
39      y1 = y - CenterOfMass(1,2);
40
41      x1 = abs(x1);
42      y1 = abs(y1);
43
44      x1 = sqrt(x1);
45      y1 = sqrt(y1);
46
47      [m,n] = size(x1);
48
49      red_distances = [];
50
51      for c = 1:m
52          red_distances = [red_distances; x1(c)*y1(c)];
53      end
54
55      %make a matrix of radial distribution for color green
56      [x,y] = find(G);
```

```
57
58      x1 = x - CenterOfMass(1,1);
59      y1 = y - CenterOfMass(1,2);
60
61      x1 = abs(x1);
62      y1 = abs(y1);
63
64      x1 = sqrt(x1);
65      y1 = sqrt(y1);
66
67      [m,n] = size(x1);
68
69      green_distances = [];
70
71      for c = 1:m
72          green_distances = [green_distances; x1(c)*y1(c)];
73      end
74
75      %output the matrix in excel
76
77      saveName = strcat(name,'_CMTPX_distribution.xlsx');
78      xlswrite(saveName, green_distances);
```

```
79
80      saveName = strcat(name,'_DID_distribution.xlsx');
81      xlswrite(saveName, red_distances)
82
83      %plot overlay histogram
84
85      figure
86      h_CMTPX = histogram(green_distances,'FaceColor','g');
87      hold on
88      h_DID = histogram(red_distances,'FaceColor','r');
89
90      h_CMTPX.Normalization = 'probability'; %normalize the bars to set as percentage
91      h_DID.Normalization = 'probability';
92
93      h_CMTPX.BinWidth = 2.5;
94      h_DID.BinWidth = 2.5;
95
96
97      legend('CMTPX','DID');
98
99      title('Distribution of Two Cell Lines');
100     xlabel('Distance from Spheroid Center');
```

```
101         ylabel('Distribution');
102
103         saveName = strcat(name,'_histogram');
104         print(saveName,'-dtiffn');
105
106         %ask whether to analyze image again
107         askAgain=0;
108
109         while askAgain == 0
110             prompt = 'Analyze another image(Y/N)? : ';
111             name = input(prompt, 's');
112             if name=='N'
113                 doAgain=0;
114                 askAgain=1;
115             elseif name=='Y'
116                 askAgain=1;
117             end
118         end
119     end
```